MAGNETORHEOLOGICAL CEMENTITIOUS INKS FOR 4D PRINTING OF ORIGAMI INSPIRED AUXETIC CONCRETE ELEMENTS

by

Aparna Shashikant Deshmukh

A Dissertation Submitted in

Partial Fulfillment of the

Requirements for the Degree of

Doctor of Philosophy

in Engineering

at

The University of Wisconsin-Milwaukee

December 2021

ABSTRACT

MAGNETORHEOLOGICAL CEMENTITIOUS INKS FOR 4D PRINTING OF ORIGAMI INSPIRED AUXETIC CONCRETE ELEMENTS

by

Aparna Shashikant Deshmukh

The University of Wisconsin-Milwaukee, 2021
Under the Supervision of Professor Konstantin Sobolev

Existing concrete technology relies on the use of considerable volumes of raw materials, large energy consumption and so associated with severe corresponding environmental impacts. This impact is the driving force for the development of sustainable concrete including a wide range of concrete with supplementary cementitious materials and advanced manufacturing. Recent developments in the field are further inspired by the digital concrete based on 3D printing (3DP) technology which require tailor-made concrete mixtures. The main challenge for 3D printing of concrete is to develop printable ink material, thus this research focuses on characterisation of cementitious materials based on smart materials-materials that respond to specific stimuli and can be tuned as needed. The 3DP using smart material or resulting in a smart materials response is termed as 4D printing (4DP). The smart materials used in this research are tuned for the magnetorheological and auxetic responses, where the former controls the green strength while the latter controls the mechanical response of the hardened composite based on of the proposed cementitious ink. The design methodology for the cementitious ink and auxetic concrete is proposed here, along with supporting experimental data based on experiment planning approach as no specific standards or guidelines are

available yet for the design of new composites.

Systematically designed cement based mixtures incorporating various proportions of portland cement (PC), high-ferrous Class-F fly ash (FA), nano-silica (NS), and nano-alumina (NA) were characterized for rheological response with and without the application of a magnetic field in order to better understand the effects of potential doping of cement with magnetic material for application in '4D-printing' of cementitious 'smart materials' (SM). Control groups doped with industrial-grade magnetite powder (commonly used as pigment) were likewise mixed and characterized to provide contrast to low cost ferromagnetic components based on beneficiated coal-combustion byproduct fly ash. Mixtures supplemented with ferromagnetic particles had demonstrated the amplified yield stress when exposed to the magnetic field, leading to non-Newtonian rheological response exhibiting 'sticky particles' paradigms as discussed herein. Further, control portland cement systems were doped with cobalt powder at varying dosage to study the effect of strong ferromagnetic dopant on yield stress and stiffening stress. In order to develop a sustainable printable ink, ferromagnetic particles were extracted from fly ash using fly ash beneficiation technique, and were characterized for rheological and magnetorheological response. The heat of hydration, X-ray diffraction for individual components and products of the hydration, and compressive strength parameters were used to characterize the proposed cementitious inks. These results suggest that the idea of utilizing an applied magnetic field to modify the flow and slump of cementitious materials extruded through 3D-printing apparatus is worthy of further pursuit and development. In addition, the ferromagnetic particles used in this smart mix composition did not influence cement hydration or compressive strength, however, the applied magnetic field slightly accelerated the hydration process of portland cement.

Another smart material approach used in this research was focusing on the development

of auxetic concrete elements that exhibits a negative Poison's ratio due to it's geometrical configuration. Based on the principle of origami and kirigami, the geometry of the auxetic concrete was designed. The nano-engineered fiber-reinforced cement composites were used to create the auxetic samples and were tested to confirm their auxetic behavior. The result of this research provided a substantial confidence in the potential of additive manufacturing and the use of auxetic concrete contributing to a broader practical application of 4DP. This research enabled to establish the theoretical framework and fundamental understanding of magnetorheological cementitious ink materials with ultimate active control of rheological behavior, the formation of patterned microstructures as required for an auxetic response, and improved fracture toughness capable of scaling up to 4D printing of smart origami and kirigami (OAK)-oriented structures. The advancement of engineered cementitious inks based on ferromagnetic nano-particles, nano-fibers, and micron-sized powders combined with magnetite-rich fly ash particles can result in a smart rheological response of the ink, enabling immediate on-demand stiffening, the formation of "patterned" microstructures, and accelerated strength development under short-term electro-magnetic (EM) fields as required for the long-term auxetic response of structural elements. The promising outcome of this research along with future study will led to the development of EM-induced on-demand stiffening and strength development of digitally-deposited cementitious ink materials shall represent a foundational paradigm shift in the approach and methodology of additive manufacturing which will be applicable to a range of auxetic biomaterials, ceramics, and concrete enabling the materialization of future cyber infrastructure with capabilities to deploy permanent structures and habitations here on earth, underwater, up to the Moon, Mars, and beyond.

©Copyright by Aparna Shashikant Deshmukh, 2021
All Rights Reserved

Dedicated to

My late grandparents ***(Aai- Anna)***, this achievement is your blessings,

My parents ***(Mummy- Papa)*** for their unconditional love and,

My beloved husband ***(Amit)***.

TABLE OF CONTENTS

ABSTRACT ii

LIST OF FIGURES **x**

LIST OF TABLES **xvii**

ACKNOWLEDGEMENT xix

1 Introduction **1**

1.1 Objectives 4

1.2 Thesis Outline 5

2 Literature Review **6**

2.1 Additive manufacturing technologies 6

2.2 Challenges in current additive manufacturing technologies 8

2.3 Why 4D printing of concrete? 9

2.4 Requirements of concrete for 3D printing 11

2.5 Magnetorheological response and active control of concrete 12

2.6 Fly ash beneficiation for magnetorheological applications 14

2.7 Lunar Regolith: potential for 3D printing 15

2.8 Concrete auxetic structures 16

3 Materials **18**

3.1 Overview of materials used in research 18

3.2 Material characterization 22

3.2.1 Particle size distribution 22

3.2.2 Particle shape and morphology 23

4 Test methods and experimental results 27

4.1 Fly ash beneficiation 27

4.1.1 Demand for fly ash beneficiation 28

4.1.2 Type and chemical composition of fly ash 30

4.1.3 Milling procedure and magnetic separation 30

4.1.4 Material balance for milled and magnetically separated fly ash 33

4.1.5 Characterization of milled and beneficiated fly ash 34

4.2 Lunar Regolith 40

4.2.1 Particle size distribution 41

4.2.2 Mineral composition 42

4.2.3 Effect of milling 42

4.3 Rheological properties of cementitious inks 44

4.3.1 Testing equipment and geometry 47

4.3.2 Design and evaluation of electromagnet 48

4.3.3 Sample preparation and testing protocols 48

4.3.4 Experimental matrix for rheological and magnetorheological measurements 52

4.3.5 Rheological and magnetorheological response of MRCI 55

4.4 Hydration of cementitious inks 72

4.4.1 Heat of hydration 74

4.5 Compressive strength of developed cementitious inks 82

4.5.1 Portland cement and milled fly ash systems 84

4.5.2 Portland cement and Lunar regolith systems 85
4.5.3 Fiber-reinforced composites 87
4.6 Bending response of fiber-reinforced composites 89
4.7 Tensile response of fiber-reinforced composites 92
4.7.1 Splitting/ wedge test 92
4.7.2 Direct tension response 93
4.7.3 Characterization of notched samples 93

5 Design philosophy and practical applications of auxetic concrete 97
5.1 Auxetic metamaterials and structures 99
5.1.1 Classification of auxetic metamaterials 100
5.1.2 Mechanical response of auxetic composites based on developed inks . 105

6 Conclusions and future work 108

Bibliography 112

Curriculum Vitae 125

LIST OF FIGURES

1.1 Thesis outline 5

2.1 The 3DPC projects implemented in last two decades [1] 7

2.2 The schematics explaining 3D and 4D printing process 10

2.3 4D printing market size in USD Million since 2019 10

2.4 The deformation of i) conventional material and ii) auxetic material subjected to loading 16

3.1 The TEM of nano-alumina fibers [2] 21

3.2 SEM of portland cement:(a) x1000 and (b) x2500 24

3.3 SEM of representative Class F fly ash (Oak Creek):(a) x1000 and (b) x2500 25

3.4 SEM of Lunar regolith at X1000: (a) fine LR sample and (b) fine LR sample F6 25

3.5 SEM of magnetite powder: (a) x2500 and (b) x5000 25

3.6 Images of cobalt powder under confocal microscope: (a) 2D image and (b) 3D image 26

3.7 SEM of Cobalt powder 26

4.1 (a)SWECO vibro energy grinding mill used for wet-milling of Fly ash (b) milling balls/ used as grinding media 32

4.2 Magnetic separation setup used for separation of milled fly ash 33

4.3 Material balance after milling each Prairie State, LG 14 and Oak Creek class F fly ash for 1hr, 2hrs and 3hrs, respectively. 34

4.4 Particle size of Oak Creek fly ash milled for 1hr, 2hrs and 3hrs 35
4.5 Particle size of LG14 fly ash milled for 1hr, 2hrs and 3hrs 36
4.6 Particle size of Prairie State fly ash milled for 1hr, 2hrs and 3hrs 37
4.7 Comparative mineral composition (XRD) of magnetic and non magnetic Class F Oak Creek fly ash milled for one hour, two hours and three hours . . 38
4.8 Comparative mineral composition (XRD) of magnetic and non magnetic Class F LG14 fly ash milled for one hour, two hours and three hours 39
4.9 Comparative mineral composition (XRD) of magnetic and non magnetic Class F Prairie state fly ash milled for one hour, two hours and three hours . 40
4.10 Sieve analysis curve for LR samples 41
4.11 The X-ray diffraction Characteristics of fine LR samples 43
4.12 The X-ray diffraction for coarse LR samples 44
4.13 Response of magnetorheological fluid:(a) without magnetic field, fly ash and magnetite particles are randomly distributed and (b) ferrous particles aligning along the flux path under magnetic field, after [3] 45
4.14 The schematics for electromagnet 48
4.15 The schematics of the experimental setup with electromagnet including the side plates and magnetic field marked by the arrows. 49
4.16 Experimental setup for magnetorheological test: Pictures of (a) vane rotor and steel cylinder inside the solenoid; (b) the electromagnet with side steel plates and power supply 50
4.17 The test protocol for magnetorheological investigation 51
4.18 The models governing the rheological response of MRCI: (a) ramp up; (b) ramp down 56

4.19 The effect of nano-silica and nano-alumina fibers on rheological response of (a) superplasticized portland cement systems – R_1 series, and (b) the effect of magnetite powder – R_1M series 61

4.20 The effect of nano-silica and nano-alumina fibers on rheological response of (a) superplasticized portland cement-fly ash pastes – R_2 series and (b) the effect of addition of magnetite powder – R_2M series 62

4.21 The effect of magnetic field on rheological response of (a) superplasticized portland cement pastes doped with nano-particles R_1' series and (b) the effect of addition of magnetite powder – R_1M' series 64

4.22 The effect of magnetic field on rheological response of (a) superplasticized portland cement -fly ash pastes doped with nano-particles R_2' series and (b) the effect of addition of magnetite powder – R_2M' series 65

4.23 Response and structural build-up of magnetic material within the MRCI: (a) without nano-particles, magnetic particles are closely locked at poles and build a stronger chain resulting in stiffer structures and (b) nano-particles create a barrier between the magnetic poles on ferrous material thus enabling sliding 65

4.24 The effect of magnetic field on the yield stress (under third ramp down test) on Stage 1 compositions 66

4.25 The build-up of yield and stiffening stress on Stage 1 compositions due to application of magnetic field (under third ramp down test) 66

4.26 The effect of cobalt on the rheological response of compositions at the first ramp series (a) no magnetic field and (b) under the magnetic field 68

4.27 The effect of milled fly ash on rheological response of the first ramp series at superplasticized cementitious ink (a) no magnetic field (b) under magnetic field 69
4.28 The effect of milled fly ash on the rheological response of cementitious inks at the first ramp series showing (a) no magnetic field (b) under magnetic field 70
4.29 The effect of magnetic field on the yield stress (under third ramp down test) for Stage 2 and 3 compositions 71
4.30 The build-up of yield and stiffening stress on Stage 2 and 3 compositions due to the application of magnetic field (under third ramp down test) 71
4.31 The representative heat of hydration curve indicating different phases of heat of hydration of cementitious inks 72
4.32 The effect of superplasticized portland cement pastes doped with nano-particles R_1 and with magnetite R_1M systems (a) no magnetic field (b) after application of magnetic field 75
4.33 The effect of superplasticized portland cement pastes doped with nano-particles R_2 and with magnetite R_2M systems on HOH of the Stage 1 compositions . 77
4.34 The effect of superplasticized portland cement pastes doped with nano-particles R_2 and with magnetite R_2M systems on HOH of the Stage 1 compositions after application of magnetic field 77
4.35 The effect of superplasticized portland cement pastes doped with cobalt powder on HOH of Stage 2 compositions 78
4.36 The effect of superplasticized portland cement pastes doped with cobalt powder on HOH of Stage 2 compositions after application of magnetic field . . . 79
4.37 The effect of magnetic field on the total heat evolution for Stage 1, Stage 2, and Stage 3 compositions 80

4.38 The effect of milling and beneficiation on the heat flow of cement systems with Oak Creek Class F fly ash (per content of cementitious material) (a) heat flow evolution (b) cumulative heat flow 80
4.39 The effect of milling and beneficiation on the heat flow of cement systems with Prairie State Class F fly ash (per content of cementitious material) (a) heat flow evolution (b) cumulative heat flow 81
4.40 The effect of milling and beneficiation on the heat flow of cement systems with LG14 Class F fly ash (per content of cementitious material) (a) heat flow evolution (b) cumulative heat flow 82
4.41 The effect of fine LR on the heat flow of cement systems (a) fine LR milled (b) fine LR (as received) 83
4.42 The effect of fine LR on the heat flow of cement systems (a) fine LR milled (b) fine LR (as received) 83
4.43 Compressive strength for milled and beneficiated Oak Creek fly ash compositions. 85
4.44 Compressive strength for compositions with cement replacement by Fine LR. 87
4.45 Compressive strength for compositions with cement replacement by milled Fine LR 88
4.46 Compressive strength for compositions with aggregates replacement by coarse LR. 88
4.47 The fiber reinforced composite cubes: (a) standard cube, (b) cube with one notch, (c) cube with two notches 89
4.48 The load-displacement curve for fiber-reinforced composite for cube sample . 90

4.49 The cube with one notch is tested for compression: (a) experimental set up, (b) The load-displacement curve for cube with one notch 90
4.50 Thee types of beam samples tested in this study 91
4.51 The four point bending test for reference beam loaded in the direction parallel to its greater depth 91
4.52 The four point bending test for v- notched beam loaded in the direction parallel to its greater depth 92
4.53 The four point bending test for reference beam loaded in the direction parallel to its smaller depth 93
4.54 The four point bending test for c-notched beam loaded in the direction parallel to its smaller depth 94
4.55 The cube with two notches is tested for compression: (a) experimental set up, (b) The load-displacement curve for cube with two notches 95
4.56 The load-displacement curve for reference beam subjected to tensile load . . 95
4.57 The load-displacement curve for v-notched beam subjected to tensile load . . 96

5.1 Classification of auxetic metamaterials 101
5.2 The examples of origami-inspired structures 102
5.3 The PSN materials a) alternative horizontal and vertical slits forming squares; b) random perforations forming hexagon [78] 103
5.4 Map of bulk modulus and shear modulus with regions of negative PR and negative stiffness [4] 104
5.5 The auxetic geometries tested in this research (a) initial geometrical design tested, (b) optimized geometrical configuration of auxetic concrete 106

5.6 The load- displacement curve for auxetic concrete (a) initial geometry, (b) optimized geometry 106

5.7 The apparent Poisson's ratio for auxetic concrete (a) initial geometry, (b) optimized geometry 107

LIST OF TABLES

2.1 Comparative cost estimates for construction of a wall with 40MPa concrete using conventional method and 3DPC [5] 7

3.1 Chemical composition and physical properties of portland cement Type I . . 19

3.2 Particle size for cementitious materials 23

4.1 The chemical composition and physical properties of Class F fly ash 30

4.2 Compositions used for fly ash milling 31

4.3 Reduction in particle size after milling of LR fine samples 45

4.4 The expanded test program for Stage 1: portland cement and fly ash systems doped with nano-particles and magnetite powder 53

4.5 The experimental matrix for Stage 2: portland cement systems doped with cobalt powder 54

4.6 The experimental matrix for Stage 3: portland cement systems with 10% 3hrs milled fly ash 55

4.7 Rheological constants and percentage built up for ramp down (RD) responses for stage 1 compositions 58

4.8 Rheological constants and percentage built up for ramp down (RD) responses for stage 2 compositions 59

4.9 Rheological constants and percentage built up for ramp down (RD) response of stage 3 compositions 60

4.10 The heat of hydration constants and percentage build up for heat flow and accelerated time for Stage 1 compositions 76
4.11 The heat of hydration constants and percentage build up for heat flow and accelerated time for Stage 2 compositions 78
4.12 The heat of hydration constants and accelerated time for milled fly ash compositions 81
4.13 The densities of the cementitious products used for ink design 84
4.14 The compositions for mortars based on milled fly ash systems. 85
4.15 The mix compositions for fine LR systems. 86
4.16 The mix compositions for LR sand systems. 87

ACKNOWLEDGEMENTS

First and foremost, I am extremely grateful to my advisor, Dr. Konstantin Sobolev for his invaluable advice, continuous support, and motivation during my PhD research. His immense knowledge and plentiful experience have encouraged me to work in materials part of civil engineering. His expertise helped me to formulate research questions, research plan and methodology. He always made me believe in myself, his words, "Aparna, you can do it", have always kept me going. Without his guidance I would not be able to accomplish this multidisciplinary research.

I would like to extend my sincere thanks to Dr. Zhao, Dr. Tabatabai, Dr. Ma, Dr. Kouklin, and Dr. Kozhukhova for agreeing to be part of my committee. I also thank Steve Kosmatka for providing his feedback and stepping forward and helping me whenever possible.

I express my sincere gratitude to all the undergraduate assistants who helped me with all the research projects that I have worked on at UWM. A special recognition to our two gems: Rosalba Huerta who was there to help me throughout this research with experimental setup, experiments and data analysis, Gabriel Stern who single handedly handle all the 3D models, finite element modelling, 3D printed molds and prototypes. Also, special thanks to Sara Huerta for all the last-minute help with data representation.

In addition, I would like to thank our Master students: Paul George for all his help with casting and testing, Milad Manjili for helping me with PSD and XRD testing and Anita for providing her expert insight on chemistry of materials. I express my gratitude to my colleagues, Roy Wittenberg, Marina Kozhukhova, Behrouz Farahi, Reed Heintzkill, Filip Zemajtis for helping me whenever needed, adjusting their schedule for my experiments, providing me honest and sincere feedback and co-operating in all possible ways. Thanks to

Filip for helping me with his expertise in materials and Reed for going through the technical writings and arranging awesome lab outings.

I am grateful to Dr. Hua Liu and Dr. Zhao for helping me setting up the strain gauges and data acquisition, and support with mechanical testing of samples. Additionally, I would like to thank Rahim Reshadi for helping me with all the testing set up in the Structural Lab

I would like to extend my sincere thanks to John Condon and Bob Breske from Machine Shop for their time sensitive help and ability to modify the designs as required. Additionally, I would thank Steven Hardcastle from AAF for providing timely help and advice in using AAF facility.

I am thankful to Civil Engineering Department and all the professors for supporting me financially through a teaching assistantship for almost half of my stay at UWM. I would like to extend my sincere gratitude towards UWM research foundation for financially supporting my research through UWM catalyst grant.

I am grateful to have friends like a family, making my stay in the United States like home- away from home. I thank Anisha, Darshit, Vaibhavi, Yash, Honey, Nishikant, Purva, Joanna, Vidit, Sharvari, Prateema, Shrish, Sarvesh, Yugg, Samruddhi, Kiran and the list goes on. A special thanks to Kaustubh Rane, for encouraging me to write my Thesis in Latex, reviewing it, and helping me to make it up to mark.

My parents are my greatest inspiration and epitome of simplicity and generosity. Without their support and faith in me, I wouldn't be in United States for my higher education. Mummy-Papa, it was not easy to stay so far away from you. I express my deepest gratitude to my parents for their efforts, sacrifices and believing in me throughout my educational journey. I would like to thank my brother, sister, cousin, and other family members for pushing me hard and making me laugh when I missed home. I would also thank my new

family, my in-laws (Aai-Baba) who always took keen interest to hear and understand my research.

Lastly, I thank the person who motivated me to graduate this semester. He is the one who have been listening to all my frustrations and tantrums, and yet with all patience cheering me up, reminding me how close I am to the finish line. So, this acknowledgement would not be complete without thanking my dear husband, Amit.

न हि ज्ञानेन सदृशं पवित्रमिह विद्यते ।

तत्स्वयं योगसंसिद्धः कालेनात्मनि विन्दति ।।4.38 ।

Bhagavad Geeta, Chapter 4, Verse 38

"In this world, there is nothing as purifying as divine knowledge. One who has attained purity of mind through prolonged practice of Yog, receives such knowledge within the heart, in due course of time."

Chapter 1

Introduction

The advent of the digital era has led to an explosion of new and never-before envisioned breakthroughs in manufacturing and fabrication technologies, not the least exciting of which is the field of additive manufacturing (AM) or 3D-printing. Application of digital manufacturing methods are being attempted in every conceivable realm, from the very small scale to the most massive, including concrete construction [6]. Possible benefits from the introduction of 3D-printing in concrete (3DPC) include saving on labor and raw materials, reduction of waste, reduced construction time, elimination of formwork, and improved quality control. Despite these substantial benefits, 3DPC faces a number of challenges and limitations such as lack of well-developed printable cementitious materials and mix designs, difficulty in incorporating reinforcing members into the printed matrix, lack of industrial design specifications, general inexperience in design and implementation specific to 3DP, and – most notably – issues controlling workability and immediate setting of concrete "inks". Nonetheless, 3DPC remains an exciting new frontier with tremendous potential for breakthroughs in the crossroads of industrial, civil, and materials engineering. In addressing the primary challenge of developing technology and materials with rheological properties tuned for 3DPC, a method of achieving 'active control' in material deposition is proposed. The active control can be achieved through the use of the Smart Materials (SM) – in this case, magnetically-manipulated cementitious material intended for the application in auxetic structures. Smart materials can generally be considered as material system in which

a predictable or programmed change can be achieved through the application of an outside stimulus. In a 2014 review, Bogue established five categories of SM: "shape changing, self-actuating, self-sensing, self-diagnostic, and self-healing"[7]. How can SM technology be incorporated into concrete construction? This reported research investigates a new category of SM, fitting the broader definition of a material that *changes* with stimuli, sub-classified as shape-changer and state-changer. The auxetic smart material is classified under shape changer as it exhibits negative "bulk" or "apparent" Poisson's ratio and responds to stimulus by producing a strain and shape memory effect. Here, magnetorheological response can be classified under a state changer as a response to applied magnetic field. The incorporated property such as magnetorheological response is tuned to address a fundamental problem with 3DPC: *maintaining a highly-pumpable and printable cementitious ink material that sets upon the command rapidly after deposition.*

The state-changing smart materials exhibit a change in rheological response under a magnetic field as a stimulus. The reported 'smart' cementitious inks for 3D printing undergo a change of state from liquid to congealed when a magnetic field is applied. The responsive constituents in these magneto-cementitious inks are nanosized ferromagnetic components, as well as highly ferrous fly ash powder when combined with cementitious phase, result in a flowable composition controlled by an applied magnetic field, yielding active control of the rheological behavior in fresh state, thus, termed Magnetorheological Cementitious Inks (MRCI).

The shape-changing smart materials which exhibit a unique counter-intuitive deformation response, are termed as auxetic materials [8]. Auxetic materials and assemblies reveal numerous outstanding properties which are not observed in conventional bulk materials and can be effectively incorporated into cement based composite structures, such as increase in

shear resistance [9], increased indentation resistance [10],[11], energy absorption [8], fracture resistance [12], variable permeability [13],[14],[15], ability to undergo synclastic curvature [16], increased toughness and sound dampening properties [17]. Auxetic structures have complicated geometries and repetitive void elements which cannot be produced using conventional concrete placing methods and so need to be 3D printed. Therefore, *3D printing, auxetic materials and MRCI are interdependent, compatible, and complementary technologies establishing 4D printing of concrete (4DPC).* Moreover, while researchers are striving hard to eliminate the challenges of 3DPC, these challenges can be overcome by introducing proposed 4DPC approach. Therefore, this research focuses on the development of smart concrete: characterization and design of MRCI and design approach for auxetic concrete.

The current thesis work is focused on detailed characterization and design of MRCI based on portland cement, supplementary cementitious materials with ferromagnetic inclusions, an array of nano components such as nano-silica particles and nano-alumina fibers, and microfiber reinforcements. The production of cement-based MRCI in this research, aimed at effective utilization of (potentially off-spec) fly ash, which is beneficiated using a selective separation of unburned carbon and extraction of high purity ash with higher quantities of magnetic inclusions as required for MRCI. The process of beneficiation includes milling of fly ash and then magnetically separating it in order to obtain magnetically rich fly ash component as required for MRCI. Different factors including the shape and size of reactive powders, chemical and mineral composition of the beneficiated fly ash; chemical composition of the cementitious material; and other factors strongly affect the magnetorheological properties of blended cement pastes.

With recent developments in 3D printing, NASA is aiming to built structures and habitats on extraterrestrial bodies like Moon and Mars. To realize these projects using local

materials easily available on-site such as Lunar regolith, is important. As a part of this research, simulated Lunar regolith was characterized and evaluated for its compatibility with portland cement chemistry using paste and mortar and also as required for its potential suitability for 3D printing.

1.1 Objectives

The aim of the current research is to:

1. Characterize various reactive powder materials which can be used to develop MRCI suitable for 3D and 4D printing applications;

2. Investigate the category of components which would be important for the design of smart materials compatible with 3D printing that can add 4^{th} dimension, and have the potential to overcome current 3DPC challenges;

3. Evaluate the influence of ferromagnetic powders/slurries on magnetorheological response and potential interactions in portland cement systems with fly ash systems and nano-particles;

4. Explore the pathways for beneficiation of Class F fly ash and separation of high ferrous fly ash components for the application in MRCI;

5. Characterize the simulated lunar regolith for the potential 3D printing applications on Moon;

6. Investigate the properties of cement based materials when cement is replaced with large volumes of lunar regolith powders and aggregates based on lunar regolith sand;

7. Propose the design philosophy and evaluate the auxetic concrete elements ready for 3D printing applications using developed MRCI.

1.2 Thesis Outline

The research presented here follows the systematic approach to achieve the above listed objectives. This approach is outlined in Fig. 1.1. Chapter 1 and 2 give the introduction and background of this research. Chapters 3, 4 and, 5 report the materials used, methodology, experimental results and discussion for the problem defined in the first two chapters. Last chapter draws the conclusions from the results and discussions and further briefly states the scope for future investigation.

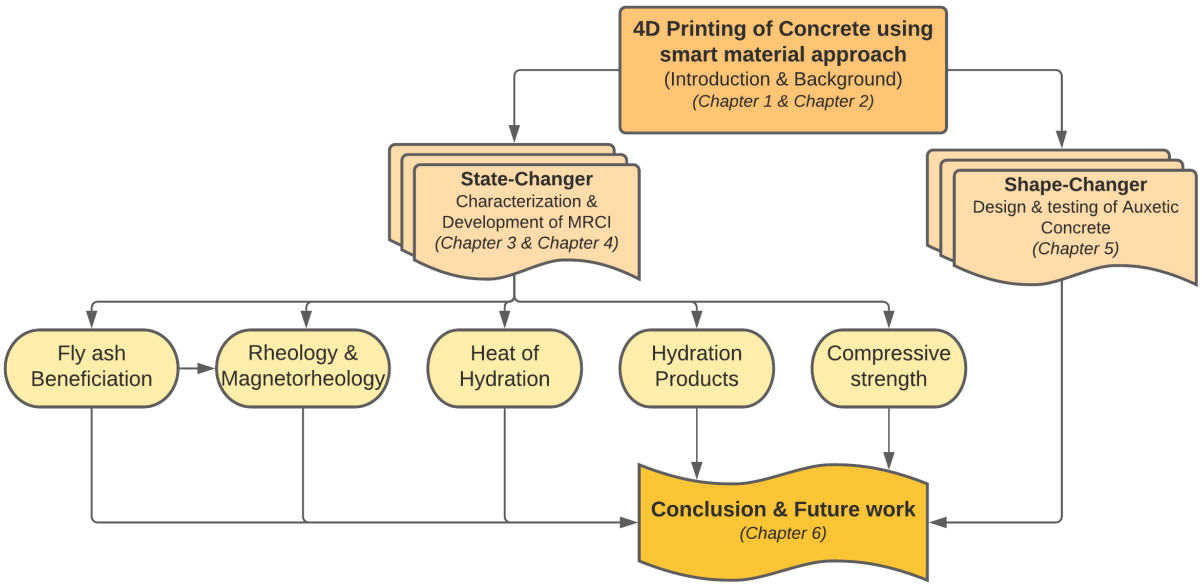


Figure 1.1: Thesis outline

Chapter 2

Literature Review

2.1 Additive manufacturing technologies

The 3DP refers to an automated additive manufacturing or rapid prototyping process in which three-dimensional objects are created by laying down successive layers of a material [5]. As the name states it is an additive process of laying successive layers of material to create or build up an object [6, 18, 19]. The first 3-D printer, using stereolithography technology, was developed by Charles Hull in 1986 [6, 18]. Traditionally, the use of 3-D printing was restricted to the prototyping and manufacturing sectors. The process was used to produce prototypes with low production volumes, small part sizes and complex designs. While 3DP was used only for rapid prototyping in manufacturing sectors, there were a few attempts that used construction-related materials demonstrating its application in construction industry. Later in 1998, stereolithography, was used to produce ceramic 3D parts [19]. As technology improved, in recent years the use of 3-D printing has been expanded to construction products other than ceramic products. In 2001, contour crafting demonstrated that it could be used to produce plaster parts if forced drying by heating was adopted [20, 5]. In 2008, the research team at Loughborough University took an initiative to develop a 3D concrete printing process that can produce free-form building element [19]. These pilot studies demonstrated that 3-D printing technologies could be used to produce construction components when appropriate quality control strategies were adopted.

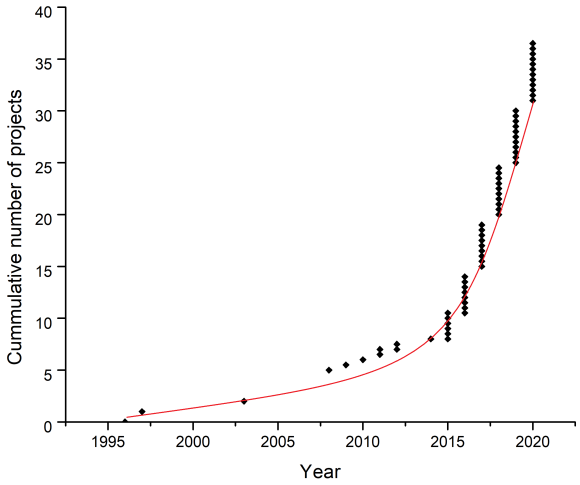


Figure 2.1: The 3DPC projects implemented in last two decades [1]

The Fig 2.1 shows the increase in number of 3D printing projects in last two decades, demonstrating a significant increase in last 5 years. The 3D printing is not only limited to print geometrically complicated concrete products but also can be used to print a larger structures such as houses, apartments and bridges. Engineers and researchers are working towards establishing a reliable 3DP technology which would help in expanding the scope of 3DPC applications such as affordable, accessible housing [21, 22], emergency and natural disaster relief shelters [23, 24, 25, 26].

Table 2.1: Comparative cost estimates for construction of a wall with 40MPa concrete using conventional method and 3DPC [5]

	Conventional construction			Concrete 3D printing		
	Cost	Quantity	Price	Cost	Quantity	Price
Supply of concrete	\$200/m^3	150 m^3	\$30,000	\$250/m^3	150 m^3	\$30,000
Pumping	\$20/m^3	150 m^3	\$3,000	\$20/m^3	150 m^3	\$3,000
Labor	\$20/m^3	150 m^3	\$3,000	-	-	-
Formwork	\$100/m^2	1500 m^2	\$150,000	-	-	-
Total			\$186,000			\$40,500

% Total reduction in cost = 78.22%

The 3DPC technology offers many potential advantages to the construction industry. Its viability can be defined in various aspects such as materials, structural design, process efficiency, labor, logistics, environmental impact, and cost. The 3DPC enables structural optimization, architectural freedom, eliminating formwork, rapid construction ability, saving labor and reducing transportation costs. This technology has a potential of reducing around 70% of labor cost and also reducing a number of injuries and fatalities onsite [27, 28]. It is also capable of saving about 30-60% on raw materials by reducing the construction and industrial wastes due to automation and shape optimization [19, 18, 20]. Table 2.1 provides the cost comparison for construction wall using 40 MPa concrete and conventional construction method and 3DPC. Here, 3DPC can cut down the construction costs up to 78% and reduce labor and formwork costs to almost zero [5]. In addition to these benefits, 3DPC technology can have a significantly positive impact on the environment by lowering the material consumption, energy use, emissions and waste over the life cycle of the structure. As it was reported, the construction industry accounts for the use of 40% of the world's material resources, energy consumption and solid waste generation, and is responsible for 38% of greenhouse gas emissions [29, 22, 30]. The 3DPC has a potential to reduce these environmental impacts by up to 50% as compared to conventional construction [29, 22]. However, currently, the application of 3D printing in construction industry is limited, as current codes and standards, designed for conventional concrete construction are not considering 3DPC.

2.2 Challenges in current additive manufacturing technologies

Inspite of the potential benefits of 3DPC over conventional construction, 3D printing has few limitations and challenges such as:

1. Lack of commercially available cementitious materials and mixes, concrete inks opti-

mized for 3DP;

2. Lack of standard specifications for 3D printing, including rheological properties;

3. Limitations in the ability to incorporate the reinforcement into 3D printed structures;

4. High equipment and technology cost.

It is expected that by addressing these challenges, 3-D printing can reach its maximum potential in the construction industry. This research focuses on addressing first two challenges.

2.3 Why 4D printing of concrete?

The 4D printing can be defined as 3D printing (or additive manufacturing) with smart materials, including new "ink" types [7]. There is no 4D printer, and 4D printing is not an evolution of 3D printing, instead it is an evolution in the use of 3D printing as technology is extended to metamaterials. The 4DP is a promising technology that is still at the Innovation Trigger stage in the latest hype cycle. The 4D printing is the additive manufacturing of multi-material, including particularly smart materials, of three dimensional objects; the 4th dimension being in reference to the ability of such objects to change their properties (shape, physical properties, etc.) and, potentially, their functionality after being printed [7, 31]. The additional dimension only refers to the ability of a 3D printed item to switch its geometric configuration (including surface morphology) from one to another in a fully controllable manner. When a smart material is used in AM, the change to physical or chemical properties undergone by the application of a stimulus can be considered a change over time, and thus 3D-printing with SM is thought of as '4D-printing' (Fig.2.2). This notion was first explored and described by Skylar Tibbits, MIT in 2013-14 [31, 32], and continues to be a subject of interest in a broad array of manufacturing and research sectors [33, 34, 35].

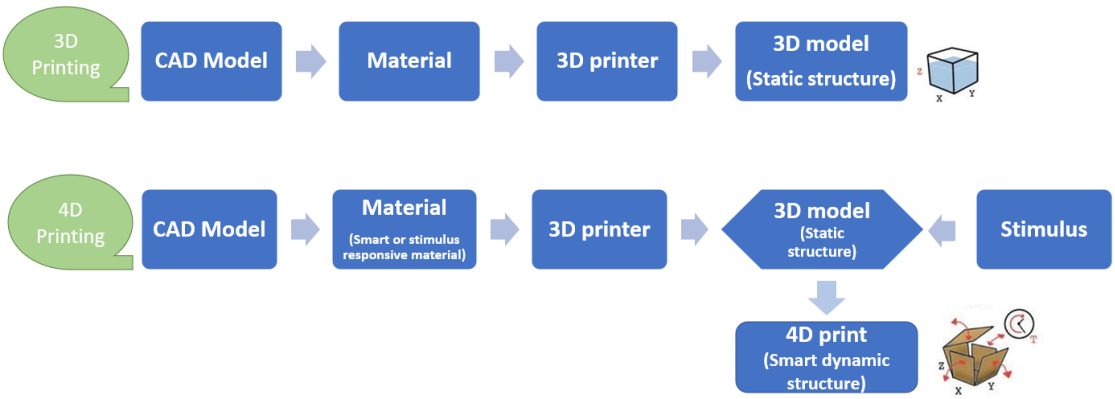


Figure 2.2: The schematics explaining 3D and 4D printing process

The current 4D printing market share stands at USD 130 million (Fig.2.3) and is expected to rise to USD 538 million by 2025 [36] with majority of this contribution attributed to biomedical applications. Constant efforts have been made by many researchers all over the

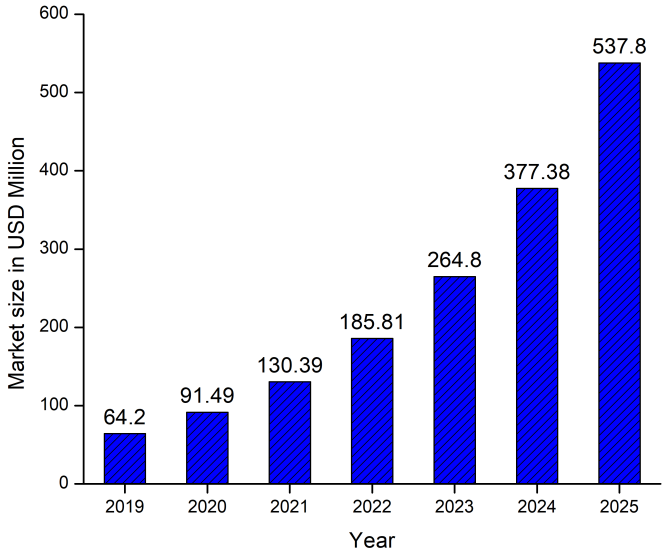


Figure 2.3: 4D printing market size in USD Million since 2019

world, to commercialized this technology to overcome current 3D printing limitations and emerging into next generation AM technique. Construction industry is one of the fields, where smart materials can be used to produce dynamically smart structures by applying external stimulus. Here, further section will discuss the engineering of smart materials used

for 4D printing of concrete.

2.4 Requirements of concrete for 3D printing

Conventional concrete is often characterized using on three main time periods, namely, fresh state, early hardened state and long term evolution governing the durability. Similarly, 3DPC is designed for all three states as mentioned, but digital concrete specification is different, more extensive challenging. For 3DP, the fresh state needs more attention as related properties are difficult to control and are correlated to the hardened state and overall durability of the structure. This research focuses on fresh state properties of printable mix that plays an important role in successful implementation of 3DPC. The fundamental challenges faced by present state of 3DPC technology in its fresh state are the ability to; pump, extrude and build up the multilayered structure. To excel these abilities, the cementitious mix composition needs to be characterized and tuned based on its rheological behavior. The rheological response of the cementitious mix administers fresh properties such as workability, consistency, flowability, mobility and pumpability [37], furthermore providing a benchmark to optimize the mix for 3DPC. The yield stress and plastic viscosity are the fundamental physical qualities used to determine the rheological characteristics of cement composites. The main and challenging requirement for printable concrete is to have low plastic viscosity during pumping and extrusion and, at the same time, possess high yield stress and plastic viscosity to hold the layers deposited above. In addition to this, the printable mix should possess accelerated setting times, and should be densely packed to avoid layer failure due to porosity and layer deformation. The printing time and pace also play a vital role and these parameters should be in accord with the setting time of the mix to achieve the desirable bonding between the layers. The reported research is successful in determining the mix

composition having desirable rheology for 3DPC. Though determining the rheological characterization of the 3DPC mix is important, but material selection also plays an important role to achieve the desired properties. Unlike conventional concrete, there a limitation in using coarse aggregates, hence, fine aggregates and fine cementitious materials are used in the compositions of the ink. The use of finer composition is desirable for easy flow of mix through the 3D printer nozzle. The current state of concrete 3D printing depends on further optimization of the cement paste, geometric designs [38] to be extruded, process optimization and the mechanical components of the printer. The industry is optimizing cementitious admixtures by utilizing various powders and additives, from superplasticizer to nano-fibers tuned for effective layer-by-layer deposition by utilizing 3D printing equipment [39].

2.5 Magnetorheological response and active control of concrete

In general, magnetorheological fluids (MRF) are the fluids in which suspended micron-sized ferrous particles can align in parallel paths forming a chain, upon the application of magnetic field [40]. The apparent viscosity of MRF increases on the application of magnetic field increasing its apparent viscosity [40, 41]. Magnetic field intensity plays an important role in controlling the yield stress of MRF [3, 42]. Although MR fluids are not common in civil engineering applications, these materials have been used in variety of areas, such as automotive clutches [41], vibration dampers and seismic vibration control [43], cancer treatment [44], prosthetic knee dampers, drilling fluids, body armor, gun recoil systems [41]. In 2014 [3], the concept of MRF based cement paste was studied but there is no real application in 3D printing to date. Due to the above mentioned properties, it is envisioned that cement-based magnetorheological fluids can potentially be used in applications to act as a "set-on-demand" material, allowing the user greater control over the processing such as

mixing, casting, pumping, and deposition of concrete.

From the Section 2.4 review, it is clear that the cement paste and ink rheological response is the most important parameter to characterize the 3DPC mix. In order to meet the requirements of 3DPC, the rheological properties are tuned for successful printing. This presented research deals with the investigation of rheological properties and tuning cementitious ink for smart response. Here, the research focuses on state-changing smart materials exhibiting a change in rheological response under a magnetic field as a stimulus. When a magnetic field is applied to a cementitious ink for 3D printing, fluid paste converts to a solid state. The responsive constituents in the proposed magneto-cementitious inks are micron and nano-sized ferromagnetic components, as well as high-ferrous fly ash powders, resulting in an ink composition sensitive to an applied magnetic field, yielding active control on the rheological behavior and, overall, fresh properties. The advancement of cementitious inks to manufacture smart materials has not been highly explored, yet the properties of MRCI may provide numerous benefits through real-time tuning of the rheological properties of fresh material to manufacture intricate shapes. Instead of focusing on designing the machines to print concrete in the conventional fluid state, modifying the mix composition to include the ferromagnetic components will allow for multiple layers to be incorporated in a 3-dimensional structure. Additionally, this development may lead to the ability to create very complex geometries such as auxetic that are not conventionally possible or feasible using conventional cast methods. The properties of MRCI can be further extended to 3D printing in unconventional environments (e.g., space) where cement slurry is difficult to cure and hold a desired shape.

2.6 Fly ash beneficiation for magnetorheological applications

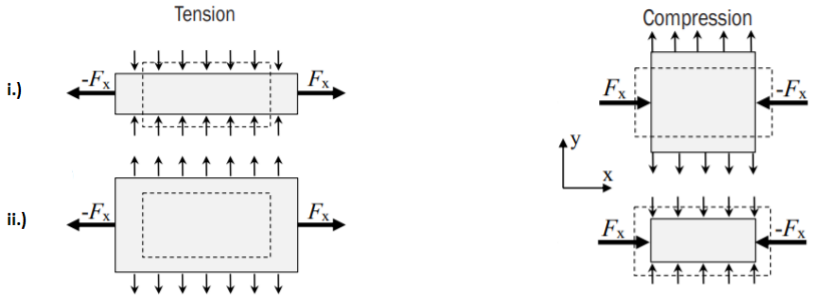
Over the last century, the efficiency of coal-powered energy plants has improved dramatically, and fly ash that is produced by these plants is in high demand by concrete manufacturers. Fly ash has physical characteristics as a fine powder as well as a chemical composition that can be used to effectively replace portland cement and, at the same time, improve the long-term performance of concrete [45]. The manufacture of "pure" cement from raw limestone and other components is energy-intensive, and any opportunity to replace cement with a byproduct is desirable. Current demand for concrete dictates the complete use of freshly generated fly ash and alternative sources of ash are needed to sustain the green concrete benchmark. In this regard, the beneficiation of fly ash which is the process of extracting high purity carbon and pozzolanic and magnetic ash from landfills for re-utilization in various applications was proposed. Longtime UWM collaborative partner, WEC Energy Group (We Energies) explored early innovations for waste ash utilization in cement-based products, but still possesses millions of tons of land-filled ash. Other utilities in the USA had accumulated over tonns of ash. Given the evolution of coal combustion technology, legacy ash is not as pure as contemporary fly ash, although much of the local supply is regarded as "monofill," representing continuous waste-stream (not intermixed with other types) which is a valuable resource. Much of the land-filled product is originated from pozzolanic Class F low calcium fly ash, coming from a bituminous coal source with significantly higher iron content. However, this iron rich fly ash can significantly contribute in the development of MRCI. The iron rich fly ash when used as a replacement of portland cement in the ink composites, can activate the magnetorheological characteristics of the ink and help in achieving higher yield stresses. The presented work demonstrates the feasibility of milling and magnetic separation of beneficiated fly ash to obtain amorphous compound rich (non-magnetic content) and

ferrous rich (magnetic content) powders and slurries for further application of MRCI (see Section 4.1).

2.7 Lunar Regolith: potential for 3D printing

Lunar regolith (LR) is made up of rock mineral and glass fragments that undergoes specific combination of extraterrestrial weathering processes. It composes of lunar soil, covering the Moon surface with varying thickness from few centimeters to hundred of meters. Additionally, despite of geological differences observed in lunar geography, collected and characterized lunar materials reveal remarkable uniformity in many physical characteristics [46]. By analyzing the lunar samples returned by the Apollo missions- which represent a variety of materials and geological formations- NASA is amplifying its knowledge of lunar materials and their environment as the agency prepares for a long-term human presence and construction in space. As a follow up part of the Apollo program, a set of standard lunar soil simulants was developed for testing all the systems in preparation for the landings and construction on the moon [46]. Although science still know very little about the variation of the mineral compositions on lunar surface, this method can be very effective for large-scale experiments on Earth.

In 1989 NASA's workshop, Lunar simulants were defined and technical report was published in 1991. Later 2005 workshop hosted by the Exploration Science and Technology, focused on properties and mineral composition of LR. The primary goal of this workshop was to establish the requirements for the production and distribution of terrestrial analogs of LR, that now became the accepted material standard for research and development efforts on space resources utilization technologies [46]. Recently, the European Space Agency (ESA) endorsed the concept of 3D printing to construct the landing base from locally available



(a) Subjected to tension (b) Subjected to compression

Figure 2.4: The deformation of i) conventional material and ii) auxetic material subjected to loading

materials [47]. The 3D printing have potential to facilitate lunar settlement with reduced logistics from Earth. Understanding the need of exploring new possibilities, this research makes an attempt to characterize the simulated LR in addition to the characterization of MRCI for 3DPC. The further details of this work are given in Section 4.2.

2.8 Concrete auxetic structures

Auxetic materials are materials which exhibit a negative Poisson's ratio (NPR). Conventional materials contract in the transverse direction when subjected to uniaxial tensile load, whereas auxetic material demonstrates an expansion in the transverse direction on the application of uniaxial tensile load, Fig 2.4a and Fig 2.4b [8]. Though this phenomenon is called auxetic response and, however, this unusual behavior is not due to the material itself, but rather due to geometrical arrangement of certain shapes and inclusions. Here, the macroscopic mechanical properties of the system are expected to be governed primarily by the geometrical structure of the system rather than by its material composition. Auxetic materials with NPR can be achieved from the cumulative behavior of repeated functional units when arranged in a specific order.

The internal structure of this material can be designed using a geometrical foam-like

cellular configurations which exhibit an auxetic effect. Auxetic behavior was first studied for honeycomb foam structures by Rodger Lakes [16] in 1987, and it received considerable attention in past couple decades, due to the "unusual" properties and potential applications in fields such as medical and biomedical engineering [48], military devices, aerospace [49], textile and sports applications [15]. There is no reported research on auxetic concrete yet. This thesis demonstrates the design philosophy of auxetic concrete that can be suitable for 3DP using MRCI developed in the presented research work. Further details on auxetic concrete development are explored in Chapter 5.

Chapter 3

Materials

This chapter gives the overview of the materials used in the research program. Cement, supplementary cementitious materials SCM, namely three types of Class F fly ash, nano-alumina, nano-silica, magnetite powder (black pigment), cobalt powder and lunar regolith (LR) are thoroughly characterized and evaluated for application in concrete inks. Section 3.1 provides general information of the materials used such as manufacturer and general specifications. Section 3.2 gives detail characterization of the materials used in this research based on composition, particle size distribution, particle shape and morphology.

3.1 Overview of materials used in research

The materials used in this research are:

1. Portland cement: Type I portland cement (PC) used in this study was supplied by LafargeHolcim. The chemical and physical properties of PC, as tested by the manufacturer according to ASTM C150, are reported in Table 3.1.

2. Class F fly ash: Three types of fly ash, which were pozzolanic and supplementary cementitious materials suitable for concrete as defined by ASTM C618. The main classification of fly ash is based on the combined content of SiO_2, Al_2O_3, and Fe_2O_3; based on ASTM C618, there are two types of fly ash products recommended for application in concrete: low-calcium fly ash (ASTM Class F) used in this research and

Table 3.1: Chemical composition and physical properties of portland cement Type I

Chemical Composition	ASTM C150 Limit, %	Test result, %
SiO_2	-	20.1
Al_2O_3	6.0 max	4.9
Fe_2O_3	6.0 max	3.2
CaO	-	64.1
MgO	6.0 max	2.2
SO_3	3.0 max	2.6
Loss on Ignition	3.5 max	2.1
Insoluble Residue	1.5 max	0.63
CO_2 (from Limestone)	-	1.3
$CaCO_3$ in Limestone	70 min	95
C_3S	-	58
C_2S	-	14
C_3A	8 max	7
C_4AF	-	10
$C_3S+4.75C_3A$	-	93
Na_2Oeq	0.6 max	0.52
Physical Properties	**ASTM C150 Limit**	**Test Result**
Air Content, %	12 max	8
Blaine Fineness, m^2/kg	260 min	375
Initial Setting Vicat, minutes	45-375	130
Compressive Strength MPa		
1 day	-	11.8
3 days	10 min	23
7 days	17 min	29.4
28 days	-	37.5
Heat of Hydration, kJ/kg (ASTM C1702) 3 days		247

high-calcium fly ash (ASTM Class C). Three different Class F fly ash, namely Oak Creek, LG14 and Prairie State products were used in this research. Oak Creek ash was produced by WE Energies and is represented by a pozzolanic material consisting of an amorphous silicate glass modified with aluminum and iron. LG14 product was provided by Prairie State ash was provided by LafargeHolcim and verified at Advanced Analytical Facility (AAF) at UWM. The chemical composition and physical properties of class F fly ash products are given in Table 4.1.

3. Nano-silica: Nano-sized particles of silica were proposed to increase the strength and durability of concrete [50]. Nano-SiO_2 with a particle size between 5 and 50 nm was used as a viscosity modifying agent at a dosage of 0.25% (or less) by mass of cementitious materials [50, 51]. The addition of nanosilica in self-consolidating concrete tends to increase the viscosity and reduce the setting time in pastes. It has been observed that the use of nano-silica in cementitious materials can generate a denser packing of hydration products, a refinement of the pore structure and improved interfacial transition zone [50, 52, 53, 54]. The Cembinder 50 (CB50) colloidal nanosilica product, supplied by EKA Chemicals, was evaluated and utilized in this study. The CB50 product is characterized by an average particle size of 5 nm, and a solid concentration of 15%. At a dosage of up to 0.5%, nanosilica product acts as an effective viscosity modifying agent and also early strength enhancer [54].

4. Nano-alumina: The nano-alumina (NA) fibers used in this research were provided by ANF Development. The product with a surface area of 155 m^2/g was found to be in chemically crystalline form of γ-Al_2O_3 [55]. The single crystal tensile strength of the fiber is 12 GPa (1740 ksi), while the modulus is 400 GPa (58000 ksi). The typical fiber diameter is 10-20 nm, and it was delivered in disks (pucks) with fiber lengths of

50 mm (Fig 3.1). The fibers are synthesized from an aluminum melt and then grown up to 50 mm length [52].

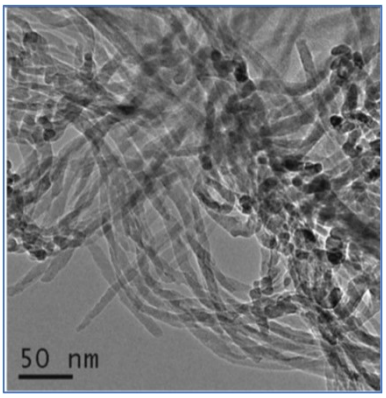


Figure 3.1: The TEM of nano-alumina fibers [2]

5. Magnetite powder (black pigment): Magnetite powder (MP) used in the research was black pigment supplied by Real Milk Paint. It is characterized by a presence of ultra-fine submicron sized particles and agglomerates of approximately 300 nm.

6. Cobalt powder: The cobalt metal powder used in this research is supplied by Chemcraft Ltd. company from Russia. The cobalt powder was used as a strong ferromagnetic agent to induce the magnetorheological response in the MRCI compositions.

7. Superplasticizer (SP): Superplasticizer (SP) used in this research is commercially available polycarboxylate ether (PCE) product Megapol supplied by Handy Chemicals with 38.7% solid concentration; this SP was selected after the evaluation of several PCE products based on its ability to disperse NA fibers. This SP PCE was used at a dosage of 0.15% of a total binder weight, except in the compositions with NA fibers, which already contained an effective surfactant (similar to PCE SP used in this research) and so required a reduced dosage of 0.05%.

8. Lunar Regolith: Simulated lunar regolith sourced from Uplift Aerospace was received

in a number of batches, the first considered the reference (control) sample named LR1. The subsequent batch (LR2) included coarse sand and powder fine samples. In order to test consistency or variance in texture, composition, and particle size distribution among supplied products, samples were identified as 'LR2 C1' – 'LR2 C6' for coarse sand samples, while fine powder samples were designated, 'LR2 F1' – 'LR2 F6'. A series of standardized materials characterization experiments were undertaken on these samples in order to qualify and quantify their suitability in concrete systems, both as aggregate and cement replacement reactive powder material. The details of this investigation are further described in Section 4.2.

9. HDPE fibers: The HDPE fibers used in this research have a density of 970 kg/m^3, a length of 12 mm, a diameter between 12 and 21 µm, an axial tensile strength of 3.6 GPa, and an axial tensile modulus of 116 GPa. These fibers are used as a reinforcement in auxetic concrete as discussed in Chapter 5.

10. Fine aggregates (sand): Standard Ottawa sand conforming ASTM C778 was used in this research as a reference sand for the preparation of mortars. This sand is graded so that 96% of the aggregates fall between the No. 30 and No. 100 sieves.

3.2 Material characterization

3.2.1 Particle size distribution

The particle size distributions (PSD) of powdered materials were determined using the laser diffraction according to ASTM D4464-10. This test method is capable of measuring the equivalent spherical diameter for particle sizes in the range of 1 to 300 µm. To conduct the laser diffraction test, a sample of material is dispersed in distilled water or a compatible

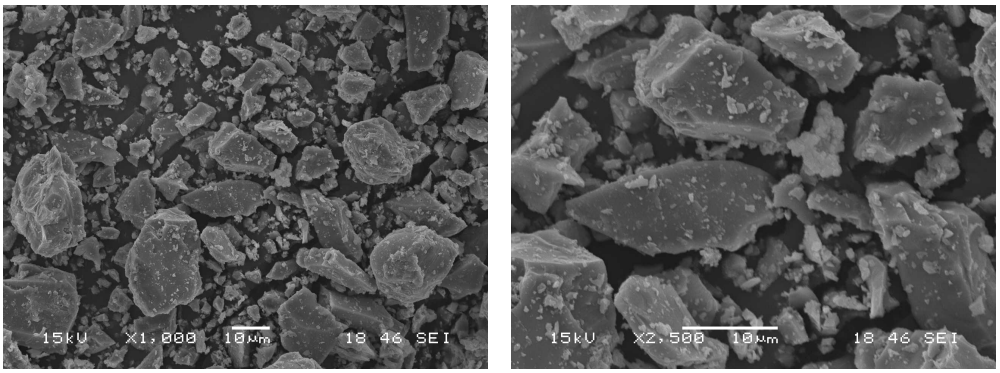
organic liquid (alcohol) and circulated through the path of a laser light beam. When the light beam hits a particle, it is scattered. This scattered light is then collected by a photo detector and converted to an electrical signal and analyzed with the assumption that all the particles are spherical. From the PSD curves, fineness modulus, particle sizes corresponding to 10, 50, and 90% passing, named D_{10}, D_{50} and D_{90} can be determined. The fineness modulus (FM) is used as a single value derived from the PSD and determined by dividing the sum of the percentages of Passing No. 200 size material coarser than 75, 50, 30, 20, 10, 5, 3, and 1 μm by 100. The diameters D_{10}, D_{50} and D_{90} correspond to the portions of the material that are 10%, 50% and 90% finer respectively. The PSD of more coarse powder materials such as cement and fly ash was determined using Malvern Panalytical Mastersizer 3000 as reported in Table 3.2; furthermore, for magnetic powders; such as magnetite and cobalt, particle size was determined using zeta sizer and electron microscope, respectively. The average size of magnetite powder as reported using zeta potential is 1.7 μm, whereas cobalt particles were smaller, ranging from 1 to 2 μm with a strong tendency to agglomerate.

Table 3.2: Particle size for cementitious materials

Raw Materials	**Particle size, micron**		
	D_{10}	**D_{50}**	**D_{90}**
Cement	7.63	20.7	58.4
Class F fly ash Oak creek	6.85	29.2	92.4
Class F fly ash LG14	8.35	28	96.3
Class F fly ash Prairie state	7.82	20.8	59.9

3.2.2 Particle shape and morphology

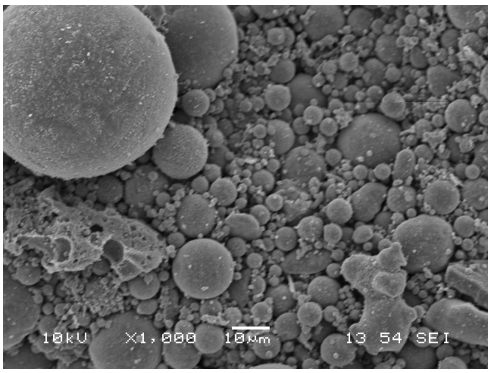
A Scanning Electron Microscope (SEM) was used to evaluate the shape and particle size of powders. A small amount of cementitious material was adhered to double sided carbon



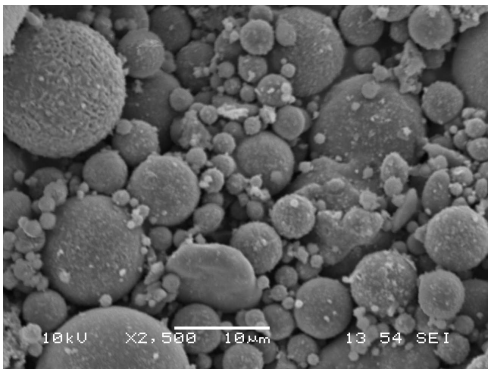
(a) (b)

Figure 3.2: SEM of portland cement:(a) x1000 and (b) x2500

black tape which was attached to a sample holder. The sample was then sputter coated with a thin layer of gold to make it electrically conductive. Once properly aligned, the SEM was focused and images were taken. Figures 3.2 to 3.3 demonstrates the features of "classical" portland cement and fly ash as defined by ASTM C618. To demonstrate the particle size range, a magnification of 1000x and 2500x was used. As observed in the PSD tests, SEM images confirm that, in general, Class F fly ash had smaller particles than portland cement. Figure 3.2 proves that cement particles have angular and irregular shapes, whereas, fly ash products have spherical shape particles with smooth surface and dense structure (Figure 3.3). The Figure 3.4 demonstrates SEM images of the fine LR sample of two different types and it confirms that the particle shape and size are almost same for all the fine LR samples. The LR particle sizes are irregular; however, particle shape is similar to observed for portland cement particles. The Magnetite and cobalt powders have the smallest particles, and are highly agglomerated. As powder particles get finer and so difficult to separate the exact size and shape are difficult to detect under the SEM. However, it is clear from the images that cobalt powder is finer than the magnetite powder, still with considerable agglomeration (Figures 3.6 and 3.7).

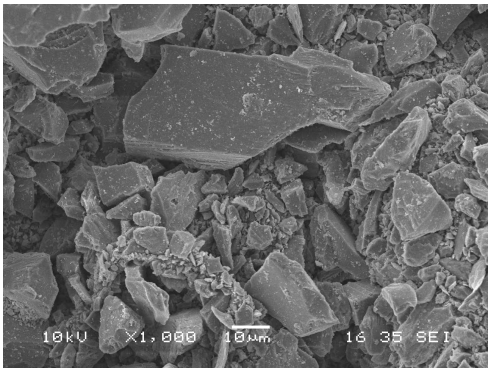


(a)

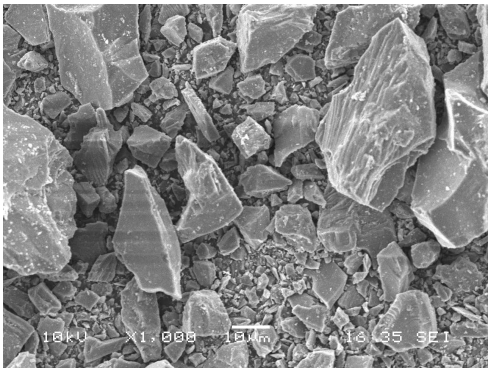


(b)

Figure 3.3: SEM of representative Class F fly ash (Oak Creek):(a) x1000 and (b) x2500

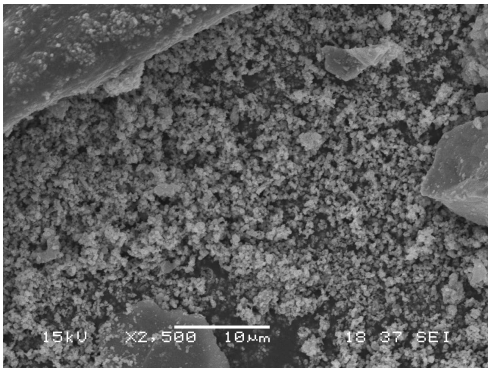


(a)

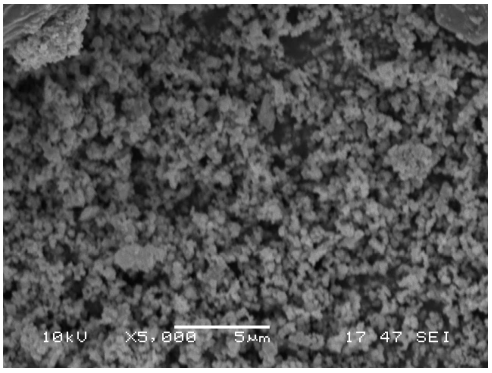


(b)

Figure 3.4: SEM of Lunar regolith at X1000: (a) fine LR sample and (b) fine LR sample F6



(a)



(b)

Figure 3.5: SEM of magnetite powder: (a) x2500 and (b) x5000

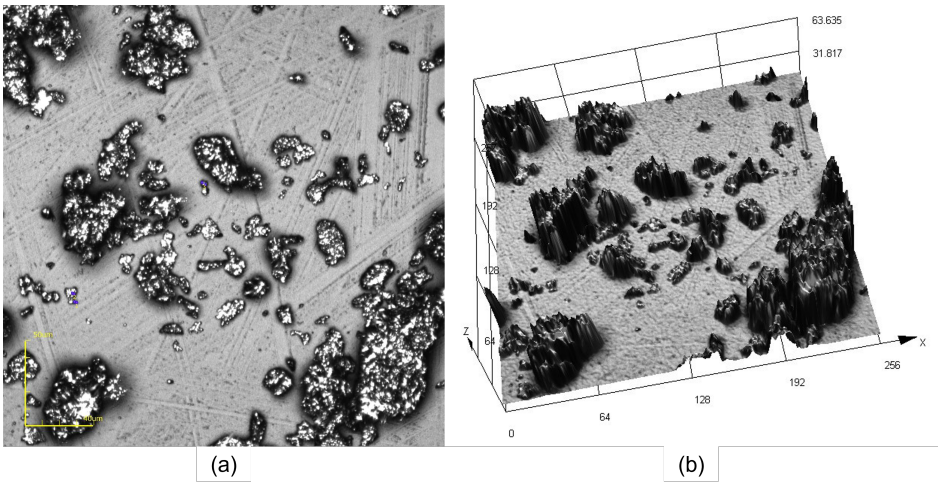


Figure 3.6: Images of cobalt powder under confocal microscope: (a) 2D image and (b) 3D image

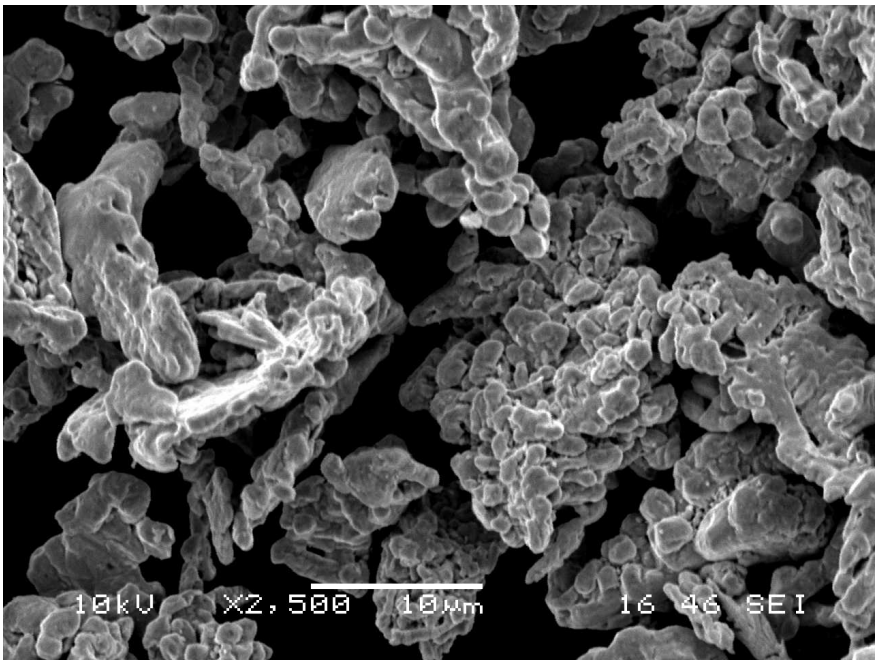


Figure 3.7: SEM of Cobalt powder

Chapter 4

Test methods and experimental results

4.1 Fly ash beneficiation

While current "clean coal" technology is highly efficient and fresh waste ash streams are utilized almost in their entirety, this was not the case in past when landfilling of waste ash was a standard procedure for the majority of coal power facilities. As such, tremendous amounts (more than 1bn tons) of coal ash remains deposited in the landfills, containment ponds, and brownsites throughout the country. Coal burned prior to the 1980s tended to be sourced from East Coast bituminous and anthracite coals that produced pozzolanic "Class F" fly ash with high iron content, while coals burned in more recent decades tend to be sub-bituminous or lignite resulting in cementitious ash product with higher calcium content, known as "Class C." Both types are beneficial as supplementary cementitious materials for concrete, but ash found in landfills has considerable variability in composition and a greater proportion of unburned carbon due to the lower efficiency standards of past years. Various components of aged fly ash can be separable by density methods as lighter coal particles can be separated from heavier iron-containing phases using a cyclone beneficiation. This project was intended to utilize the vast quantities of landfilled and ponded ash by further developing separation processes, and utilizing the components as burnable fuel, fly-ash slurry for concrete, and to incorporate high-iron product into cementitious inks such as MRCI intended for 3D-printing of concrete. The beneficiation of waste ash monetizes environmental cleanup operations by

reclaiming old landfills and turns these liabilities deposits into valuable byproducts with significant revenue streams. One of the barriers to large-scale implementation of 3DPC is the precise balance between the workability, pumpability and the material's capability to set on demand, providing a base for placement of forthcoming layers. The MRCI materials stand to fill this niche quite well – the ability to add near-instant setting and improved green strength can revolutionize this highly sought-after technology. Of primary importance to the project is further advancing the technology of magneto-rheological 3DPC and demonstrating the value of high-iron ash byproducts in the emerging market.

4.1.1 Demand for fly ash beneficiation

As a part of this research, I-Corps customer discovery interviews were conducted via telephone questionnaires with firms currently involved in 3DPC of domiciles, with ready-mix operators and national admixture supply company executives, and within the network of industry leaders specializing in fly ash byproduct utilization. The research team conducted interviews with a variety of young engineers, senior engineers, and managers leading the U.S. construction industry, and supplemented this research with questionnaires of executives and decision-makers in local and national firms, as well as leaders in industry associations and societies. The need for sustainable solutions for cement and concrete industry, including the use of fly ash and other Supplementary Cementitious Materials (SCM) was identified. Based on the survey results, the team decided that for sustainable concrete solutions, the best customer segment to target would be the companies that supply concrete, cement, fly ash, and chemical admixtures. These companies can be early adopters of proposed technology to manufacture and supply a broader range of fly ash based products for construction and infrastructure maintenance, including the beneficiated ash and inks for 3D printing.

The discussion with a major ready-mix firm triggered a serious interest in exploring this new approach in fly ash delivery and utilization. While most ready-mix producers are not presently investing in 3DPC technology, they – like most other industry leaders – acknowledged the inevitability of 3DPC to become a significant market opportunity. Through these discussions, it was realized that the landfills and ponds owned by utility companies represent significant financial liabilities – especially older landfills constructed prior to strict environmental guidelines.

Based on the additional 10+ interviews geared toward modern construction, recent developments are further inspired by flourishing digital concrete based on 3DPC technology, which requires tailor-made concrete mixtures. Findings of the refined survey indicate that current manufacturing incorporates essentially '2D-printing' of concrete at an industrial scale, and numerous attempts to add a 3rd dimension over the conventional slab thickness have resulted in incremental developments comparable to 2D slip-forming processes used for mass concrete. Here, the MRCI tuned for applications in 3DPC can be a viable solution for modern construction. This MRCI innovation addresses the identified need to "improve the rheological response and control of concrete used in 3D printing". The proposed MRCI can be used for rapid construction helping to utilize the potential of additive manufacturing. In addition, developed fly ash products can provide accelerated strength development and incorporate smart capabilities into the next generation of buildings and infrastructure.

According to the market analysis, in 2025, the global green cement and fly ash markets are expected to reach $40bn [4]. The availability of decent quality SCM is limited and cannot offset the need for higher volumes of cement and concrete as required by green standards and developing markets. In this regard, one viable alternative can be the use of alternative SCM, including off-spec products [45]. The beneficiated ash products and MRCI provide a

strong opportunity for utilizing the sources from impoundments and landfills.

4.1.2 Type and chemical composition of fly ash

Three types of class F fly ash were used in this study, namely, Oak Creek fly ash, Prairie State and LG14. The Table 4.1 reports the chemical composition and physical properties of Class F fly ash. All the three fly ash products meet the chemical requirements according to ASTM C618, where SO_3 content is less than 5% and the sum of SiO_2+Al_2O_3+Fe_2O_3 is at least 70% . These fly ash products were selected for this research on the basis of high ferrous content, and the Oak Creek fly ash had the highest ferrous content of 19.2%.

Table 4.1: The chemical composition and physical properties of Class F fly ash

Chemical Composition	**ASTM C168**	**Class F Fly ash, %**		
	Limit, %	**Oak Creek**	**LG14**	**Prairie State**
SiO_2	-	46.9	46.3	55.04
Al_2O_3	-	22.9	26.0	18.22
Fe_2O_3	-	19.2	16.9	11.49
Total, SiO_2+Al_2O_3+Fe_2O_3	> 70	89.0	89.2	84.76
SO_3	< 5.0	0.3	1.5	0.72
CaO	-	3.8	2.8	6.38
MgO	-	0.8	1.3	1.53
K_2O	-	1.7	2.8	2.63
Na_2O	-	0.6	0.8	1.15
Loss on Ignition	< 6.0	2.3	2.0	0.52
Physical Properties				
Specific Gravity	-	2.5	2.6	2.39
Strength activity index, % of control at 7 days	> 75	77.5	77.5	78
Water Requirement, % of control	< 105	102	58	98.3

4.1.3 Milling procedure and magnetic separation

Previous study reported that milled fly ash with higher surface area and chemical reactivity can result in an improvement of mechanical performance [56, 57]. Milling of fly ash results

in the formation of ultrafine particles which are more compatible for replacing cement. In

Table 4.2: Compositions used for fly ash milling

Materials	Proportions by weight (g)	
	Test batch	Bigger batch (X10)
Fly ash	350	3500
Grinding media	3500	35000
Water	350	3500
SP	1	10

this study, all three types of fly ash were milled for one, two and three hours to study the efficiency of milling technology. All fly ash products were wet milled using SWECO vibro energy grinding mill (Fig.4.1) operating at a frequency of 60 HZ. The grinding media plays an important role in milling. Here, steel balls of $3/8^{th}$ diameter were used for milling. To increase the resistance of the inner walls of the vibrating mill, it is made up of polyurethane rubber material. Fly ash is ground by the abrasion between the grinding media, producing finer particles. The wet milling used in this research, is less energy intensive process than commonly used dry milling and has a potential to produce ultrafine particles at an industrial scale. Initially, 1000 ml plastic bottle chamber was used for testing a milling efficiency in the vibratory mill. Fly ash, water, grinding media and superplasticizer (SP) were added to the bottle in the quantities given in Table 4.2 in the small test batch. This experiment was repeated for each of the three types of fly ash and for three different durations (1 hour, 2 hours and 3 hours). After milling of each sample, it was magnetically separated using a permanent magnet with a design as shown in Fig.4.2. This simple device was designed with 8 slots for bar magnet along the periphery and one round magnet at the bottom. To realize the separation, the bottle is placed in the device, and, due to magnets at the periphery and bottom, magnetic particles align around the inner periphery of the bottle and so non magnetic slurry can freely flow. Therefore, the non-magnetic slurry can be collected,

separating the magnetic paste and non-magnetic slurry. Material balance, particle size distribution and mineralogical composition of individual ash fractions were evaluated for all the samples. Further, these beneficiated slurries were tested in cement compositions at 10% replacement to determine the rheological and magnetorheological response and effects of these products on cement hydration.

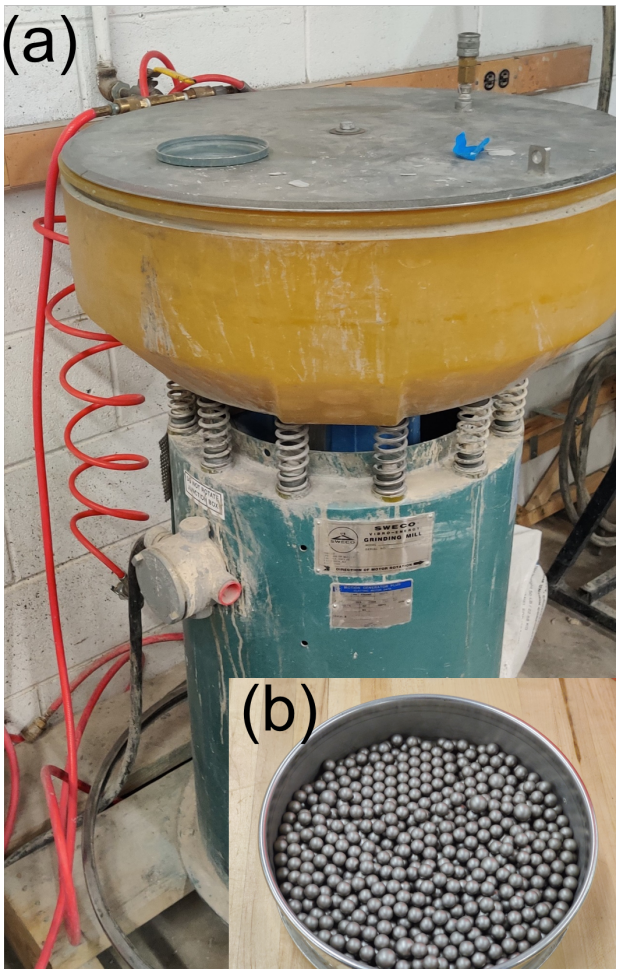


Figure 4.1: (a)SWECO vibro energy grinding mill used for wet-milling of Fly ash (b) milling balls/ used as grinding media

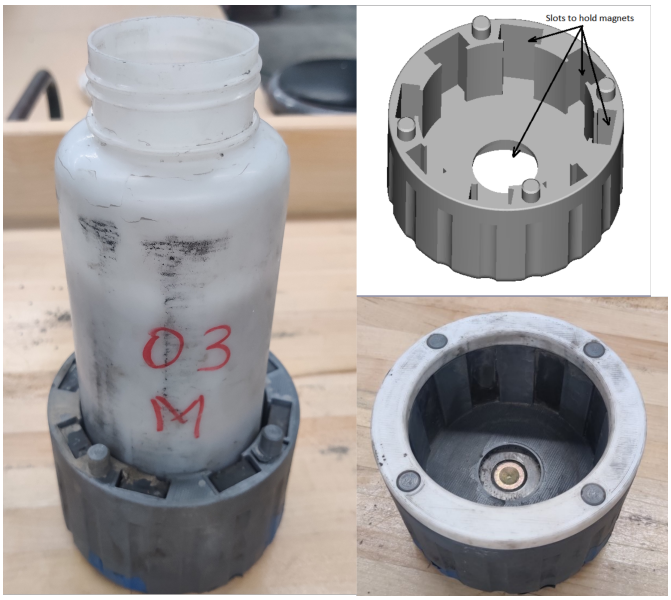


Figure 4.2: Magnetic separation setup used for separation of milled fly ash

4.1.4 Material balance for milled and magnetically separated fly ash

Fig. 4.3 represents the material balance for each type of fly ash after milling for 1 hour, 2 hours and 3 hours. The initial Fe_2O_3 content in Prairie State, LG14 and Oak Creek material was 11.49%, 16.90% and 19.20%, respectively. After milling for 1 hour and magnetically separating, the magnetic content in Prairie State, LG14 and Oak creek is 26.5%, 30.3% and 60.4%, respectively. The Oak Creek class F fly ash had the highest percentage of ferrous (magnetic) content in the milled slurry. With the increase of the milling time, the magnetic content in the slurry reduces indicating effective milling and particle size reduction. Fly ash particles are spherical and with increasing of milling time, the particles break into finer particles, enabling the harvesting of the iron rich but still reactive powders. Hence, with increase milling time, the volume of magnetic products in the slurry is reduced.

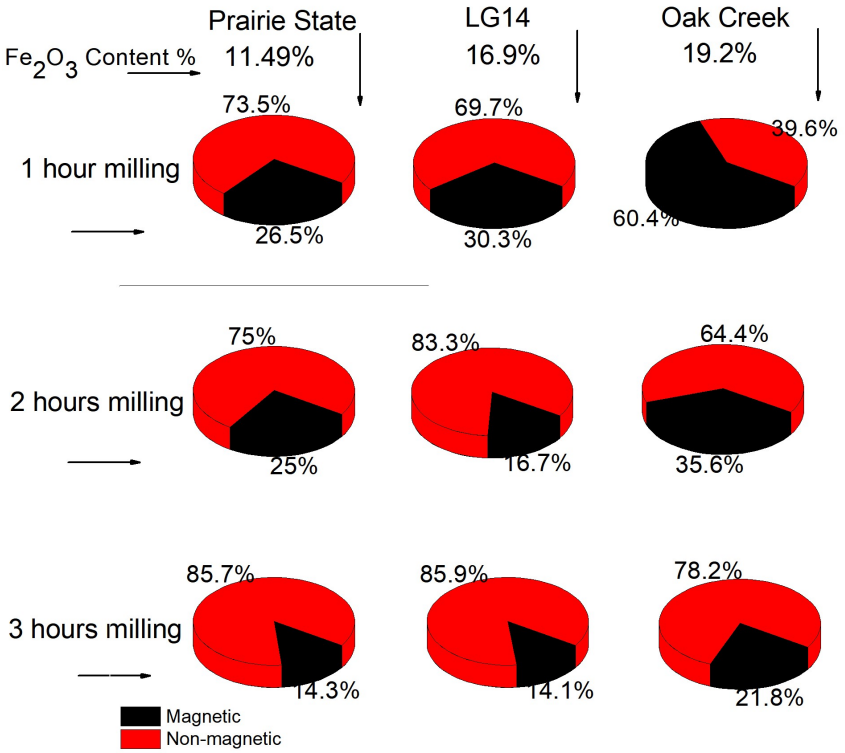


Figure 4.3: Material balance after milling each Prairie State, LG 14 and Oak Creek class F fly ash for 1hr, 2hrs and 3hrs, respectively.

4.1.5 Characterization of milled and beneficiated fly ash

To understand the efficiency of milling process and beneficiation, it is important to characterize the milled slurry in terms of particle size distribution, mineral composition and oxide composition. The section below describes the effect of milling on particle size reduction of the fly ash.

Particle size distribution

Fly ash particles are spherical in shape (Fig. 3.3) and, upon milling, the particles are observed to transform into ultrafine particles. It is generally considered that, up to some limit, the particle size is reduced with increase in milling time. The particle size was determined using Malvern Mastersizer 3000. The Fig. 4.4 reports on the particle diameter corresponding

to 10, 50 and 90% passing for Oak Creek fly ash, milled for up to three hours. Each milled sample was separated into magnetic and non-magnetic phase. Hence, particle size for each milling time is evaluated for unseparated, magnetic and non magnetic samples. Magnetic particles have a larger particle size as compared to non magnetic particles. The D_{90} value of unmilled Oak Creek fly ash is 92.4 μm, which is reduced by 82% after 3 hours. Similarly, D_{10} and D_{50} values are reduced by 42 and 70%, respectively after 3 hours of milling. This demonstrates that the large particles which attribute to 90% passing are crushed down to smaller particles reducing corresponding passing size. It is also observed that the main percentage reduction in particle size is happening after 1 hour, and 2 and 3-hour results in milling with lesser efficiency. Hence, after 2 hours, most of the particles are already in its finest form and further milling is not effective. The Figure 4.5 reports the D_{10}, D_{50} and D_{90} values for

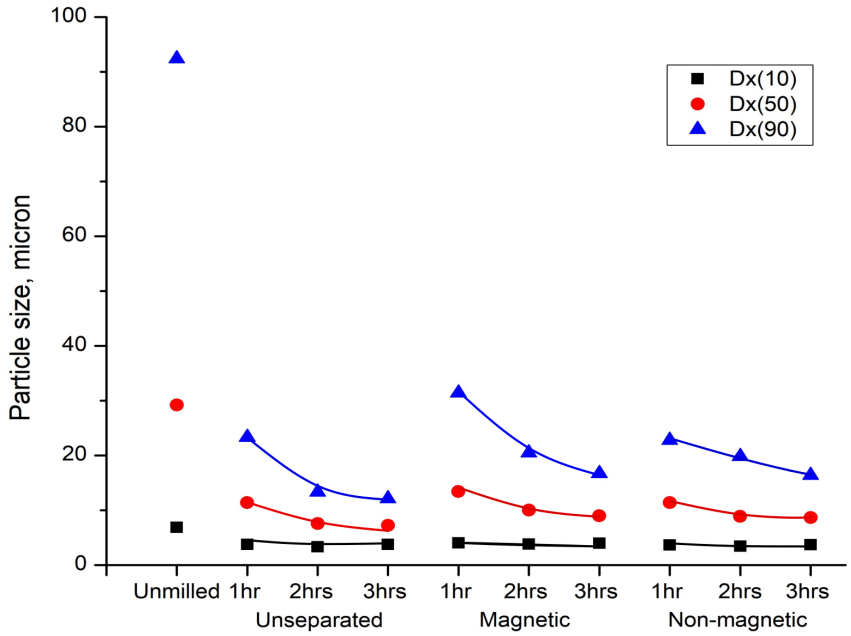


Figure 4.4: Particle size of Oak Creek fly ash milled for 1hr, 2hrs and 3hrs

LG14 fly ash. The LG14 ash particles appear to be larger than Oak Creek product. After 3 hours milling for LG14, the percentage reductions in D_{10}, D_{50} and D_{90} values are 48%, 63% and 79%, respectively. The Prairie State fly ash is finer than Oak Creek fly ash. After 3

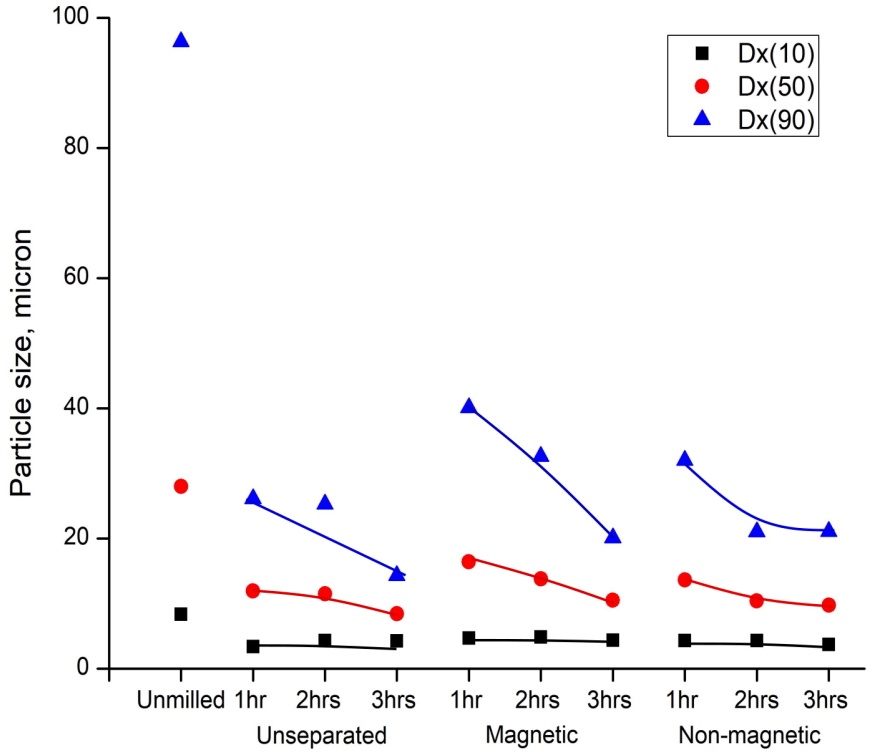


Figure 4.5: Particle size of LG14 fly ash milled for 1hr, 2hrs and 3hrs

hours milling, the percentage reductions in D_{10}, D_{50} and D_{90} values are 47%, 50% and 68%, respectively. This proves that the large particles which attribute to 90% passing are crushed down to smaller particles reducing the corresponding passing values. It is also observed that the main reduction in particle size occurs already after 1 hour milling, with smaller reduction observed after 2 hours and 3 hours milling. Hence, after 2 hours, the reduction is not achieved as the most of the particles are already in the finest form and further reduction is not achieved. The surface area of the particles is inversely proportional to the particle size. Hence, milling increases the surface area contributing towards the reaction ability of the powders. Smaller particle size and greater surface area help to develop denser matrix with lower permeability. These properties make activated fly ash a better product for the production of concrete for a wide range of applications.

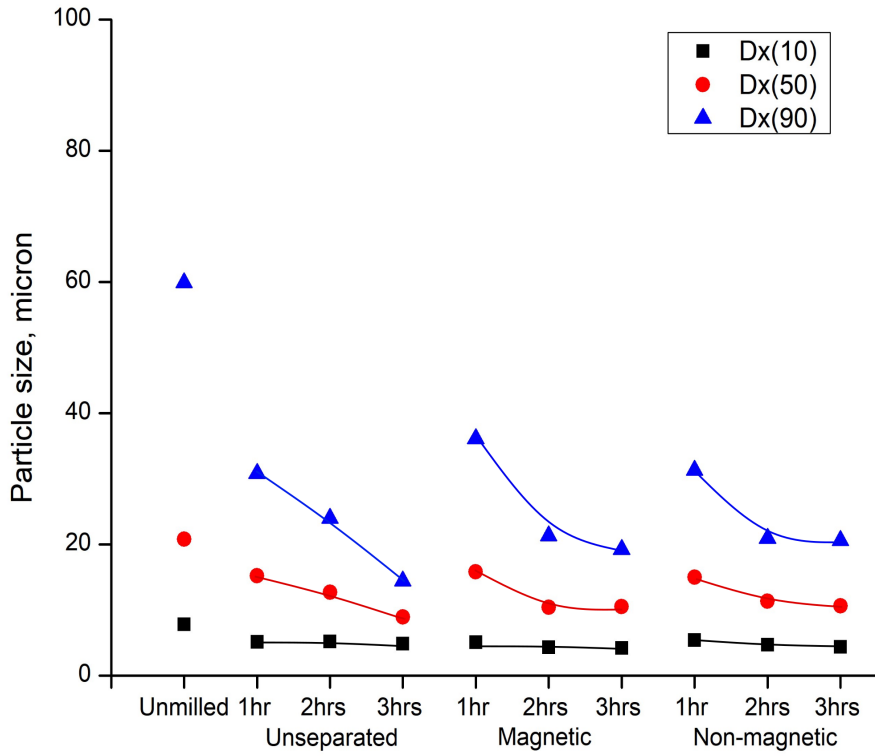


Figure 4.6: Particle size of Prairie State fly ash milled for 1hr, 2hrs and 3hrs

Mineral composition

The mineral composition of the Class F fly ash was determined using X-Ray diffraction (XRD). All fly ash samples were collected, tested for up to three periods of milling using a Bruker D8 Discover Diffractometer machine with Cu X-rays and Ni filter at a step scanning mode. The machine software was set to report in 2θ units from 5 to 60 degrees. The analysis of the intensity peaks provided the composition of the mineral phases that were present in the dry samples. Fig 4.7 to Fig 4.9 demonstrate the comparative study of mineral composition for magnetically separated and non-magnetic fly ash and also enabled to evaluate the effect of milling time on the mineral composition. In Fig 4.7, black line represents reference (unmilled) Oak Creek (OC Ref) fly ash with higher content of quartz followed by mulite, gypsum and hematite. After milling and magnetic separation, two products were obtained, magnetic and non-magnetic. Based on the milling time, these components are represented as OCxM

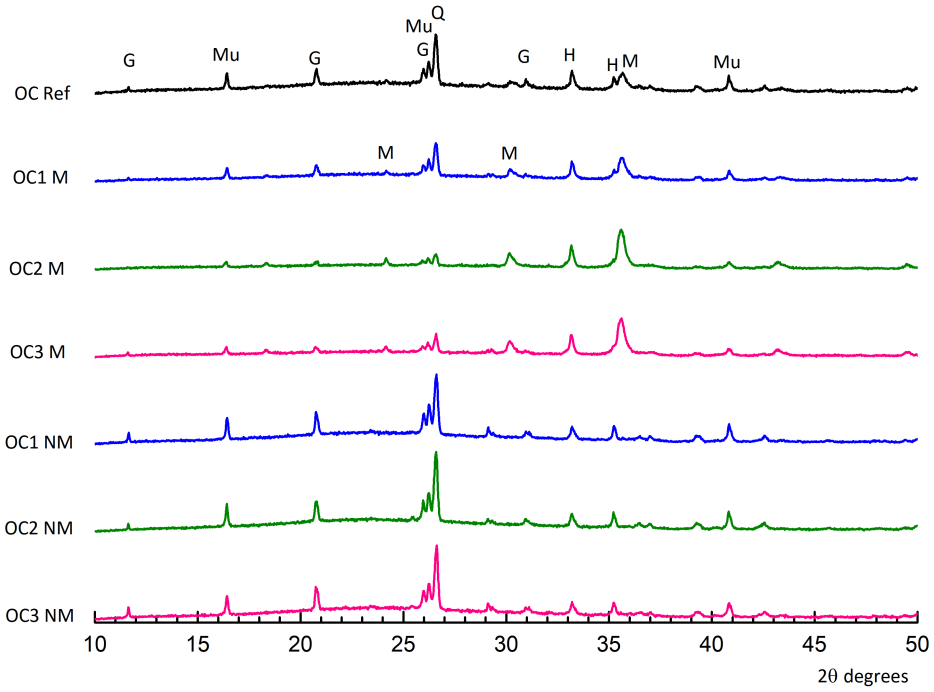


Figure 4.7: Comparative mineral composition (XRD) of magnetic and non magnetic Class F Oak Creek fly ash milled for one hour, two hours and three hours
(Note: G= Gypsum, Mu= Mulite, Q=Quartz, H= Hematite, M= Magnetite, C= Calcite)

(OC=Oak creek fly ash, x= milling time, 1,2,3 hours, and M= magnetic) and OCxNM (NM= non-magnetic). The magnetic fly ash has a strong presence of a higher volumes of magnetite, whereas non-magnetic ash is characterized by amorphous phase and higher peaks of quartz and gypsum. The increase in milling time have resulted in considerable increase in the peak intensities for magnetite and, to lesser extent, hematite in magnetic fly ash whereas in non magnetic fly ash the intensities of identical phases were found to be considerably constant irrespective of the milling time.

The Fig 4.8 demonstrates that Class F LG14 fly ash has a similar mineral composition as Class F Oak Creek fly ash. The reference LG14 (LG Ref) is represented by black line and products milled for 1 hour, 2 hours and 3 hours milled are represented in blue, green, and pink, respectively. The magnetic and non magnetic milled products can be easily distinguished with higher peak intensities of magnetite, hematite, and traces of quartz,

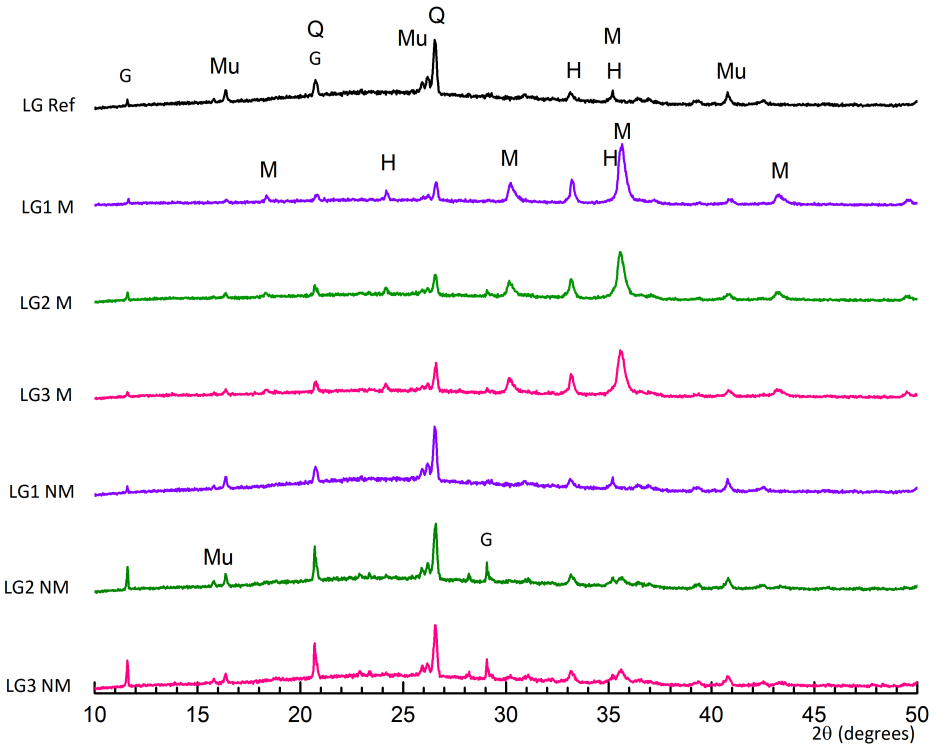


Figure 4.8: Comparative mineral composition (XRD) of magnetic and non magnetic Class F LG14 fly ash milled for one hour, two hours and three hours
(Note: G= Gypsum, Mu= Mulite, Q=Quartz, H= Hematite, M= Magnetite, C= Calcite)

in magnetically beneficiated product and higher peak intensities of gypsum and presence of amorphous phase in non-magnetic fly ash. With the increase in milling time up to 2 hours, a considerable increase in intensities is observed in non-magnetic fly ash than in non-magnetic fly ash. The Fig 4.9 reports the mineral composition transformations for Class F Prairie State fly ash. The reference Prairie State fly ash product has a similar mineral composition as other two fly ash materials used in this study. However, calcite formation is observed after milling and separation in non-magnetic products. Quartz is observed in all the milled products based on Prairie State ash including magnetic ash, which was not the case for other fly ash materials.

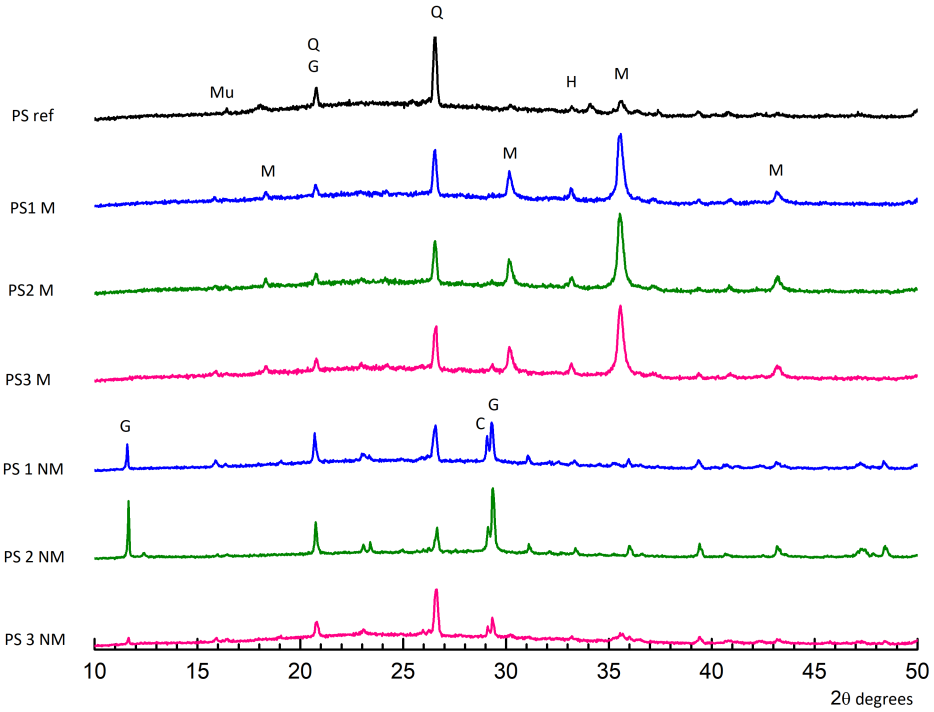


Figure 4.9: Comparative mineral composition (XRD) of magnetic and non magnetic Class F Prairie state fly ash milled for one hour, two hours and three hours
(Note: G= Gypsum, Mu= Mulite, Q=Quartz, H= Hematite, M= Magnetite, C= Calcite)

4.2 Lunar Regolith

Simulated LR sourced from Uplift Aerospace was received in a number of batches, the first considered the reference (control) sample named LR1. The subsequent batch (LR2) included sand coarse (LR2 C1 to C6) and fine (LR2 F1 to F6) powder samples. Initial visual observation of these regolith simulants detected a noticeable variation in particle shape and size, suggesting inhomogeneous distribution of the constituent mineral phases. A regiment of sieve-sorting, followed by chemical material identification, milling of various sorted materials, micro- and nano-particle size distribution analysis, and in-depth material characterization for these subsequently separated batches were carried out over the course of the investigation. Following these separation and characterization processes, these processed materials were mixed in various iterations and combinations within controlled cementitious

cement matrices, then subjected to further cement-specific experimental characterization techniques, including 'heat of hydration' (HOH), flow test, as well as short- and long-term compressive strength testing.

4.2.1 Particle size distribution

The LR samples as received had varying particles sizes, hence the characterization of these samples was first step to determine the particles size distribution using sieve analysis test. The sieve analysis test was performed using ELE International Rotary sifter Shaker. The samples were sieved through eight sieves with starting size of sieve from 4.76 mm to 0.075 mm. Each sample weighed 1000 g and was sieved for 8 minutes. After sieving, the quantity of sample retained on each sieve was weighed. Later sieve analysis data was used to calculate the percentage passing and percentage retaining. The particle size distribution curves were obtained from the data collected after sieving.

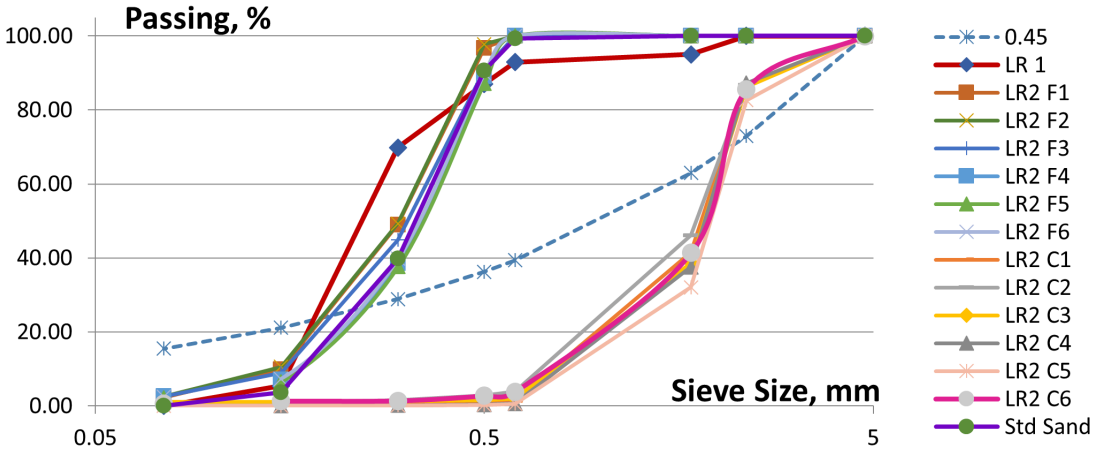


Figure 4.10: Sieve analysis curve for LR samples

The Fig 4.10 gives the particle size distribution for the LR sample received in batch one and, 12 LR (fine and coarse) samples received in batch two, as compared toand standard sand. The sieve analysis curve for LR coarse sand samples (LR2 C1, LR2 C2, LR2 C3, LR2 C4, and LR2 C5) almost coincides, similarly, the curves for fine powder LR samples

(LR2 F1, LR2 F2, LR2 F3, LR2 F4, and LR2 F5) aligns with each other. In addition to this, LR1 curve can be recognized distinctly. The distinct curves for fine and coarse samples are observed. Further, 0.45 power curve was plotted to optimize the aggregates grading for compositions based on LR sand.

4.2.2 Mineral composition

In order to characterize the LR simulant, it is highly desirable to have the exact mineral-composition to investigate the compatibility and potential reactivity with cement matrix. The general XRD and XRF report for the LR simulant was provided by the manufacturers, and the first LR simulant received was prepared by combining the particles with varying size and compositions. The second load of simulant was composed of fine grey powders and coarse sand was a blend of fine and coarse particles. Therefore, to understand the mineralogical composition of fine and coarse LR simulant, X-Ray diffraction was performed using Bruker D8 Discover Diffractometer machine with Cu X-rays and Ni filter. This is the same unit which was used for XRD characterization of all the powder materials used in this research. The same procedure was followed, and the machine software was set to report the intensity vs the angles of diffraction of 5-60 degrees using 2θ units.

4.2.3 Effect of milling

The fine and coarse regolith samples were milled using SWECO vibratory mill. The LR2 fine powder was milled to produce a fine material which can be used as cement replacement, and coarse LR2 was milled to produce a standard-sized sand and aggregate blend corresponding to 0.45 power curve. The milling time varied depending on both the coarseness needed to be produced and the particle size of the raw materials. The LR fine powder was milled for

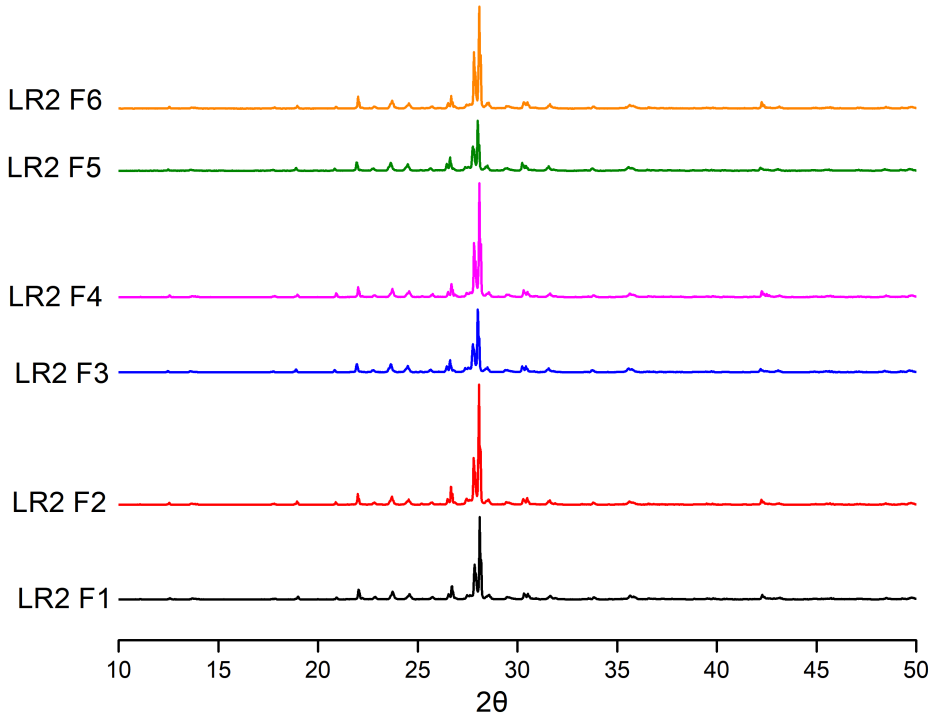


Figure 4.11: The X-ray diffraction Characteristics of fine LR samples

2 hours and 4 hours, whereas LR coarse sand was milled for 20 mins. The dry milling was carried out in the chamber, with 3,500 g of sample and 35,000 g of steel grinding media. The fine powder samples were milled to achieve the particle passing 200 μm sieve. The samples after milling were finer and fine samples tend to agglomerate during dry sieving complicationg the sieve analysis. Thus, Malvern Microsizer 3000 was used to measure the particle size. Table 4.3 demonstrates that due to milling the particle size was reduced to 2.93 to 32 μm - range which is finer (similar) to the size of portland cement and fly ash used in this research.

Further, coarse LR samples were milled for 20 mins to achieve the standard size sand and 0.45 power curve product as defined in Fig 4.10. These milled products were then used to cast mortar samples tested for compression. The results of compressive strength test are

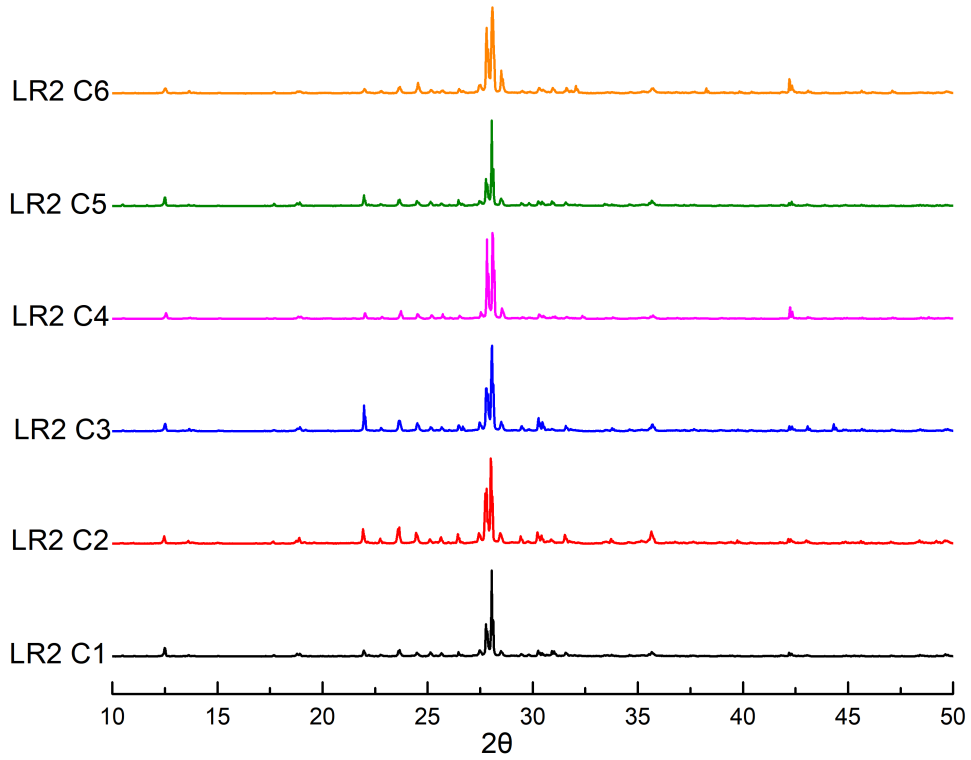


Figure 4.12: The X-ray diffraction for coarse LR samples

given in Section 4.5.

4.3 Rheological properties of cementitious inks

Through rheological testing, the characteristics of particulate suspensions e.g. cement paste, such as workability and flow can be determined, and insights gained as to how the paste's viscosity changes with time, and the effect on the overall fluid flow behavior [37]. For MRCI, rheological parameters such as yield stress and plastic viscosity can be modified by applying an external magnetic field, thus introducing a new set of properties described as magnetorheological response. The value of magnetorheological fluids (MRF) is realized when a magnetic field is applied; micron-sized ferrous particles suspended in the fluid align parallel to the flux path, creating the particle 'chains' as demonstrated in Fig. 4.13. Initially, the

Table 4.3: Reduction in particle size after milling of LR fine samples

LR2 Fine	Particle size, μm		
	D10	D50	D90
Milled for 2hrs	3.44	18.80	46.50
Milled for 4hrs	2.93	11.30	32.00



Figure 4.13: Response of magnetorheological fluid:(a) without magnetic field, fly ash and magnetite particles are randomly distributed and (b) ferrous particles aligning along the flux path under magnetic field, after [3]

ferrous particles are randomly distributed as in Fig. 4.13, but upon the application of a magnetic field, these ferrous particles begin to align along the flux path Fig.4.13. These particle chains restrict fluid movement within the cement matrix, creating a yield stress developed in the fluid on demand, and resulting in a considerable change in the rheological response [3, 58, 41, 59, 60, 61]. The degree of this shift is related to the strength of the magnetic field and may occur in a matter of milliseconds. When subjected to a magnetic field, the fluid can greatly increase its apparent viscosity to become a viscoelastic solid exhibiting non-Newtonian behavior, e.g., Herschel-Bulkley response [41]. Initially, in the fundamental models of rheology, such as the Bingham model was used to characterize the MRF [62]. Later, many researchers confirmed that Bingham's plastic model to be more appropriate for describing the MRF response [59, 63, 60, 61]. Whereas the Bingham model demonstrates a flow curve as shear stress against shear rate, the Casson model plots the slope of shear stress as a function of shear rate. Unlike these two models, the Herschel-Bulkley model is based

on three parameters which serve to explain the flow curve and yield stress of visco-plastic fluids, and is more commonly used in these cases [41, 64]. The fluid greatly increases its apparent viscosity to become viscoelastic solid when subjected to magnetic field exhibiting non-Newtonian behavior (Herschel-Bulkley model) [41]. The magnetic field intensity plays an important role in controlling the yield stress, viscosity, and other rheological characteristics of MRF. Although MRF are not common in civil engineering applications, such products have been used in variety of areas, such as shock absorbers, automotive clutches, vibration dampers and seismic vibration control, drilling fluids, gun recoil systems, body armor, and also for cancer treatment, prosthetic knee dampers, and other advanced materials [43, 65, 66, 44, 40]. The concept of MRF based cement has been proposed [42] but no real application in 3D printing have come to fruition. Based on the principle of MRF, the MRCI with active control is introduced. This MRCI relies on the incorporation of nano materials and ferromagnetic components into the cementitious material that is tuned for a desired response under an external magnetic field, changing the behavior of the material from liquid to solid-like. In addition to iron particles present in cement and fly ash, magnetic powders such as iron oxide powders often used as pigments can be added to cement paste to enhance the response under the external magnetic field. The quantity of magnetic particles and strength of applied magnetic field play an important role in controlling the rheological properties of MRF [42]. Therefore, rheological properties of cement paste can be altered as desired by adjusting these parameters. Due to the application of a static magnetic field during hardening, more C-S-H was fount to be produced, with denser morphology and reduced porosity [67]. Significant improvement in mechanical performance was observed in the hydration process due to the applied magnetic field.

This research hypothesized that the magnetic field may also have a significant impact

on important properties of MRCI such as compressive strength and fracture mechanics, but these factors have not yet been investigated.

4.3.1 Testing equipment and geometry

Rheological measurements are empirical and can vary largely with minor variations in the execution of the experiments. Thus, it is important to use a proper apparatus and geometry for the rheological measurements. For this research, Discovery HR-1 Dynamic Shear Rheometer (DSR), from TA instruments was used. Initially, parallel plate geometry with a diameter of 25 mm was used in the preliminary research stage, but test results were not consistent for stiff pastes due to slippage. Hence, after intensive research, coaxial cylinder geometry with vane rotor was used. The use of coaxial cylinder geometry for measuring rheological response was proposed back in 1941, but successful implementation was demonstrated in 1980s [37]. Generally, the rheological properties of the cement paste, mortar and concrete samples were measured in terms of fundamental physical quantities; yield stress and plastic viscosity. The vane geometry attached to the rheometer is suspended in the coaxial cylinder containing fresh sample such as (cementitious paste with mix proportions specified in Section 4.3.4. The blades of the vane geometry help to avoid any possible slippage and enable measuring accurate values of stress and viscosity at specified shear rate. This setup was used for rheological measurements, but for magnetorheological measurements, there was a need to attach an electromagnet to vane geometry. Some manufacturers of rheometers can provide a magnet only for plate geometries. Hence, an electromagnet to be used for all the magnetorheological measurements was desired. This magnet was further improvised using steel plate attachments to avoid the loss of magnetic field and to achieve a uniform magnetic field at the center.

4.3.2 Design and evaluation of electromagnet

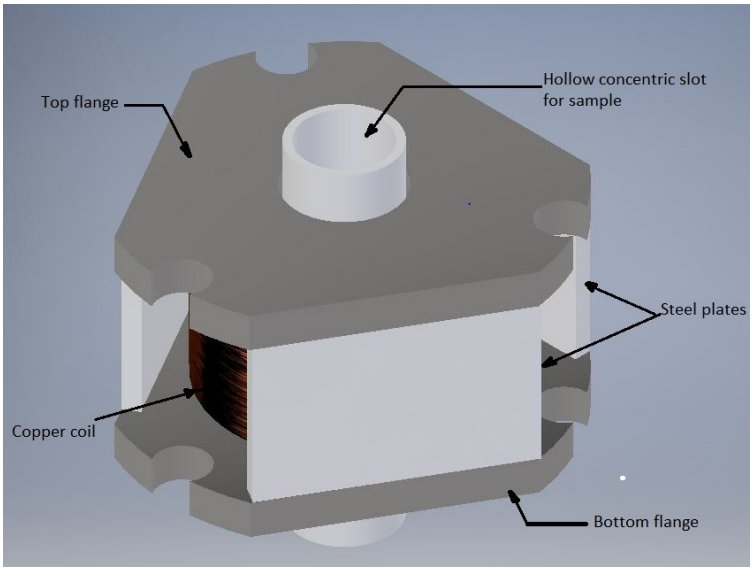


Figure 4.14: The schematics for electromagnet

The Fig. 4.14 presents the schematic design of the electromagnet. The electromagnet contained a hollow core concentric solenoid wrapped with 1000 turns of copper wire between the top and bottom flanges of the electromagnet. The hollow core concentric arrangement was intended to place the coaxial cylinder containing a fresh sample. The top and bottom flanges are triangular in shape with three sides to fit the rheometer. Initially, these sides were open, later the top and bottom flanges were connected with three plates as demonstrated by Fig. 4.14, forming a closed circuit for the magnetic field to pass over an outer portion providing the uniform magnetic field at 0.1 T at the center of the core, when current of 5 A is applied to the solenoid. Cooling copper pipe connected to theromstat cooler was further wrapped over the coil to provide the desired testing temperature.

4.3.3 Sample preparation and testing protocols

The composites were mixed according to ASTM C305 "Standard Practice for Mechanical mixing of Hydraulic Cement Pastes and Mortars of Plastic Consistency" using a hand-held

6-speed Mosaic-brand mixer with a helical blade. All mixing was performed using the third speed setting at 650-850 rpm as recommended by reference literature [68, 69]. The rheological characteristics of cementitious ink were determined using Dynamic Shear Rheometer (DSR from TA instruments) with vane geometry.

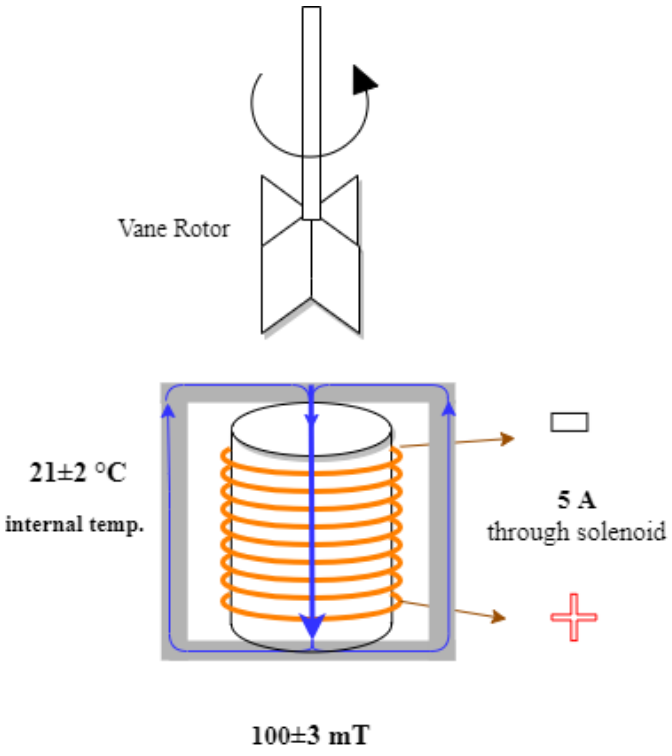
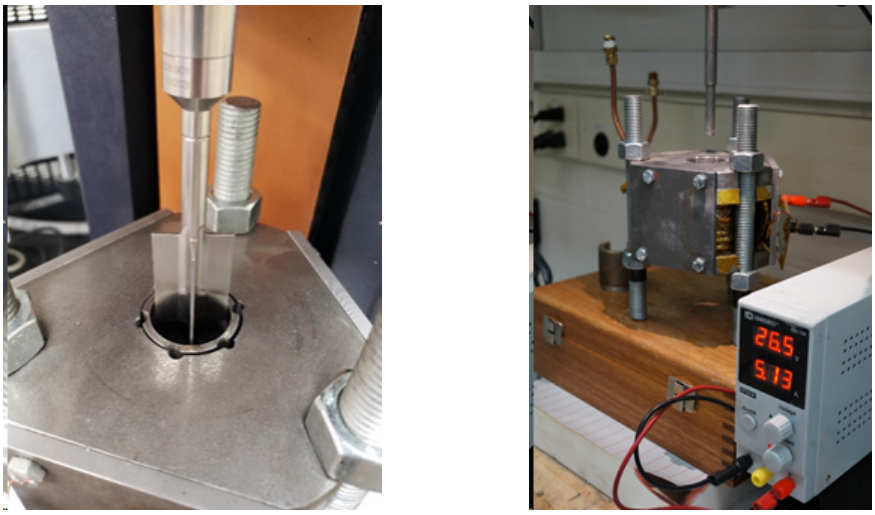


Figure 4.15: The schematics of the experimental setup with electromagnet including the side plates and magnetic field marked by the arrows.

After two minutes of mixing, the cement paste was placed into a steel cylindrical container for rheological testing. The rheological experiment is described by a testing protocol (Fig.4.17), where, after preconditioning, the sample was subjected to three sets of the ramp up and ramp down tests. Preconditioning helps to bring the sample at a stable point before the rheological measurements. The same compositions (freshly mixed to duplicate) were then tested for the investigation of rheological response under a constant magnetic field of 0.1 T.

The rheological tests were conducted at a room temperature, but a temperature increase



(a) (b)

Figure 4.16: Experimental setup for magnetorheological test: Pictures of (a) vane rotor and steel cylinder inside the solenoid; (b) the electromagnet with side steel plates and power supply

of up to 3.9°C was observed on account of heating of the electromagnet, so the target temperature of 21°C was maintained using a recirculating chiller manufactured by FTS. The chiller attached to the electromagnet maintained an average temperature of 21±2°C inside the ink sample. The magnetic setup consists of an electromagnet (Fig.4.16a) with steel plates mounted on the outside to concentrate the magnetic field inside the solenoid. The electromagnet was powered with a 20 V direct current power supply and set to 5 amperes for the duration of the rheological test. For selected settings, the electromagnet supplied a constant magnetic field of 0.10 T to the ink sample at the center. Using the F.W. Bell 5180 gaussmeter with an axial probe, the magnetic flux density was measured radially along the axial direction of the electromagnet with a deviation of 0.±3 μT inside the core. The axis of the cylindrical container and electromagnet were coaxially aligned to produce the maximum magnetic field at the center where the mix composition was placed as illustrated in Fig. 4.15 A steel cylinder was used for magnetorheological investigation to facilitate the transfer of uniform magnetic field throughout the ink sample. The cylindrical

container geometry was used in conjunction with a vane rotor, as this setup produced an accurate rheological response for a range of cement paste compositions. Additionally, the corresponding temperature, current and voltage were recorded during the soak time and at the end of last ramp. The entirety of the rheological test was time-monitored to enforce the consistency amongst all the experiments. These trials were repeated twice, but only one rheology curve is reported per trial, as each individual curve relies on a number of independent variables and averaging these results would skew the meaningfulness of the graphs. A timeline of the test protocol is shown in Fig. 4.17

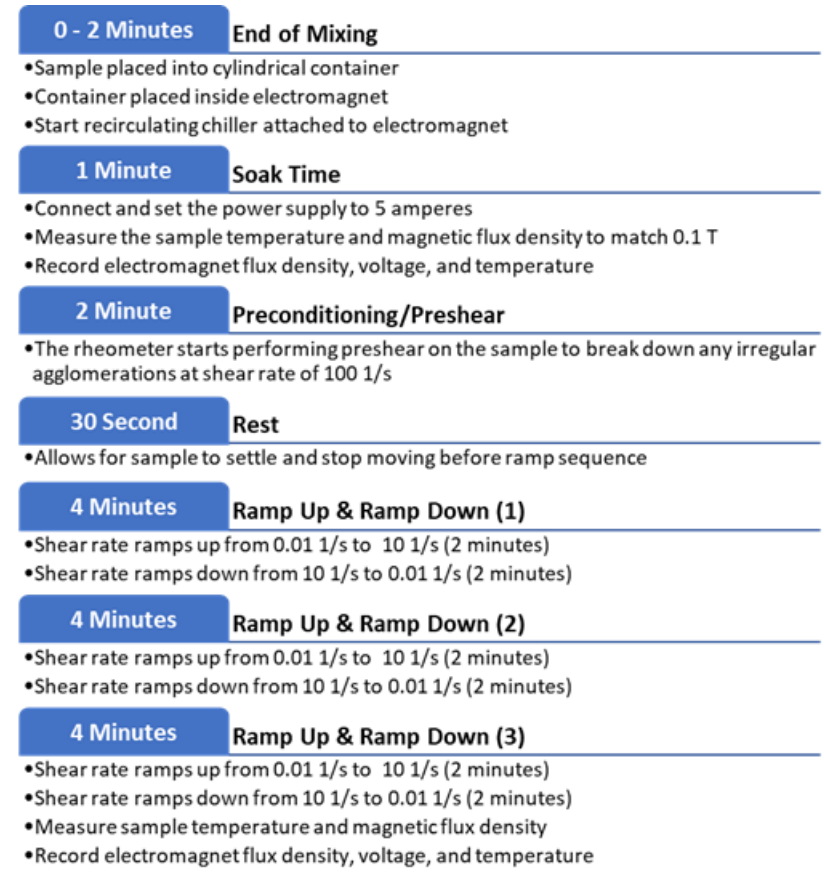


Figure 4.17: The test protocol for magnetorheological investigation

4.3.4 Experimental matrix for rheological and magnetorheological measurements

The rheological study of the compositions were carried out in three stages based on the ferromagnetic material used. In stage one, reference compositions with portland cement and fly ash were evaluated. These systems were further doped with nano-silica, nano-alumina and magnetite powder. In stage two, reference portland system was doped with different dosages of cobalt, to study the effect of cobalt on magnetorheological response. In stage three, reference portland cement systems with 10% replacement of milled fly ash (magnetic and non-magnetic) were evaluated.

Stage 1: Portland cement and fly ash systems doped with nano-particles and magnetite powder

The experimental matrix for Stage 1 compositions is reported in Table. 4.4. First reference mix contained only Type I portland cement with superplasticizer (R_1); and second reference mix, R_2 contained 50% portland cement and 50% Class F fly ash. These two reference mixes then were compared with compositions incorporated with two types of nano-materials such as nano-silica (R_1NS, R_2NS) and nano-alumina (R_1NA, R_2NA) to study the effects of nano-particles on the properties of cementitious pastes.

The proportions and dosage of chemical admixtures for MRCI were established by previous research [50, 52, 53, 55], and the appropriate measure of mixing water was added to these batches to compensate for the volume of water from chemical admixtures and NP dispersions. These six unique mix compositions were further compared with corresponding mixtures doped with magnetite powder used upto 5% of cement replacement by weight (compositions R_1M, R_2M, R_1NSM, R_1NAM, R_2NSM, R_2NAM). The magnetite powder is

Table 4.4: The expanded test program for Stage 1: portland cement and fly ash systems doped with nano-particles and magnetite powder

Mix Id	Mix Constituents	Ink Composition (%)					
		Portland Cement	Fly ash	Nanomaterials		Magnetite	Superplasticizer*
				nano-silica	nano-alumina		
R_1	PC+SP	100	-	-	-	-	0.15
R_2	PC+FA+SP	50	50				0.15
R_1NS	PC+SP+NS	100		0.25			0.15
R_1NA	PC+SP+NA	100			0.25		0.05
R_2NS	PC+FA+SP+NS	50	50	0.25			0.15
R_2NA	PC+FA+SP+NA	50	50		0.25		0.05
R_1M	PC+SP+M	95	-	-	-	5	0.15
R_2M	PC+FA+SP+M	50	45			5	0.15
R_1NSM	PC+SP+NS+M	95		0.25		5	0.15
R_1NAM	PC+SP+NA+M	95			0.25	5	0.05
R_2NSM	PC+FA+SP+NS+M	50	45	0.25		5	0.15
R_2NAM	PC+FA+SP+NA+M	50	45		0.25	5	0.05

[Notation:PC= Portland Cement, FA= Fly Ash, SP= Superplasticizer, NS= Nanosilica, NA= Nanoalumina, MP= Magnetite Powder (also M is used for mix ID) R_1= compositions based on superplasticized portland cement pastes, R_2= compositions based on superplasticized cement - fly ash systems, * as percentage by mass of the binder]

commonly used in concrete as pigment at a dosage of 5% cement replacement by mass which was also confirmed by previous work [42, 70]. Overall, 12 mix compositions were tested using a standard rheological procedure without magnetic field and were compared to the response of the same (and freshly mixed) pastes under magnetic field. The pre-dispersed nano-Al_2O_3 fibers and nano SiO_2 particles were also used in a form of dispersion. The concrete ink compositions were produced at a constant water to cementitious material ratio of 0.3 and nano-materials (SiO_2 and Al_2O_3) were used at the dosage of 0.25 by weight of cementitious materials. Therefore, two superplasticized reference compositions, based on portland cement and fly ash used (at 50% replacement by weight) were compared with compositions containing nano-particles. The cement inks with magnetite powder of black iron oxide pigment (MP) at 5% (by the weight of composition) were compared to non-MP compositions.

Stage 2: Portland cement systems with cobalt powder

The experimental matrix for the Stage 2 compositions is listed in Table 4.5. The cobalt is the ferromagnetic material used in these compositions to induce and potentially, amplify the magnetorheological response. The cobalt dosages were varied from 0.01 to 1% to determine the effects of cobalt on rheological and magnetorheological response. Other important factor that was investigated in this study, is the compatibility of cobalt with the portland cement matrix. In addition to reference superplasticized portland cement system (R_1) cementitious inks with, 0.01%, 0.1% and 1% of cobalt powder were tested and compared. The water to cement ratio of 0.3 and dosage of superplasticizer of 0.25 by weight of cementitious material was kept constant similarly to Stage 1 research. In the Stage 2 compositions, nano-materials were not used because cobalt was expected to have a complex behavior required investigation before any further inclusions. Alike Stage 1 compositions, each mix composition was tested twice using standard rheological procedure without and with magnetic field.

Table 4.5: The experimental matrix for Stage 2: portland cement systems doped with cobalt powder

Mix Id	Mix Constituents	Ink Composition (%)		
		Portland Cement	Cobalt	Superplasticizer*
R_1	PC+SP	100	-	0.15
R_1Co0.01	PC+Co(0.01%)+SP	99.99	0.01	0.15
R_1Co0.1	PC+Co(0.1%)+SP	99.9	0.1	0.15
R_1Co1	PC+Co(1%)+SP	99	1	0.15

[* as percentage by mass of the binder]

Stage 3: Portland cement and milled fly ash systems

In this research, an attempt was made to use a sustainable ferromagnetic material harvested by using fly ash beneficiation technique. The section 4.1.4 explains the material balance for

three types of fly ash after milling of three hours. Fig 4.3 demonstrates that Oak Creek fly ash when milled for 3 hours comparatively yield more magnetic particles than other two types of fly ash. Hence, the rheological response was studied using Oak Creek fly ash milled for 3 hours. Table 4.6 explains the mix composition for reference, magnetic and non-magnetic milled Oak Creek fly ash. The reference mix composition (R_1O) includes superplasticized portland cement system with unmilled (as received from producer) fly ash at 10% replacement of cement. Further, R_1OM and R_1ONM compositions included magnetic and non-magnetic particles, respectively of Oak Creek ash milled for 3 hours and used at 10% replacement. To evaluate the effect of superplasticizer, these three compositions were repeated without the addition of chemical admixture. Alike Stage 1 and Stage 2, the same water to cementitious ratio of 0.3 was used and all the mixes were tested for rheological response with and without magnetic field.

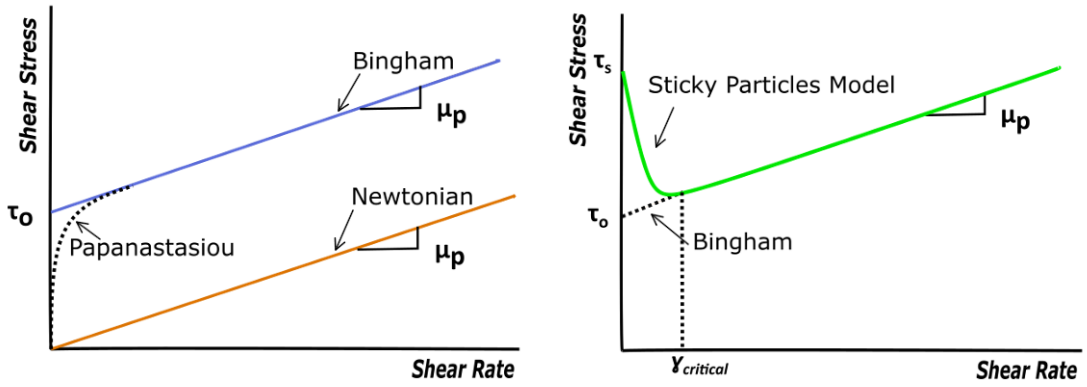
Table 4.6: The experimental matrix for Stage 3: portland cement systems with 10% 3hrs milled fly ash

Mix Id	Mix Constituents	Composition (%)				
		Portland Cement	Fly ash	Milled fly ash		Superplasticizer**
				Magnetic	Non magnetic	
R_1O	PC+FA+SP	90	10	-	-	0.15
R_1OM	PC+OM+SP	90	-	10	-	0.15
R_1ONM	PC+ONM+SP	90	-	-	10	0.05
R_1O*	PC+FA	90	10	-	-	-
R_1OM*	PC+OM	90	-	10	-	-
R_1ONM*	PC+ONM	90	-	-	10	-

[** as percentage by mass of the binder]

4.3.5 Rheological and magnetorheological response of MRCI

The rheological response of superplasticized cement systems, especially when nano-particles of $SiO_(2)$ were used, are characterized by Bingham models. The refined Bingham-Papanastasiou



(a) (b)

Figure 4.18: The models governing the rheological response of MRCI: (a) ramp up; (b) ramp down

[71, 72] model can better describe the behavior of superplasticized nanoparticle-cement paste on loading, but also to represent the stiffening at shear rates approaching zero, upon unloading. The ramp down (RD) response for binders with nano-particles can be described by "Sticky Particles Model," proposed by Sobolev. Fig. 4.18 [73] provides the summary of rheological models governing the performance of MRCI for ramp up and ramp down response. Ramp up model based on Bingham-Papanastasiou is given by the Equation (1), where τ is the shear stress at the corresponding values of m and μ_p. As the value of m increases, the shape of the transition zone becomes sharper:

$$\tau = \left(\mu_p + \tau_0 \frac{[1-e^{-m\dot{\gamma}}]}{\dot{\gamma}}\right)\dot{\gamma} \qquad (1)$$

Here, μ_p is apparent plastic viscosity, τ_o is yield stress at shear rate $\dot{\gamma}$, and m is a parameter related to the transition between the solid-like and fluid systems. The first term of the model describes the response of the model at larger values of shearing rates over $\dot{\gamma}_{critical}$, and the second portion of the equation is used to model the curvature characteristic for the solid-like response. When the transition parameter m is equal to zero, this equation corresponds to the Bingham or Newtonian model. At shearing rates approaching zero, Bingham-Papanastasiou relationship is a more accurate equation for characterization of

suspensions commonly described by the Bingham model [72]. Furthermore, the "inverted" Papanastasiou equation can be modified to describe a "Sticky Particles Model," as follows:

$$\tau = \left(\mu_p + (\tau_0 - \tau_s)\frac{[1-e^{-m\dot{\gamma}}]}{\dot{\gamma}}\right)\dot{\gamma} + \tau_s \qquad (2)$$

Here, the Sticky Particles Model (SPM) includes a third parameter τ_s which is the stiffening stress, and the rest of parameters are as defined for the Equation 1. For the range of responses observed for MCRI, the transition parameter m can be assumed to be from 1 to 4. Based on Equation 2, the ramp down response for the ink systems of portland cement and portland cement with fly ash doped with nano materials and magnetite powder can accurately represent the built-up responses of the system either due to presence of nanomaterials or magnetic field. When τ_s parameter is equal to zero, the SPM converts to the Bingham-Papanastasiou equation. The values for rheological parameters such as yield stress (τ_o), stiffening stress (τ_s) and plastic viscosity (μ_p) for all 12 mixes as tested with and without magnetic field during all three rampdown runs are given in Table 4. The percentage build up for each mix under the magnetic field is calculated and reported. The mix IDs for the response of compositions with applied external magnetic field are denoted with prime (‘). For instance, at the third ramp down cycle, the compositions R_2NSM and R_2NAM have τ_o as 19 Pa and 12 Pa, respectively, τ_s as 69.6 Pa and 25.4 Pa, respectively, μ_p as 3.8 Pa · s and 3.91 Pa · s, respectively (Table 4). The response of these compositions can be modeled assuming parameter m as 2.5 and 4 respectively, to satisfy the Equations (1) and (2). In general, the rheological response differs between the Bingham-Papanastasiou model and "inverted" Papanastasiou - SPM models as demonstrated in Fig. 4.18, and such behavior is further explored and explained.

Table 4.7: Rheological constants and percentage built up for ramp down (RD) responses for stage 1 compositions

Mix Id	Mixing constituents	Ramp down 1					Ramp down 2					Ramp down 3				
		Stress, Pa		Plastic Viscosity µp , Pa.s	Build up Stress, %		Stress Pa		Plastic Viscosity µp , Pa.s	Build up Stress, %		Stress Pa		Plastic Viscosity µp , Pa.s	Build up Stress, %	
		τ_o	τ_s		τ_o	τ_s	τ_o	τ_s		τ_o	τ_s	τ_o	τ_s		τ_o	τ_s
R1	PC+SP	5.0	20.0	0.7	-8.2	8.3	5.8	17.9	1.3	11.8	173.0	4.9	15.2	1.6	125.9	483.8
R1'	PC+SP MF	4.6	21.7	0.6			6.4	48.9	1.2			11.1	88.8	1.6		
R2	PC+FA+SP	0.0	0.0	0.3	24.0	8.3	0.0	2.5	0.4	34.5	-0.4	0.0	0.0	0.4	56.6	23.5
R2'	PC+FA+SP MF	1.2	1.7	0.8			2.0	2.4	1.4			2.8	3.6	1.7		
R1NS	PC+SP+NS	115.0	**393.8**	0.0	30.4	8.5	100.0	**328.5**	1.5	61.0	28.1	91.0	277.9	1.6	73.6	35.7
R1NS'	PC+SP+NS MF	150.0	**427.2**	0.3			161.0	**421.0**	1.9			158.0	**377.2**	0.2		
R1NA	PC+SP+NA	20.0	85.2	1.7	55.0	106.5	24.0	85.5	3.5	100.0	190.4	27.0	85.2	3.5	100.0	237.3
R1NA'	PC+SP+NA MF	31.0	176.0	1.4			48.0	248.2	3.7			54.0	287.5	3.7		
R2NS	PC+FA+SP+NS	0.5	0.6	0.9	7.5	2.3	0.5	0.7	1.4	10.4	3.7	0.5	0.7	1.7	13.6	5.4
R2NS'	PC+FA+SP+NS MF	2.0	2.6	1.8			3.0	3.9	2.3			4.2	5.4	2.7		
R2NA	PC+FA+SP+NA	0.0	0.0	0.7	5.0	0.8	0.0	0.0	1.0	3.0	1.1	0.0	0.0	1.2	4.5	2.1
R2NA'	PC+FA+SP+NA MF	1.0	0.7	1.2			0.7	1.0	2.0			1.3	1.9	2.4		
R1M	PC+SP+MP	18.0	74.0	1.9	233.3	29.9	24.0	83.4	3.4	166.7	19.6	26.2	87.5	4.3	151.9	23.5
R1M'	PC+SP+MP MF	60.0	96.1	6.0			64.0	99.7	6.8			66.0	108.1	5.9		
R2M	PC+FA+SP+MP	0.0	0.4	0.5	222.2	100.6	0.3	0.3	0.6	269.5	142.6	0.4	0.4	0.6	380.0	189.6
R2M'	PC+FA+SP+MP MF	40.0	74.8	6.9			65.0	119.2	13.5			100.0	166.3	17.4		
R1NSM	PC+SP+NS+MP	190.0	**478.8**	0.8	17.4	-3.3	180.0	**371.4**	3.0	8.3	6.2	143.0	**334.7**	3.4	28.7	10.9
R1NSM'	PC+SP+NS+MP MF	223.0	**463.0**	5.0			195.0	**394.5**	5.1			184.0	**371.3**	2.1		
R1NAM	PC+SP+NA+MP	90.0	286.7	1.7	55.6	-3.9	86.0	267.5	3.9	68.6	3.7	92.0	247.8	4.0	62.0	21.5
R1NAM'	PC+SP+NA+MP MF	140.0	275.4	6.5			145.0	277.3	7.4			149.0	**301.2**	5.4		
R2NSM	PC+FA+SP+NS+MP	16.0	68.9	2.5	243.8	29.0	17.0	68.9	3.5	241.2	53.6	19.0	69.6	3.8	300.0	104.6
R2NSM'	PC+FA+SP+NS+MP MF	55.0	88.9	8.6			58.0	105.8	7.2			76.0	142.4	6.0		
R2NAM	PC+FA+SP+NA+MP	11.5	27.3	2.4	247.8	63.7	11.8	27.9	3.5	248.9	81.4	12.0	25.4	3.9	275.0	158.7
R2NAM'	PC+FA+SP+NA+MP MF	40.0	44.7	8.2			41.0	50.6	8.5			45.0	65.7	8.7		

Notation:
MF= Magnetic Field,
τ_s=stiffening stress,
μp=plastic viscosity
'= compositions under applied external electromagnetic field,
τ_o=yield stress

Table 4.8: Rheological constants and percentage built up for ramp down (RD) responses for stage 2 compositions

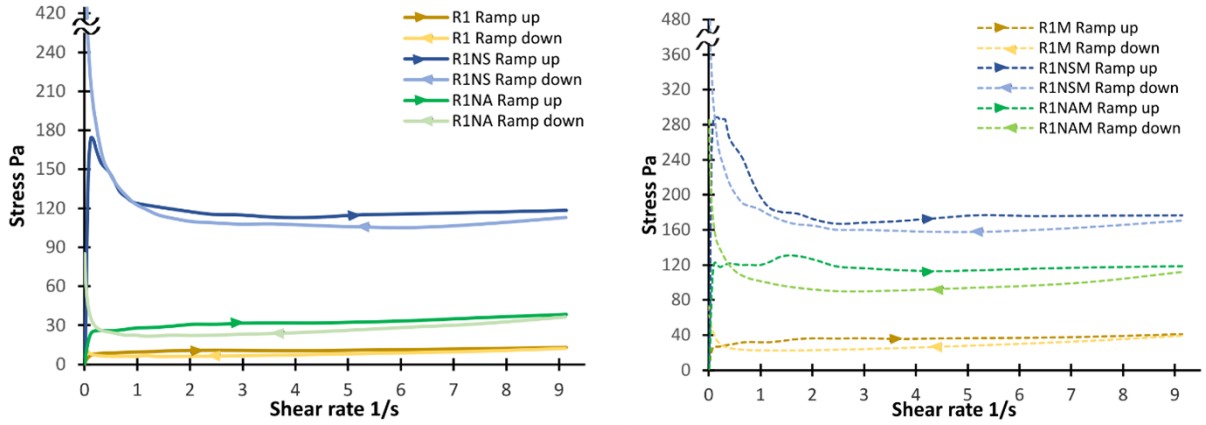
Mix Id	Mixing constituents	Ramp down 1				Ramp down 2				Ramp down 3			
		Stress, Pa		Build up Stress, %		Stress Pa		Build up Stress, %		Stress Pa		Build up Stress, %	
		τ_o	τ_s	τ_o	τ_s	τ_o	τ_s	τ_o	τ_s	τ_o	τ_s	τ_o	τ_s
R1	PC+SP	122.6	465.7	1.2	-8.3	126.5	417.5	3.7	12.5	103.6	327.6	35.1	67.3
R1'	PC+SP MF	124.1	427.1			131.2	469.7			139.9	548.0		
R1Co0.01	PC+Co(0.01%)+SP	127.3	504.7	-21.5	-2.1	131.3	400.1	-6.4	36.4	112.8	334.5	34.6	98.6
R1Co0.01'	PC+Co(0.01%)+SP MF	101.0	494.8			123.2	551.9			148.6	657.6		
R1Co0.1	PC+Co(0.1%)+SP	100.1	452.7	-30.5	-32.9	108.3	466.3	-14.6	-7.0	104.2	417.4	11.4	41.4
R1Co0.1'	PC+Co(0.1%)+SP MF	69.6	303.9			92.6	433.4			116.0	590.1		
R1Co1	PC+Co(1%)+SP	124.0	424.5	28.7	128.3	133.8	360.3	90.8	229.3	105.2	297.6	221.4	388.2
R1Co1'	PC+Co(1%)+SP MF	159.7	969.1			255.4	1186.4			338.1	1452.6		

Notation:
MF= Magnetic Field,
τ_s=stiffening stress
'= compositions under applied external electromagnetic field,
τ_o=yield stress

Table 4.9: Rheological constants and percentage built up for ramp down (RD) response of stage 3 compositions

Mix Id	Mixing constituents	Ramp down 1				Ramp down 2				Ramp down 3			
		Stress, Pa		Build up Stress, %		Stress Pa		Build up Stress, %		Stress Pa		Build up Stress, %	
		τ_o	τ_s	τ_o	τ_s	τ_o	τ_s	τ_o	τ_s	τ_o	τ_s	τ_o	τ_s
R1O	PC+FA+SP	37.0	189.3	109.2	79.1	45.2	164.8	175.3	167.1	45.3	153.6	162.5	264.7
R1O'	PC+FA+SP MF	77.4	339.1			124.5	440.1			119.0	560.2		
R1OM	PC+OM+SP	38.9	124.5	376.8	394.8	38.9	116.9	380.5	361.5	25.4	98.9	476.2	366.8
R1OM'	PC+OM+SP MF	185.5	616.0			186.9	539.5			146.5	461.7		
R1ONM	PC+ONM+SP	177.5	816.8	-6.6	7.9	150.0	701.8	37.1	41.1	120.3	596.6	85.5	77.8
R1ONM'	PC+ONM+SP MF	165.7	881.4			205.6	990.1			223.2	1060.8		
R1O*	PC+FA	104.2	104.0	28.4	33.8	88.4	96.6	36.9	30.8	86.1	92.2	33.6	31.4
R1O*'	PC+FA MF	133.8	139.1			121.0	126.4			115.1	121.2		
R1OM*	PC+OM	61.1	63.5	139.2	151.7	62.3	64.9	154.9	138.3	63.4	65.8	150.9	168.8
R1OM*'	PC+OM MF	146.1	159.8			158.8	154.6			159.1	176.9		
R1ONM*	PC+ONM	109.9	115.0	30.4	53.9	110.3	112.6	53.4	61.0	110.3	116.2	66.5	73.0
R1ONM*'	PC+ONM MF	143.3	177.0			169.1	181.2			183.6	201.2		

Notation:
MF= Magnetic Field,
τ_s=stiffening stress
'= compositions under applied external electromagnetic field,
τ_o=yield stress,
* compositions without SP



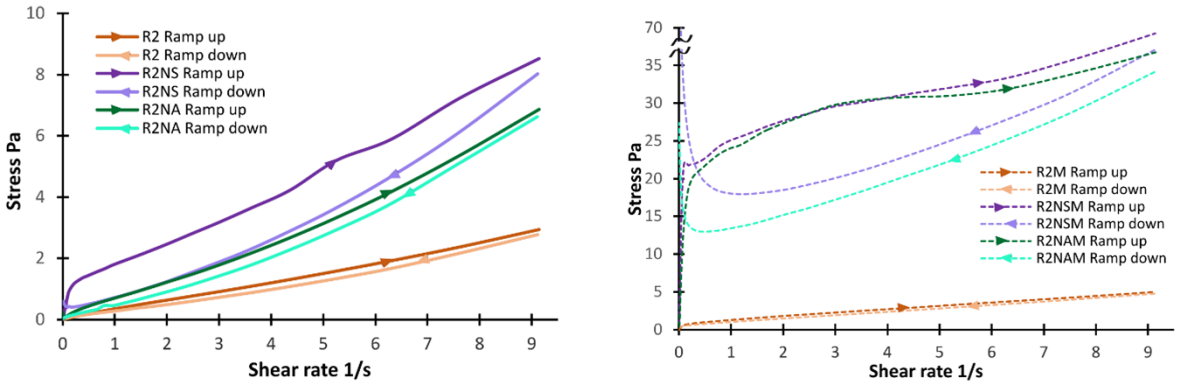
(a) (b)

Figure 4.19: The effect of nano-silica and nano-alumina fibers on rheological response of (a) superplasticized portland cement systems – R_1 series, and (b) the effect of magnetite powder – R_1M series

Effect of fly ash and nano materials on the response of MRCI inks

It is commonly agreed that fresh cement paste can be described as a Bingham fluid [37, 71, 72] which indeed was observed in the response for the reference mix R_1, Fig. 4.19a. The addition of fly ash alters the behavior of cement paste, changing its response to a Newtonian fluid. Reference mix R_2 with 50% of cement replacement by fly ash demonstrated an extreme fluidization and was characterized by constant relationship between the shear stress and shear rate as described by the classical Newtonian model, Fig. 4.20b. This transformation occurs due to the presence of fine spherical fly ash particles and, due to lower absorption capacity of fly ash powders, the redistribution of superplasticizer to portland cement grains (which can be considered as a relative increase of the dosage superplasticizer).

The Fig. 4.19a and 4.20a demonstrate the comparative increase in yield stress due to the addition of nano particles. At the same water to cementitious materials ratio, nano-silica is observed to exhibit a comparatively higher enhancement of yield values than mixes with nano-alumina. The addition of nano-silica into fly ash composition (R_2NS), shifts the response of this mix from the Newtonian back to Bingham fluid but with relatively



(a) (b)

Figure 4.20: The effect of nano-silica and nano-alumina fibers on rheological response of (a) superplasticized portland cement-fly ash pastes – R_2 series and (b) the effect of addition of magnetite powder – R_2M series

low yield values. This demonstrates that nano-silica effectively enhances the yield of fly ash-portland cement systems. The substantial differences in the response of nano-silica and nano-alumina fiber composites can be explained by the effect of surfactant used for nano-alumina fiber pre-dispersion [52]. It was observed that in ramp-down experiments, the stiffening effect corresponding to an "inverted" Papanastasiou model-SPM is appearing at very low shearing rates as nano particles facilitate the formation of gel structures. Furthermore, the investigated systems with nano particles had demonstrated a considerable thixotropy and structural rebuilding as it was observed for systems with ultrafine particles. The difference in the response of investigated systems with nano-particles was due to the formation of considerable stiffening stress exceeding the yield stress ($\tau_s >> \tau_o$), Table 4.7

Effect of magnetite powder

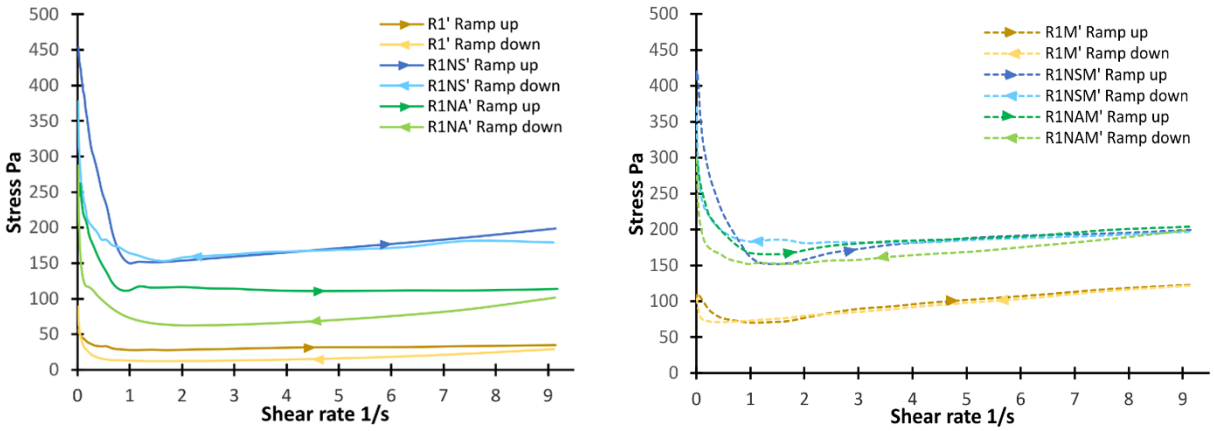
Fig. 4.19b and 4.20b report the effect of sub micron magnetite powders on reference pastes and compositions doped with nano-particles. The addition of ultrafine magnetite powders to portland cement mixes results in a considerable (3 to 4 times) increase in the yield stress, whereas compositions containing nano-silica and nano-alumina had 60% and up to 4 times

increase in the yield respectively. Although the addition of magnetite powder into fly ash / portland cement system does not constitutes a significant change but composition with nano-silica and nano-alumina fibers had a significant increase in yield stress of about 10 to 15 times altering its behavior from Newtonian to Bingham fluids (Fig.4.20b). Here, the magnetite powder enhances the effect of nano-particles, producing the compositions with considerable stiffening (τ_s at the range of 25.4 Pa to 478.8 Pa) at low shearing rates exhibiting a synergy between the nano particles and ultra-fine magnetite particles. The use of submicron-sized magnetite powder enhanced the stiffening ($\tau_s >> \tau_o$) at very low shearing rates as described by the SPM for ramp-down experiment and had a considerable thixotropic response (Fig. 4.19b, 4.20b and 4.7).

Effect of magnetic field on the response of the cementitious inks (Stage 1 compositions)

Fig 4.21 demonstrates the effect of a magnetic field on the rheological response of superplasticized reference compositions based on portland cement, whereas Fig 4.22 reports the response of fly ash-based compositions. It is observed that there has been an average increase of the yield strength by 140% upon the application of an external magnetic field of 0.1 T.

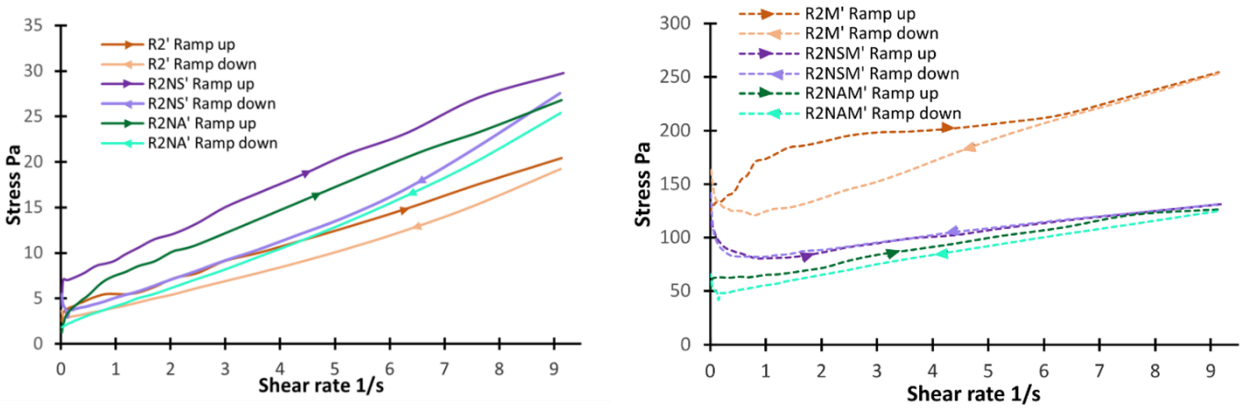
The use of magnetite powder in fly ash-based compositions enables a formation of a very effective MRCI due to the on-demand transfer from Newtonian to Bingham fluids under the magnetic fields. The use of fly ash-magnetite powder compositions with nano particles such as nanosilica and nanoalumina fibers proves to be less effective due to the formation of a non-magnetic ring surrounding the otherwise magnetic particles of fly ash and magnetite (Fig. 4.23). However, the role of nano-particles can be beneficial in the formation of self-stiffening



(a) (b)

Figure 4.21: The effect of magnetic field on rheological response of (a) superplasticized portland cement pastes doped with nano-particles R_1' series and (b) the effect of addition of magnetite powder – R_1M' series

MRCI during pumping and deposition. Here, it is important to note that a considerable stiffening is achieved at a low (approaching zero) shearing rates that occurs at the ink deposition stage. It is further observed that though mixes with portland cement (R_1, R_1NS, R_1NA, R_1M, R_1NSM, R_1NAM – R_1 series) had a higher yield stress values than compositions with fly ash (R_2, R_2NS, R_2NA, R_2M, R_2NSM, R_2NAM – R_2 series), on application of external magnetic field, the mixes with fly ash (R_2', R_2NS', R_2NA', R_2M', R_2NSM', R_2NAM'– R_2' series) demonstrated a considerable increase in the yield stress. This is because of the presence of ferrous compounds (such as magnetite) in fly ash and a magnifying effect achieved by the incorporation of magnetite powder. The combined effect of ferrous oxide compounds and external magnetic field results in effective stiffening and structure build up under these external stimuli as required for effective MRCI and 4D-printing applications. The relative percentage increase in yield stress under magnetic field for all the reported compositions is plotted in Fig. 4.24. The systems of portland cement / fly ash doped with nano-particles and magnetite possessed a significant increase in yield ranging from 275 to 522% as compared to the response without magnetic interactions. However, the same system without magnetite



(a) (b)

Figure 4.22: The effect of magnetic field on rheological response of (a) superplasticized portland cement -fly ash pastes doped with nano-particles R_2' series and (b) the effect of addition of magnetite powder – R_2M' series

powder exhibits the Newtonian response with low to zero yield. Here, the synergistic effect of

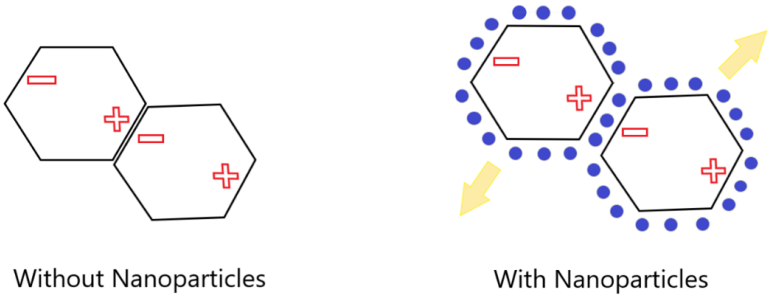


Figure 4.23: Response and structural build-up of magnetic material within the MRCI: (a) without nano-particles, magnetic particles are closely locked at poles and build a stronger chain resulting in stiffer structures and (b) nano-particles create a barrier between the magnetic poles on ferrous material thus enabling sliding

magnetite and fly ash is due to the presence of ferromagnetic phases in fly ash characterized by high Fe_2O_3 content (Table 4.1). Under the magnetic field the investigated compositions with fly ash and nano-particles had demonstrated a considerable thixotropy, Fig. 4.22a. Structural rebuilding was also observed for fly ash – magnetite powder systems but was not pronounced in complex systems when nano-particles are combined with magnetite powders, Fig. 4.22b.

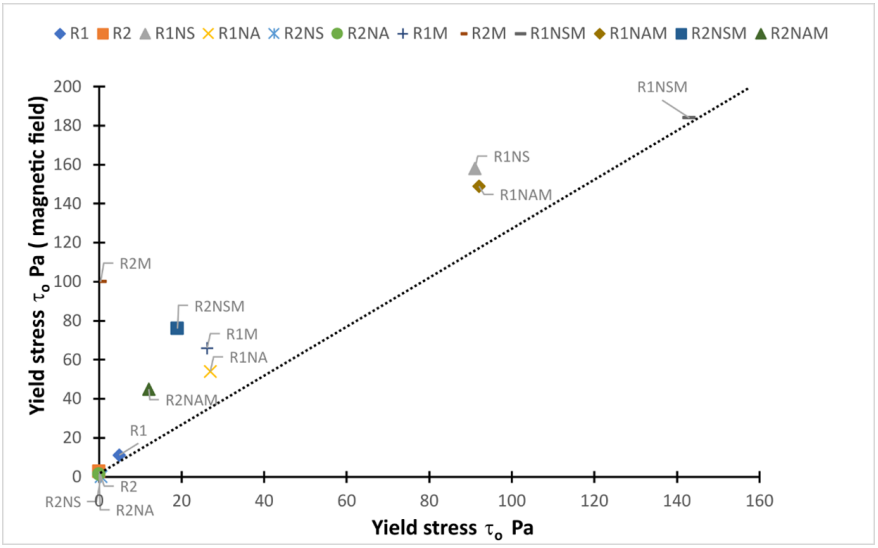


Figure 4.24: The effect of magnetic field on the yield stress (under third ramp down test) on Stage 1 compositions

Portland cement system with nano-particles and magnetite powder demonstrated a considerable yield (on the ramp-down run) even without magnetic field, but comparatively less built up is observed under the magnetic field. In Fig. 4.24, all the systems plotted above the equal stress dotted line shows a significant increase in the yield stress due to application of magnetic field, whereas systems on the dotted line or below had negligible to zero effect on the yield stress.

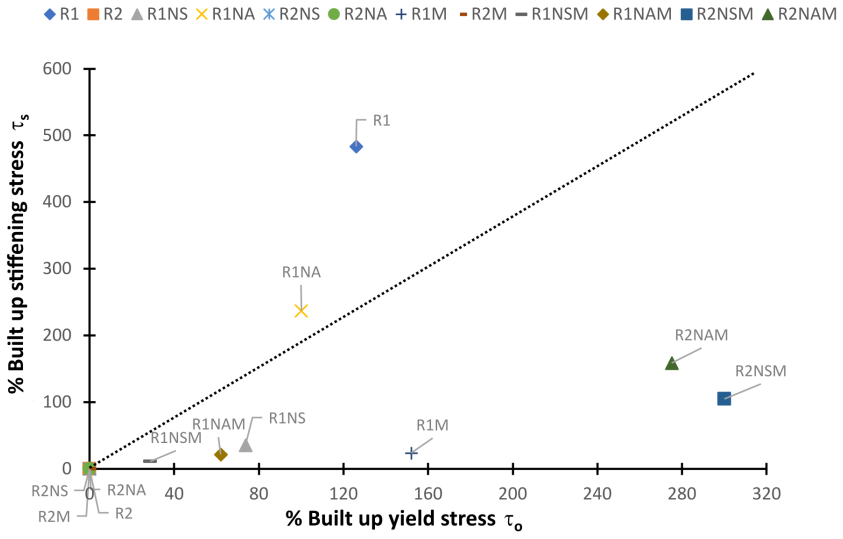
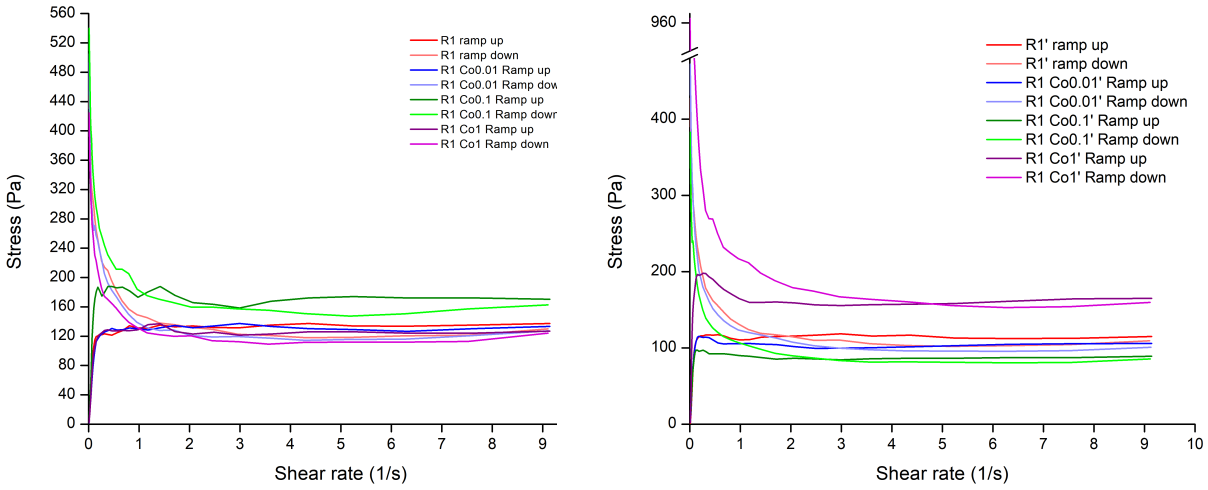


Figure 4.25: The build-up of yield and stiffening stress on Stage 1 compositions due to application of magnetic field (under third ramp down test)

Like yield stress, the stiffening stress is also considered to be a very important parameter to describe the rheological behavior of the developed inks. Though, the effect of magnetic field prominently affected the yield stress, few systems such as R_1, R_2NSM, R_2NAM demonstrated comparatively significant build-up in stiffening stress (Fig. 4.25). The dotted line in Fig. 4.25 represents the systems following a classical Bingham model, the portland cement systems such as R_1 and R_1NA which are above the dotted line follow the Bingham-Papanastasiou model upon unloading, whereas the majority of the compositions with nano-particles (R_1NSM, R_1NAM, R_1NS, R_1M, R_2NAM, R_2NSM) below the dotted line can be described by the Sticky Particles Model.

Effect of cobalt powder and magnetic field (Stage 2 compositions)

The Fig 4.26 demonstrates the effect of fine cobalt powder on the rheological response of portland cement system. This graph represents the first ramp series readings for each of the cobalt compositions. The Fig 4.26a explains that the addition of cobalt does not result in increase of yield stress and stiffening stress as compared to reference R_1 mix. However, Fig 4.26b demonstrates that, on the application of a magnetic field, cobalt powder is activated and provides a comparatively significant increase in the yield stress (τ_o) and stiffening stress (τ_s). Furthermore, as it has been observed with second and third ramp down series, the percentage build up stresses are considerably higher than observed for the first ramp down series. This is mainly because the cobalt particles start lining up forming the chains under the magnetic field and this time sensitive effect is further observed in ramp 2 and ramp 3 series. In order to further study this behavior, the mix composition was observed under the SEM. It is demonstrated that the cobalt particles are fine and highly charged so these tend to coagulate and form lumps. Therefore, cobalt powder needs to be properly dispersed in



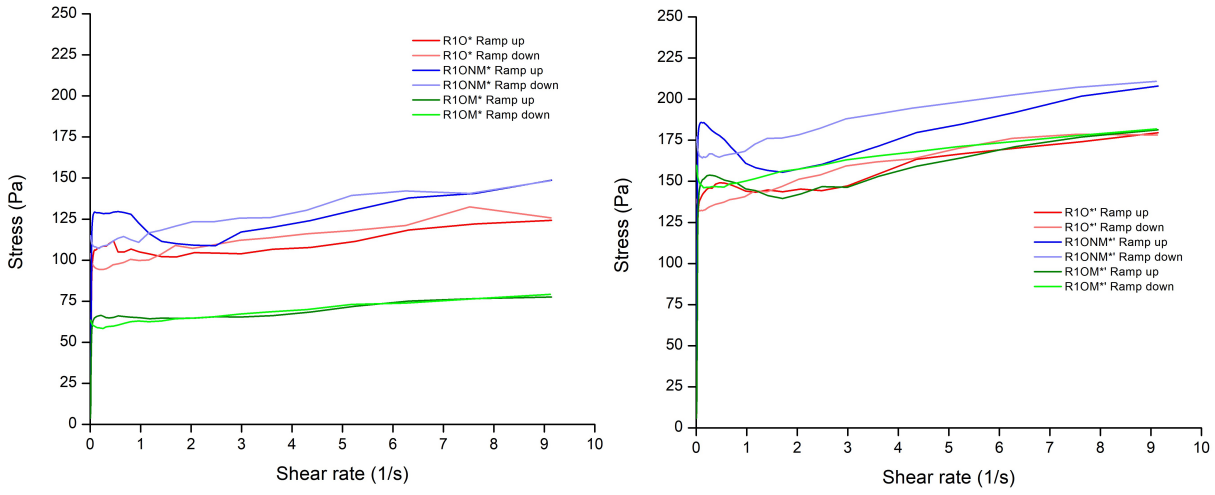
(a) (b)

Figure 4.26: The effect of cobalt on the rheological response of compositions at the first ramp series (a) no magnetic field and (b) under the magnetic field

cement systems to get more accurate and reliable results. This could also be the reason that in Fig 4.26a, in the absence of a magnetic field, cobalt particles do not align and tend to agglomerate, resulting in a comparatively lower stress values. In Table 4.8, ramp down 3, data demonstrate that cobalt powder is evenly dispersed due to the application of magnetic field resulting in an increase in the yield stress of approximately 3 times the yield stress vs. experiment without magnetic field (for compositions with 1% cobalt powder)

Effect of milled fly ash and magnetic field (Stage 3 compositions)

The Fig. 4.27 and Fig. 4.28 demonstrate the yield stresses and stiffening stresses (Ramp 1 series) for Class F Oak Creek fly ash milled for 3 hours and magnetically separated into two products: magnetic and non- magnetic. These compositions are compared with reference mix which includes portland cement and unmilled fly ash. These three compositions are repeated twice; one with superplasticizer (Fig. 4.28) another without superplasticizer (Fig. 4.27). The mix compositions with superplasticizer had demonstrated a significant increase

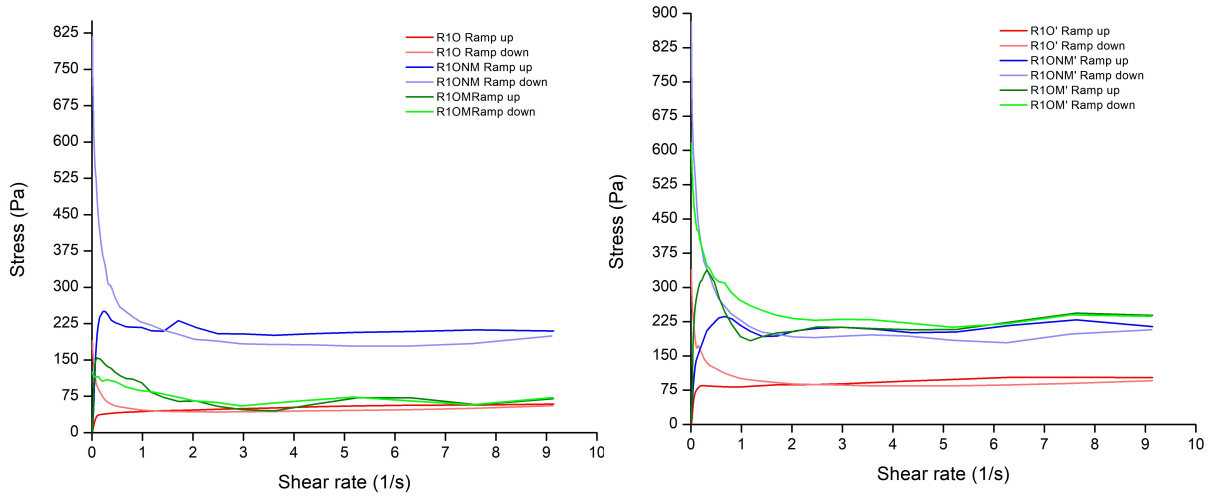


(a) (b)

Figure 4.27: The effect of milled fly ash on rheological response of the first ramp series at superplasticized cementitious ink (a) no magnetic field (b) under magnetic field

in the yield stress (60% increase) and stiffening stress (3 to 5 times increase). Thus, this effect demonstrate the role of superplasticizer in increasing the stresses (τ_o and τ_s) and contributing towards SPM behavior. It was further observed that milled fly ash systems doped with superplasticizer during the ramp down experiments demonstrates SPM response at a very low shearing rates as fine milled fly ash exhibits thixotropy and structural build up. The comparison of R_1M compositions from Stage 1 experiment with R_1OM and R_1ONM proves that R_1OM have a higher stiffening stress, and R_1ONM mix demonstrates both higher yield and stiffening stresses. The non-magnetic milled fly ash products are finer than milled magnetic products, hence, due to greater surface area, sticky and viscous mix with higher stress values were observed.

The Fig 4.27a and Fig 4.28 demonstrate that the use of non-magnetic milled products yields comparatively higher stress values than observed for magnetic and reference mixes. However, the percentage increase of stress on the application of magnetic field is considerably higher for magnetically separated fly ash compositions. It is observed that the yield stress and stiffening stress for R_1OM and R_1OM^* blends were increased up to 4.5 to 5 times after



(a) (b)

Figure 4.28: The effect of milled fly ash on the rheological response of cementitious inks at the first ramp series showing (a) no magnetic field (b) under magnetic field

the application of a magnetic field (Table 4.9). Overall, for all the compositions tested for Stage 2 and Stage 3 experiment, the application of magnetic field have resulted in an increase in yield stress and stiffening stress reported for ramp down experiment. The effect of magnetic field on yield stress is clearly visible in the Fig 4.29, with all the compositions above the dotted line demonstrating that there is an increase in yield stress due to the application of a magnetic field. There are no compositions below the dotted line which indicates that all the compositions in the Stage 2 and 3 experiment had a significant increase in the yield stress. The percentage change for build up stresses (τ_o and τ_s) are plotted in Fig 4.30. Here, R_1OM composition demonstrates a higher stiffening and higher yield stresses, whereas R_1Co1 mix had a higher stiffening stress observed in conjunction with a moderate yield stress.

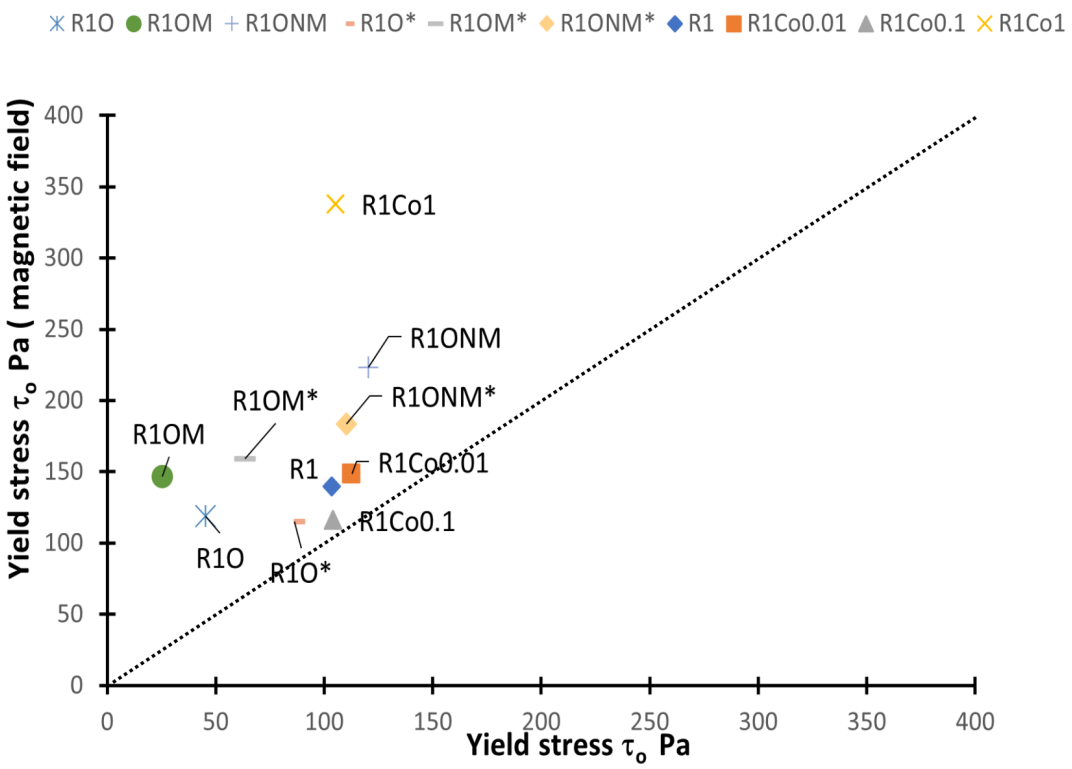


Figure 4.29: The effect of magnetic field on the yield stress (under third ramp down test) for Stage 2 and 3 compositions

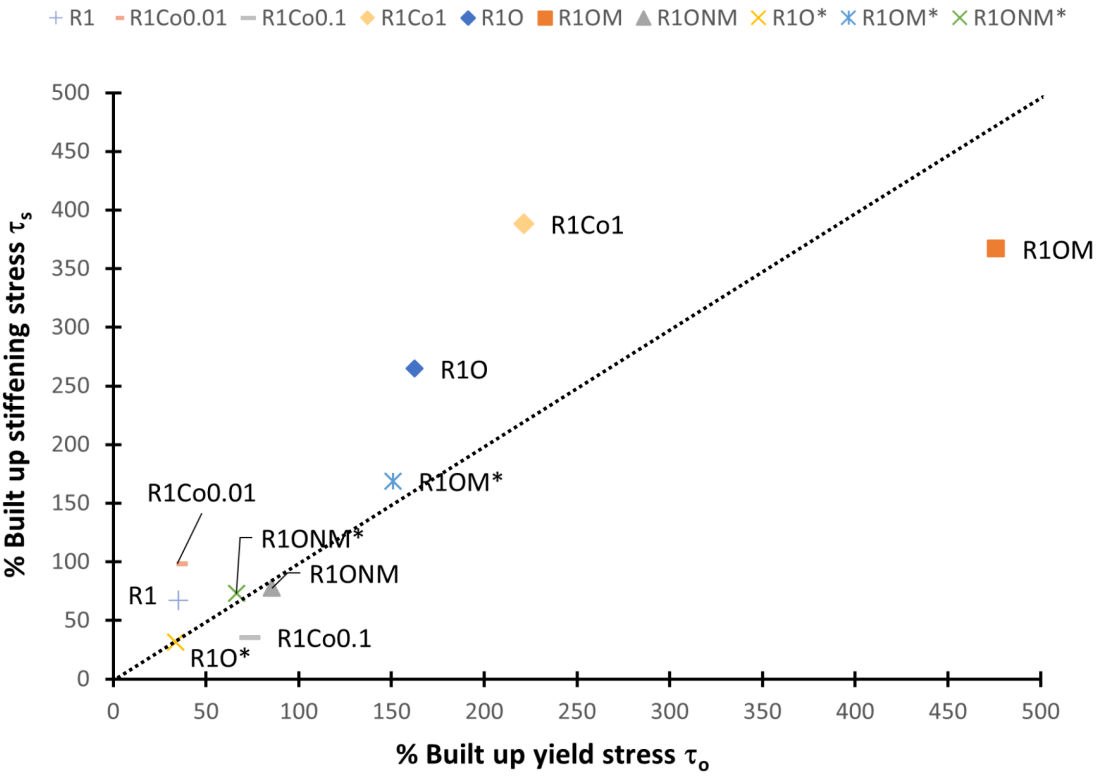


Figure 4.30: The build-up of yield and stiffening stress on Stage 2 and 3 compositions due to the application of magnetic field (under third ramp down test)

4.4 Hydration of cementitious inks

Generally, cement constitutes of chemical compounds such as Alite (C_3S), Belite (C_2S), Celite (C_3A), and Felite (C_4AF) which affect the setting and hardening process. When cement is mixed with water, exothermic reactions leading to the formation of hydration products take place with the evolution of heat. This process is termed as hydration of cement. The heat generated during this process is measured using an isothermal calorimeter and it can be used to forecast the interaction between the chemical admixtures and mineral constituents and, also, the mechanical response. There are five phases of the hydration process which help to evaluate the potential strength development of concrete as explained by Fig.4.31.

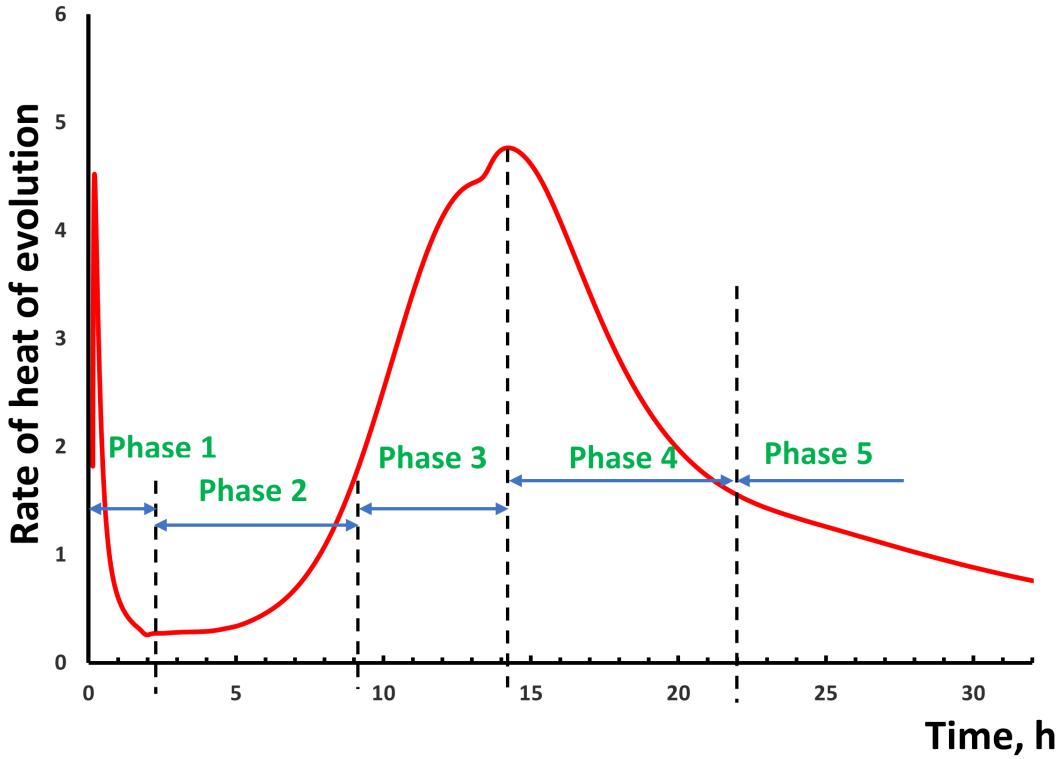


Figure 4.31: The representative heat of hydration curve indicating different phases of heat of hydration of cementitious inks

1. Phase 1: Initial Hydrolysis: In the early stages of cement dissolution, heat is released as evidenced by the first calorimetry peak.

2. Phase 2: Dormant period: In the dormant phase, the hydration products start precipitating on the surface of each cement particle. This forms a protective layer that helps in delaying the dissolution of the particle for several hours. This period is termed as dormant period.

3. Phase 3: Hydration Acceleration: This phase starts immediately after the dormant period and attains the maximum peak value for the heat of evolution. In this phase, the cement paste starts changing its semi-liquid state to a viscous fluid state.

4. Phase 4: Hydration Deceleration: After attaining maximum heat of evolution, there is a continuous decrease in the amount of heat evolved, hence the hydration process starts decelerating. Here, the cement paste starts hardening and becomes a solid with a very low strength.

5. Phase 5: Steady-state: At this phase, the rate of the heat of evolution is lowered and continuous for a longer period of time. This indicates that the formation of hydration products slows down.

Usually, all the fives phases are observed in the first 48 hours after mixing. The addition of any admixtures or supplementary cementitious materials significantly affects phase 2 and phase 3. Thus, the results of the heat of hydration for the developed ink compositions are essential for the design of MRCI as discussed in detail in the following sections.

4.4.1 Heat of hydration

The heat of hydration (HOH) experiment was carried out for all the mix compositions reported in this research. The main objective of this test for MRCI compositions was to determine the effect of magnetic field on the HOH and hydration products.

The heat of hydration tests were performed using the same compositions used for rheological tests. The samples were mixed for both tests at once using the proportion given in the Tables 4.4 to 4.7. The mixing starting time and end time were recorded. The sample of approximately 25 g was weighed into plastic bottles and placed in the calorimeter at a constant temperature of 20°C. For this test, an isothermal calorimeter (TAM Air 8-channel) from TA instruments was used. The results of heat of hydration for Stage 1, Stage 2, milled fly ash, and LR compositions are discussed below.

Stage 1 compositions

For each composition in Stage 1, two samples were kept in calorimeter, one after mixing (before running magnetorheological test) and other after the exposure to the magnet. The results of these two samples were then compared to evaluate the effect of magnetic field on the heat of hydration. Table 4.10 summarizes the results for each mix compositions from Stage 1. Furthermore, the Fig.4.32 and Fig.4.34 demonstrate the effect of magnetic field on R_1 and R_2 systems, respectively. The R1 system with nano-silica shows a considerable increase in the hydration peak and acceleration in corresponding time required to reach the peak value. Moreover, it is observed that the use of nano- particles including nano-silica and nano-alumina triggered the shift of hydration peak towards left as compared to reference R_1 mix. The addition of magnetite powder (R_1M, R_1NSM, and R_1NAM) into R_1 system have also resulted in a slight shift of the hydration peak towards left as compared to the reference

R_1. The Fig 4.32.b explains the effect of magnetic field on heat of hydration of R_1 systems. The total heat of hydration values for R_1 compositions indicate that the magnetic field is helping to accelerate the process of heat of hydration except for R1NAM' mix. The reason for this can be the presence of the component with surfactant in nano-alumina fiber dispersion that has retardation effect or this could also be explained by incompatibility as nano-alumina fibers have shown better results without magnetite powder. In the mix compositions R_1M, R_1NSM and R_1NAM, portland cement is replaced by 5% magnetite powder. These mixes have demonstrated a slight increase of 1% to 8% in the hydration peak values.

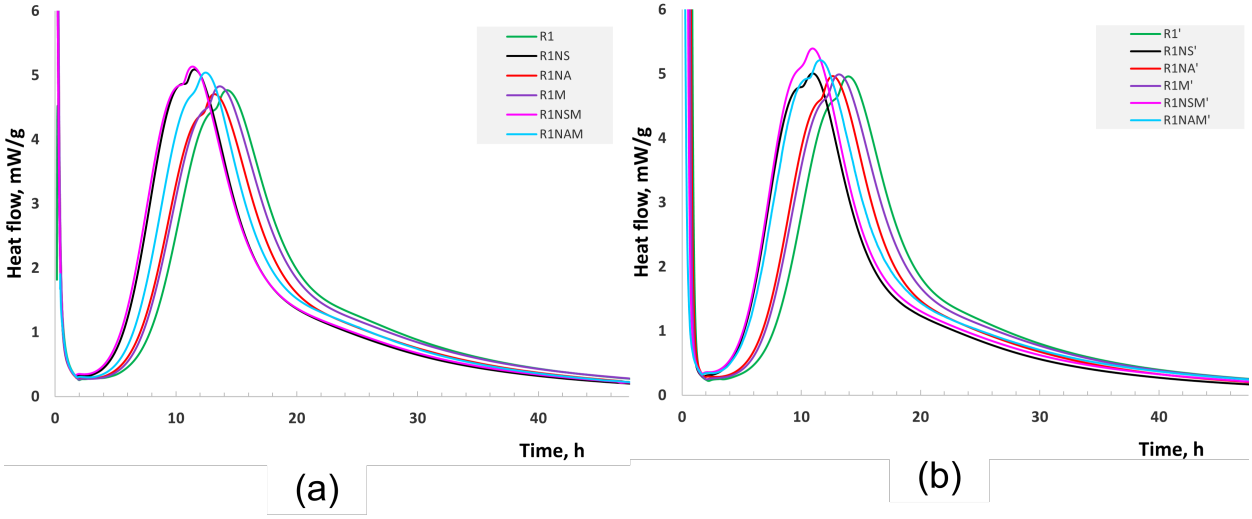


Figure 4.32: The effect of superplasticized portland cement pastes doped with nano-particles R_1 and with magnetite R_1M systems (a) no magnetic field (b) after application of magnetic field

Fig 4.33 and Fig 4.34 demonstrates the heat of hydration curves for R_2 and R_2' systems. In these systems, portland cement is replaced by 50% fly ash (or fly ash and magnetite powder) that indicate a drop in peak of hydration by more than 50% with approximately 6 hours of delay (in the formation of hydration peak) as compared to the reference R_1 composition. It is also observed for fly ash based composition an average of 60% reduction in the total heat evolution at 47.5 hours after the mixing. Similarly to R_1NS and R_1NSM, the R_2NS and R_2NSM compositions report an increase in peak and a shift to left indicating

the acceleration in the process of hydration. Thus, nano-silica proves to be effective in accelerating the process of hydration. Though nano-alumina is not as effective as nano-silica, but it still had significant effect on the formation of hydration peak and accelerating the corresponding time. The hydration peaks in the portland cement systems (R_1 systems) are high and narrower, but for portland and fly ash systems, the peaks are shorter but spread out, hence to thoroughly evaluate the performance of these systems it is necessary to consider other parameters affecting the kinetics of hydration.

Table 4.10: The heat of hydration constants and percentage build up for heat flow and accelerated time for Stage 1 compositions

Mix Id	Mixing Constituents	C_3S hydration Peak		Build up %	**Speed up %	Total Time (hrs)	Total Heat (J/g)
		Time	Heat Flow				
R1	PC+SP	14.08	4.76	3.78	0.28	47.50	239.07
R1'	PC+SP MR	14.04	4.94			47.50	267.46
R1NS	PC+SP+NS	11.47	5.06	-1.38	3.31	47.50	238.39
R1NS'	PC+SP+NS MR	11.09	4.99			47.50	241.07
R1NA	PC+SP+NA	13.06	4.7	4.89	3.68	47.50	234.83
R1NA'	PC+SP+NA MR	12.58	4.93			47.50	239.13
R1M	PC+SP+M	13.36	4.83	3.31	1.50	47.50	248.84
R1M'	PC+SP+M MR	13.16	4.99			47.50	244.46
R1NSM	PC+SP+NS+M	11.21	5.13	5.07	5.80	47.50	242.08
R1NSM'	PC+SP+NS+M MR	10.56	5.39			47.50	244.83
R1NAM	PC+SP+NA+M	12.56	5.11	-1.37	2.55	47.50	252.35
R1NAM'	PC+SP+NA+M MR	12.24	5.04			47.50	231.97
R2	PC+FA+SP	20.37	1.98	0.51	5.55	47.50	136.01
R2'	PC+FA+SP MR	19.24	1.99			47.50	151.56
R2NS	PC+FA+SP+NS	18.24	2.09	8.13	10.36	47.50	138.35
R2NS'	PC+FA+SP+NS MR	16.35	2.26			47.50	155.20
R2NA	PC+FA+SP+NA	20.19	2.14	2.34	5.30	47.50	139.10
R2NA'	PC+FA+SP+NA MR	19.12	2.19			47.50	156.39
R2M	PC+FA+SP+M	19.61	2.19	-0.46	-0.82	47.50	153.76
R2M'	PC+FA+SP+M MR	19.77	2.18			47.50	166.82
R2NSM	PC+FA+SP+NS+M	16.86	2.54	1.97	5.28	47.50	167.31
R2NSM'	PC+FA+SP+NS+M MR	15.97	2.59			47.50	182.68
R2NAM	PC+FA+SP+NA+M	19.04	2.47	1.21	6.57	47.50	156.76
R2NAM'	PC+FA+SP+NA+M MR	17.79	2.5			47.50	158.63

Stage 2 compositions

In the Stage 2 compositions, it is observed that cobalt powder is effectively helping in accelerating the process of hydration when exposed to magnetic field. Table 4.11 reports the hydration peak values, percentage built up and total heat evolution at 48 hours.

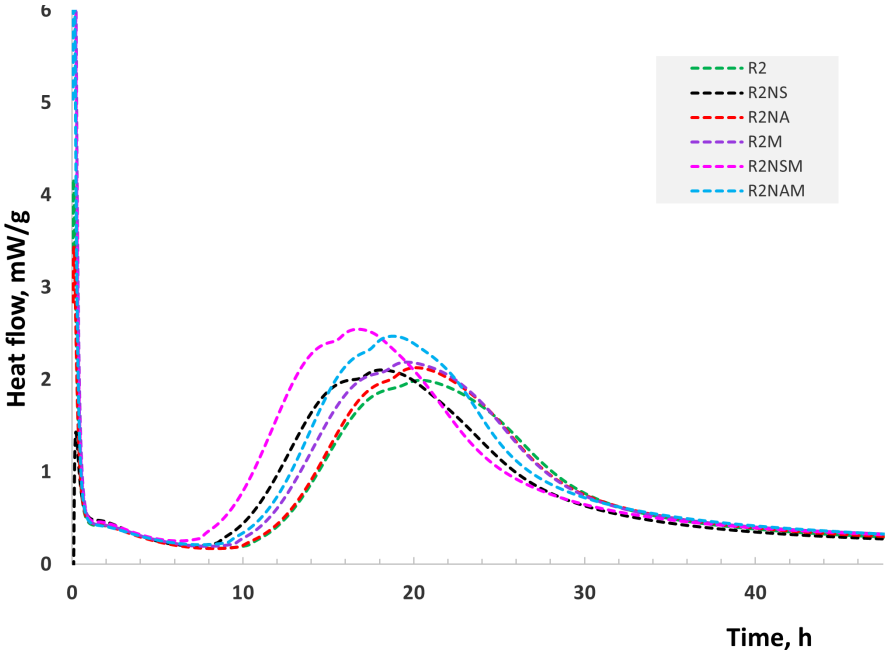


Figure 4.33: The effect of superplasticized portland cement pastes doped with nano-particles R_2 and with magnetite R_2M systems on HOH of the Stage 1 compositions

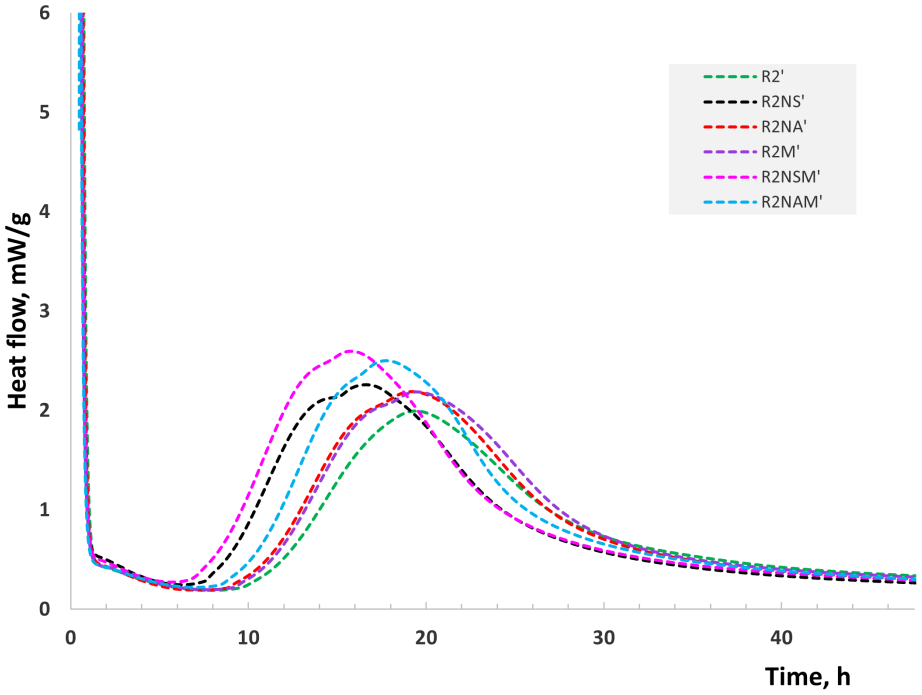


Figure 4.34: The effect of superplasticized portland cement pastes doped with nano-particles R_2 and with magnetite R_2M systems on HOH of the Stage 1 compositions after application of magnetic field

It is further observed that a small replacement of portland cement by cobalt powder has resulted into a slight increase in the hydration peak values with slight shift towards left. The

Table 4.11: The heat of hydration constants and percentage build up for heat flow and accelerated time for Stage 2 compositions

Mix Id	Mixing Constituents	C_3S hydration Peak		Build up %	**Speed up %	Total Heat at 48 hrs (J/g)
		Time	Heat Flow			
R1Co0.01	PC+Co(0.01%)+SP	10.10	5.31	2.22	11.81	237.03
R1Co0.01'	PC+Co(0.01%)+SP MF	8.91	5.43			249.59
R1Co0.1	PC+Co(0.1%)+SP	9.85	5.39	3.24	9.63	228.61
R1Co0.1'	PC+Co(0.1%)+SP MF	8.90	5.56			239.17
R1Co1	PC+Co(1%)+SP	9.86	5.33	0.83	7.62	226.28
R1Co1'	PC+Co(1%)+SP MF	9.11	5.37			234.91

Fig 4.37 represents the total heat evolved for the compositions before the exposure to the magnetic field (X-axis) and after the application of the magnetic field (Y-axis). The dotted black line crossing the graph diagonally helps to distinguish between the compositions that had higher total heat evolution on exposure to the magnetic field.

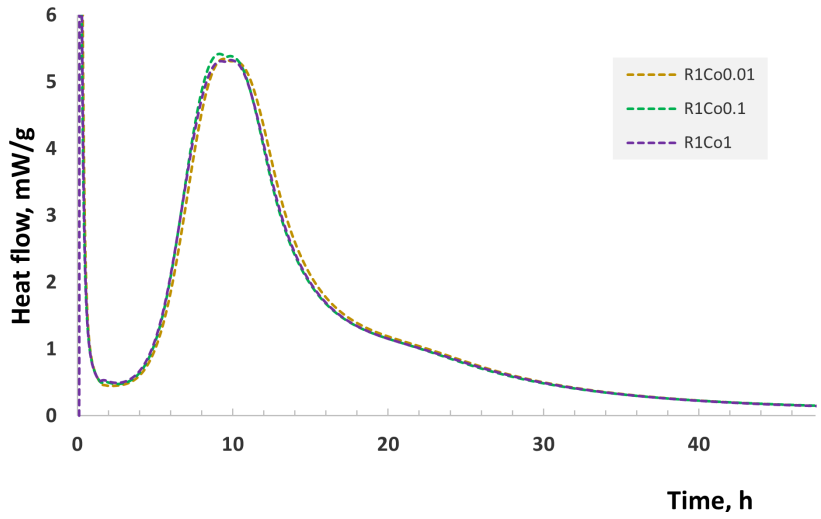


Figure 4.35: The effect of superplasticized portland cement pastes doped with cobalt powder on HOH of Stage 2 compositions

Milled Fly ash compositions

The heat of hydration experiment was performed on three types of fly ash (see section 4.1.2), Oak Creek, Prairie State and LG14 Class F fly ash. All the three fly ash products were milled and magnetically separated. There were three samples for each type of fly ash, reference (unmilled), magnetically separated and non-magnetic fly ash. Each of these

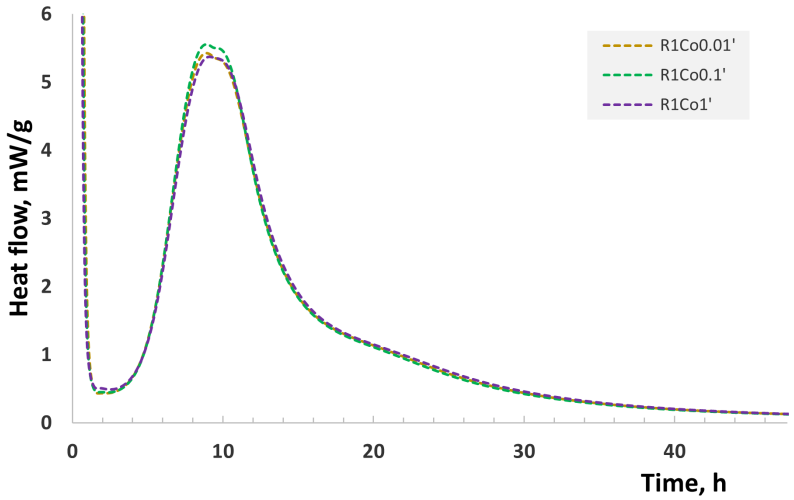


Figure 4.36: The effect of superplasticized portland cement pastes doped with cobalt powder on HOH of Stage 2 compositions after application of magnetic field

products were used at 10% cement replacement using a standard cement paste. In the Fig 4.38, 4.39 and 4.40, the reference Oak Creek Class F fly ash is denoted as R1.1, milled and magnetically separated Oak Creek fly ash as O3M, and non-magnetic ones as O3NM. Similarly, reference Prairie State is denoted as R1.2, milled and magnetically separated as P3M and non-magnetic as P3NM. For LG14, reference is denoted as R1.3, magnetically separated and non- magnetic as LG3M and LG3NM, respectively. Here, the effect of milling and beneficiation of fly ash on heat of hydration was determined. The Fig 4.38, 4.39 and 4.40 demonstrate the heat flow and cumulative heat indicating the total heat evolved during 48 hours for all three fly ash products. It is observed that there are minor deviations in the response of fly ash based systems at a early stage (less than 30 hours) of hydration. In addition to this, Table 4.12 reports a slight decrease in hydration peak for milled fly ash.

Portland cement and Lunar regolith systems

The effect of lunar fine powder on the heat of hydration process is studied by replacing portland cement with 15%, 30%, 45%, 60%, 75%, and 90% in standard cement paste. There

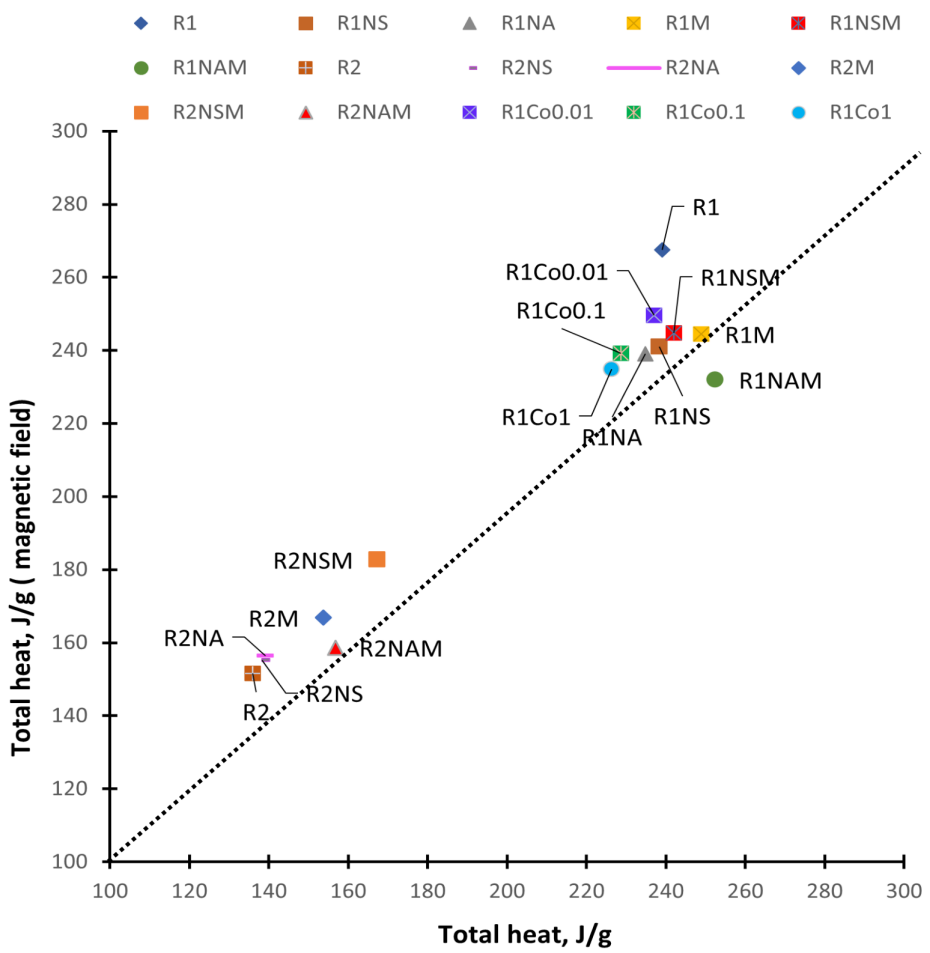
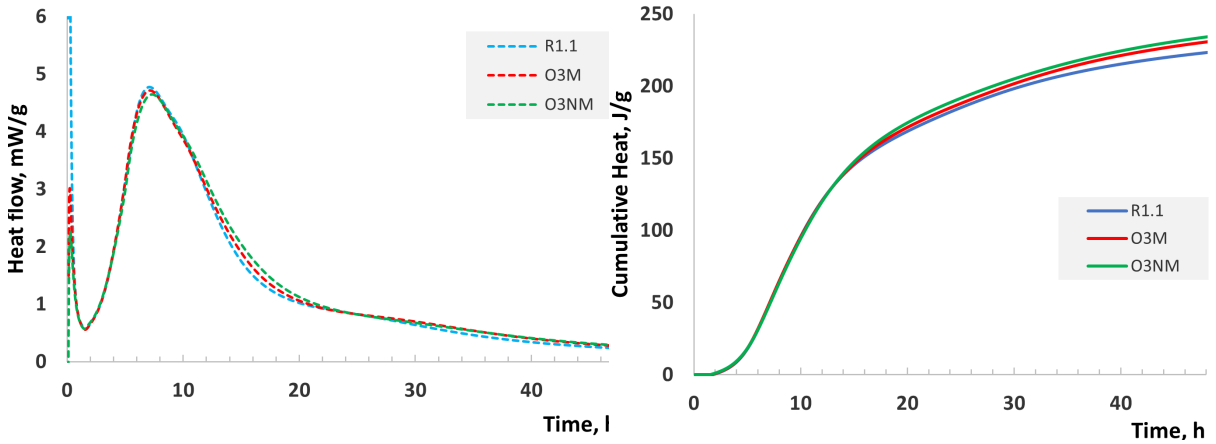


Figure 4.37: The effect of magnetic field on the total heat evolution for Stage 1, Stage 2, and Stage 3 compositions

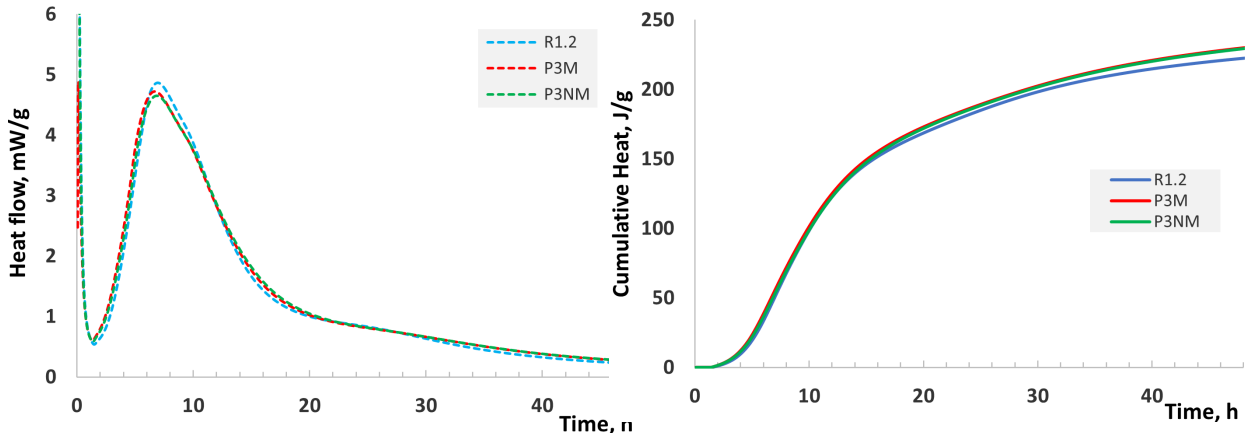


(a) (b)

Figure 4.38: The effect of milling and beneficiation on the heat flow of cement systems with Oak Creek Class F fly ash (per content of cementitious material) (a) heat flow evolution (b) cumulative heat flow

Table 4.12: The heat of hydration constants and accelerated time for milled fly ash compositions

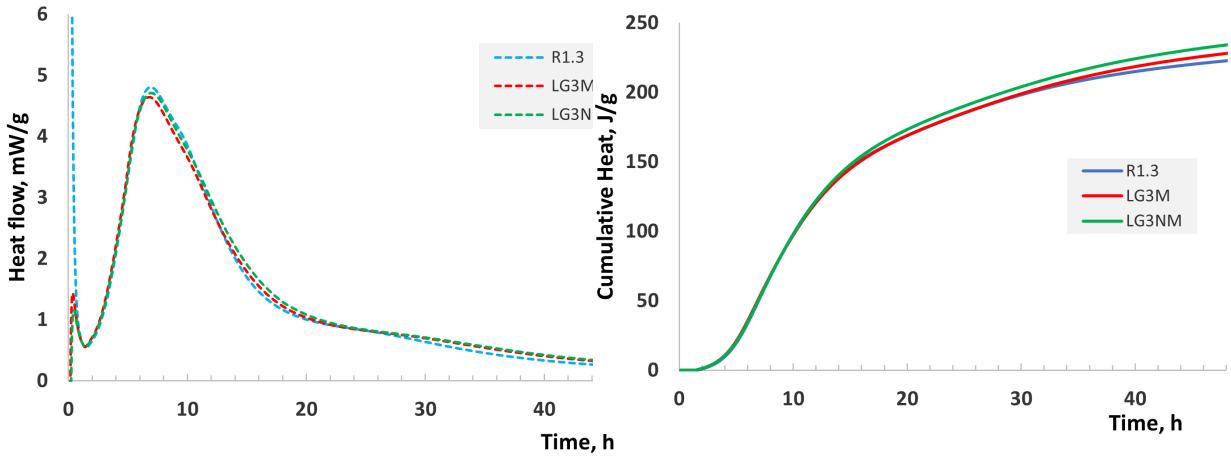
Mix Id	C_3S hydration Peak		Total Time (hr)	Total Heat at 48 hrs (J/g)
	Time	Heat Flow		
R1.1	7.28	4.76	48	223.22
O3M	7.13	4.47	48	230.63
O3NM	7.32	4.65	48	234.08
R1.2	6.96	4.87	48	222.41
P3M	6.69	4.72	48	229.94
P3NM	7.06	4.64	48	229.36
R1.3	7.14	4.79	48	222.64
LG3M	6.79	4.64	48	227.95
LG3NM	6.97	4.71	48	234.05



(a) (b)

Figure 4.39: The effect of milling and beneficiation on the heat flow of cement systems with Prairie State Class F fly ash (per content of cementitious material) (a) heat flow evolution (b) cumulative heat flow

was a total of 7 samples including reference portland cement paste. This test was done twice with fine lunar powder (as received) and milled fine lunar powder. The systems with fine lunar powder (as received) are denoted with prime (') such as LR15', LR30', LR45', LR60', LR75' and LR90'. Fig 4.41 demonstrates that with the increase in the percentage of fine LR, the hydration peak decreases proportionately with the lowest value for composition with 90% fine LR. With the addition of fine LR, peaks are proportionally reduced, but shifted



(a) (b)

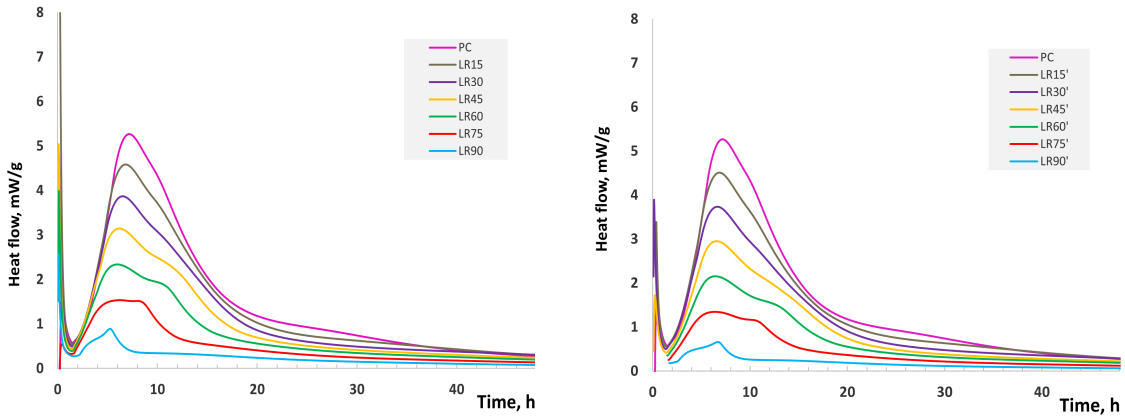
Figure 4.40: The effect of milling and beneficiation on the heat flow of cement systems with LG14 Class F fly ash (per content of cementitious material) (a) heat flow evolution (b) cumulative heat flow

earlier, indicating more complete conditions for cement hydration in diluted systems. It is observed that the process of hydration is accelerated in the milled LR system, thus milling creates hydration sites and finer products leading to an accelerated hydration process.

The Fig 4.42 demonstrates the total heat evolved during hydration process in milled LR systems and LR systems (as received), respectively. It is clearly observed that with the increase of percentage of LR there is reduction in total heat evolved. And this reduction in total heat evolution is proportional to the percentage replacement of portland cement.

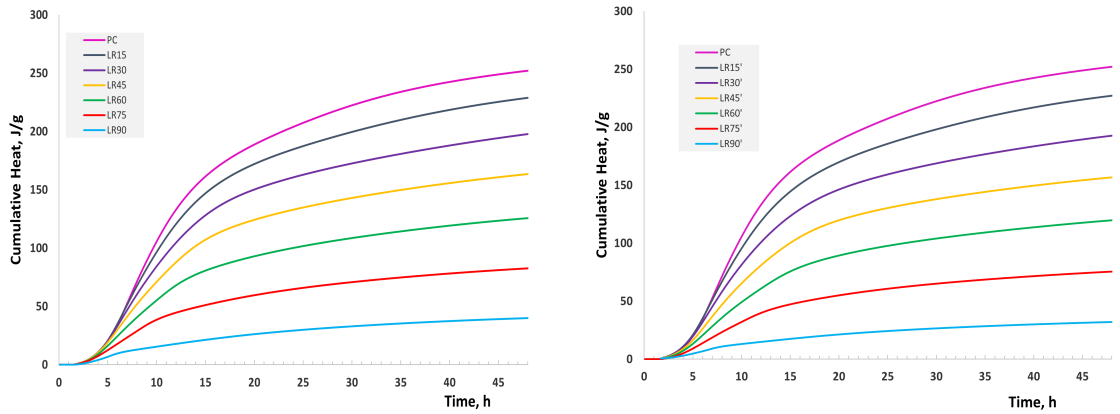
4.5 Compressive strength of developed cementitious inks

The compression test were performed on the samples to determine the effect of milled fly ash and LR on the compressive strength. The 50.8mm cube samples were prepared as per standard specification of ASTM C109 with water to cementitious material ratio (w/c) of 0.485 and sand to cementitious material ratio (w/s) of 2.75. The detailed mix composition is given in the section below. The densities of Class F Oak Creek fly ash after milling and



(a) (b)

Figure 4.41: The effect of fine LR on the heat flow of cement systems (a) fine LR milled (b) fine LR (as received)



(a) (b)

Figure 4.42: The effect of fine LR on the heat flow of cement systems (a) fine LR milled (b) fine LR (as received)

for lunar rock used in this project are evaluated by Lafarge Holicim (Table 4.13).

Table 4.13: The densities of the cementitious products used for ink design

Sample	Density, g/cm3
LR 1	2.76
LR 2 Fine Powder	2.78
LR 2 Coarse Sand	2.75
OC	2.49
OC3M	2.97
OC3NM	2.51

4.5.1 Portland cement and milled fly ash systems

The compressive strength at the age of 7 days, 28 days and 90 days for the samples cured in lime water at 21±1°C was evaluated for three mix compositions: reference (with 10% Oak Creek fly ash) (1); compositions with 10% of magnetically separated and milled fly ash (1M) and with 10% of non-magnetic (milled) fly ash (1NM), Table 4.14. The mix proportions used for casting 50.8mm cubes was specified as per ASTM C109. The compressive strength achieved for these samples is reported in the Fig 4.43. It is observed that the compressive strengths of magnetically separated and non magnetic fly ash samples is actually very close. Moreover, milling and separation of fly ash did not significantly affect the strength performance. The 26% decrease in 7-day compressive strength was observed in OC3M as compared to reference sample (OC), however only 12% decrease was observed for OC3NM samples indicating a faster reaction of activated pozzolanic component of fly ash. This demonstrates that fly ash contribution to strength development for milled and magnetically separated samples initiates only after 7 days of standard curing. The 28-day strength of compositions with milled ash (magnetically beneficiated and non magnetic) portland cement composition are similar. Furthermore, 90-day strength results indicate little variation of 1MPa.

Table 4.14: The compositions for mortars based on milled fly ash systems.

MIX ID	Mixture proportioning (g)			
	PC	Oakcreek fly ash	Sand	Water
OC	90	10	275	48.5
OC3M	90	10 *	275	48.5
OC3NM	90	10**	275	48.5

* 3 hrs milled magnetically separated Oak Creek Class F Fly ash
** 3 hrs milled non-magnetic Oak Creek Class F Fly ash

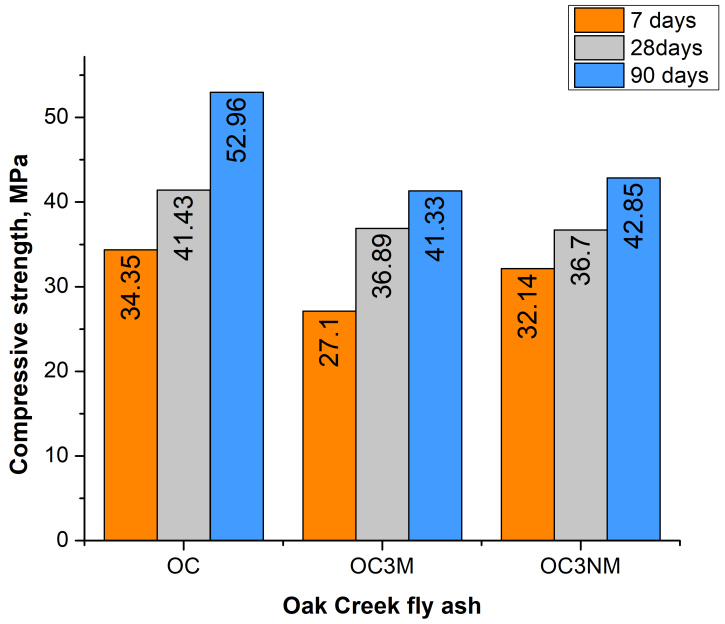


Figure 4.43: Compressive strength for milled and beneficiated Oak Creek fly ash compositions.

4.5.2 Portland cement and Lunar regolith systems

The Section 4.2 defines the simulated LR materials used in this research. The samples of simulated LR received were classified into two types fine (powders) and coarse (sand). An attempt is made to replace cement with the fine LR and sand with coarse LR material in the cement based mortar. The mortar samples were prepared as per ASTM C109 and tested for compressive strength. Fine LR based mortar were tested for the age of 7 days, 28 days and 90 days age, whereas samples based on LR sand were tested for the age of 1

day, 7 days, 28 days and 90 days. The compressive strength for fine LR powder samples is reported in the Fig. 4.44 and 4.45. Here, no significant change in strength is observed between milled and unmilled LR samples. As the percentage of LR in the mortar increases, the strength decreases, which was expected for inert fillers. There has been a proportional increase in strength of the samples with time. Table 4.16 explains the mix design composition based on LR sand system. The LR sand samples received were characterized and used as a replacement for aggregates (standard sand). The reference mix is denoted as "A" consists of standard mix design as specified by ASTM C109. In mix "B", coarse aggregate is replaced by LR sand. Here, the LR sample was crushed in a vibrating mill to get the particle size distribution similar to standard sand. In mix "C", 60% of total sand was replaced by LR sand (unmilled) and in the mix "D", standard sand was replaced by crushed LR sand. Here, LR sand is processed to achieve the particle size distribution similar to 0.45 power curve (Fig 4.10). The compressive strength for coarse LR is reported in Fig 4.46 for the age of 1 day, 7 days, 28 days and 90 days. It is observed that there has been 6.3%, 31% and 68% increase in 90-day strength for samples B, C, and D, respectively as compared to the reference sample A.

Table 4.15: The mix compositions for fine LR systems.

MIX ID	Mixture proportioning (g)			
	PC	LR Fine	Sand	Water
PC	100	-	275	48.5
LR15	85	15	275	48.5
LR30	70	30	275	48.5
LR45	55	45	275	48.5
LR60	40	60	275	48.5

This mix composition was used for both LR (as received) (LR15', LR30', LR45', LR60') and milled LR

Table 4.16: The mix compositions for LR sand systems.

MIX ID	Mixture proportioning (g)			
	PC	LR sand	Sand	Water
A	100	-	275	48.5
B	100	275*	-	51.2
C	100	165	110	48.5
D	100	275**	-	48.5

*Sand quantity is replaced by LR sand (LR2C1, LR2C2, LR2C3) which was milled to get standard sand sieve analysis curve.
**Sand quantity is replaced by LR sand (LR2C1, LR2C2) which was milled to get 0.45 sieve analysis curve.

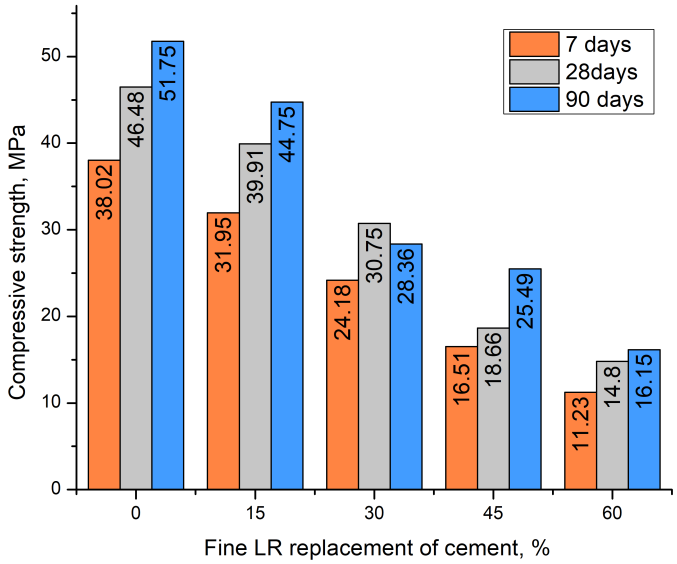


Figure 4.44: Compressive strength for compositions with cement replacement by Fine LR.

4.5.3 Fiber-reinforced composites

The fiber-reinforced composite was considered for implementation of developed inks in auxetic materials and 3D printing. The compressive strength of the fiber-reinforced composite at the age of 21 days was evaluated. The composition was designed with w/c ratio of 0.3 and

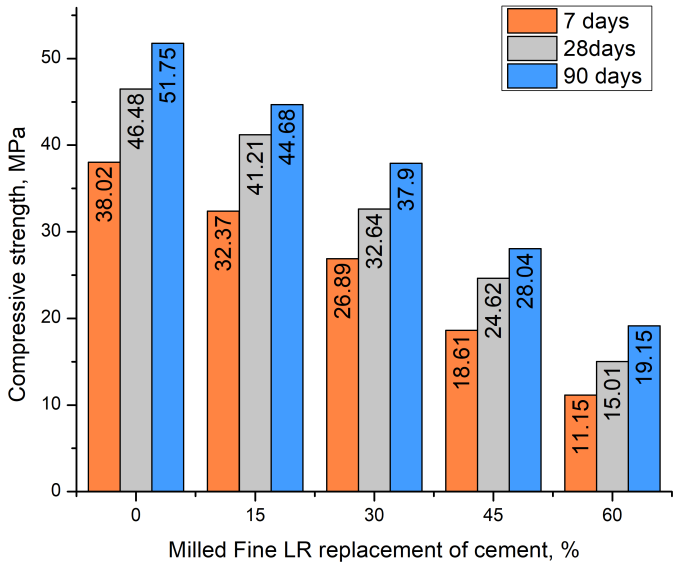


Figure 4.45: Compressive strength for compositions with cement replacement by milled Fine LR

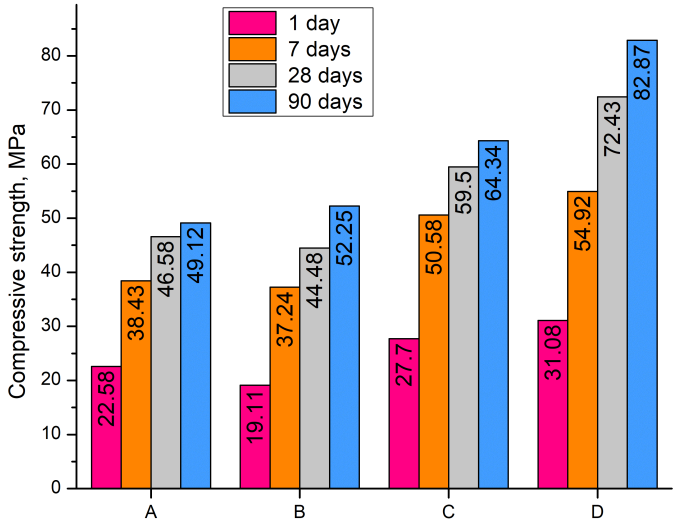


Figure 4.46: Compressive strength for compositions with aggregates replacement by coarse LR.
Note: A= reference standard mortar (ASTM C109), B= samples with coarse LR replicating standard sand, C= samples with 40% LR sand replacing standard sand, and D= samples with LR sand replication 0.45 curve.

s/c ratio of 0.5. In addition, nano-alumina fibers at 0.25% by weight of cement, metakaolin at 1% by weight of cement, and 1.8% of HDPE fibers by volume of cement were used in the fiber-reinforced composite. Three types of cubes were tested; standard cube, cube with one notch and cube with two notches as in Fig 4.47. The standard cube and cube with one notch were tested for compression, whereas cube with two notches was evaluated using splitting test. The load-displacement curve for standard sample was determined using strain gauges and a strain pod. The Fig 4.48 demonstrates the load-displacement curve for the fiber-reinforced composite sample. The 21-day compressive strength of 132 MPa was achieved for developed fiber reinforced composite. The cube test results for the samples with two notches is reported in Section 4.5.5.

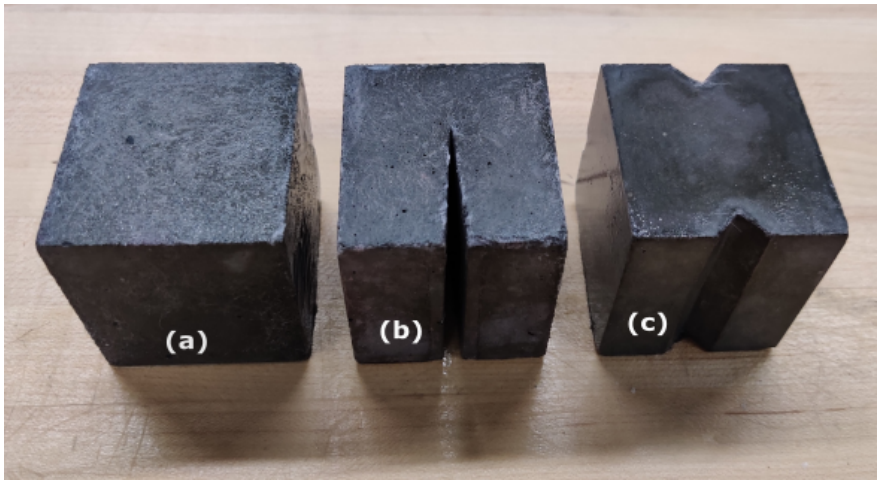


Figure 4.47: The fiber reinforced composite cubes: (a) standard cube, (b) cube with one notch, (c) cube with two notches

The Fig 4.49b demonstrates the load- displacement curve for cube with one notch. The first crack formation is observed at 0.7 mm displacement and corresponding load of 7,500 N.

4.6 Bending response of fiber-reinforced composites

The bending response of fiber-reinforced composites is studied for three beam samples; one reference beam sample (6” X 1.5” X 0.5”), beam with v notch (8” X 1.5” X 0.5”) and beam

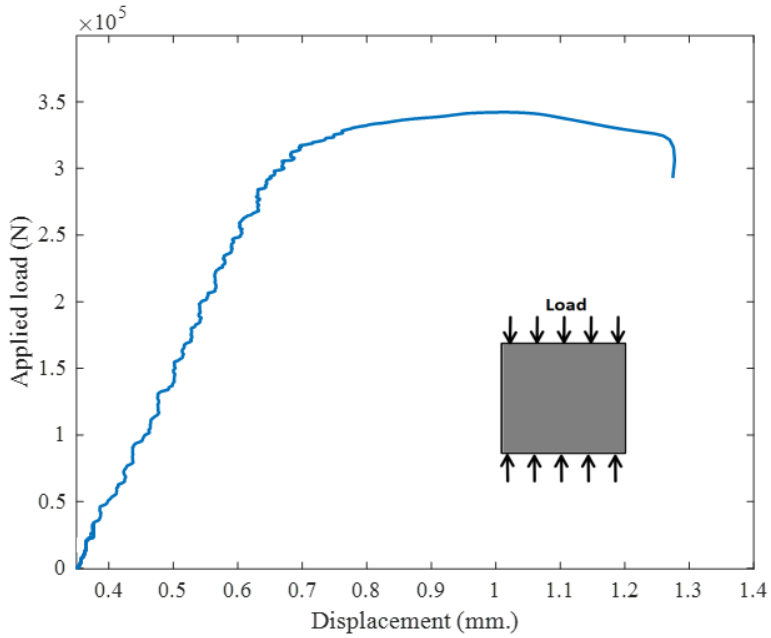
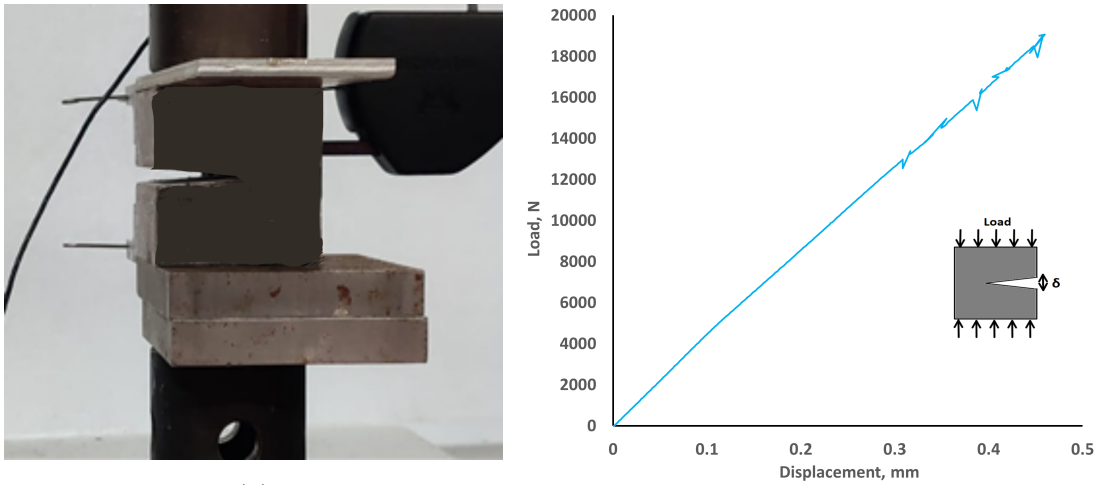


Figure 4.48: The load-displacement curve for fiber-reinforced composite for cube sample



(a) (b)

Figure 4.49: The cube with one notch is tested for compression: (a) experimental set up, (b) The load-displacement curve for cube with one notch

with c notch (6" X 1.5" X 0.5") as in Fig 4.50. The triangular v notch with base 6 mm and height 20 mm and semicircular c notch with 1/16" diameter are exactly at the center of the respective beams. The reference beam and beam with v notch are subjected to four point bending load acting as deep beam as reported in Fig 4.51 and Fig 4.52, respectively. The load displacement curve for these beam indicates that the fibers in the beam are controlling

the cracking and increasing the structural integrity of the beam.



Figure 4.50: Thee types of beam samples tested in this study

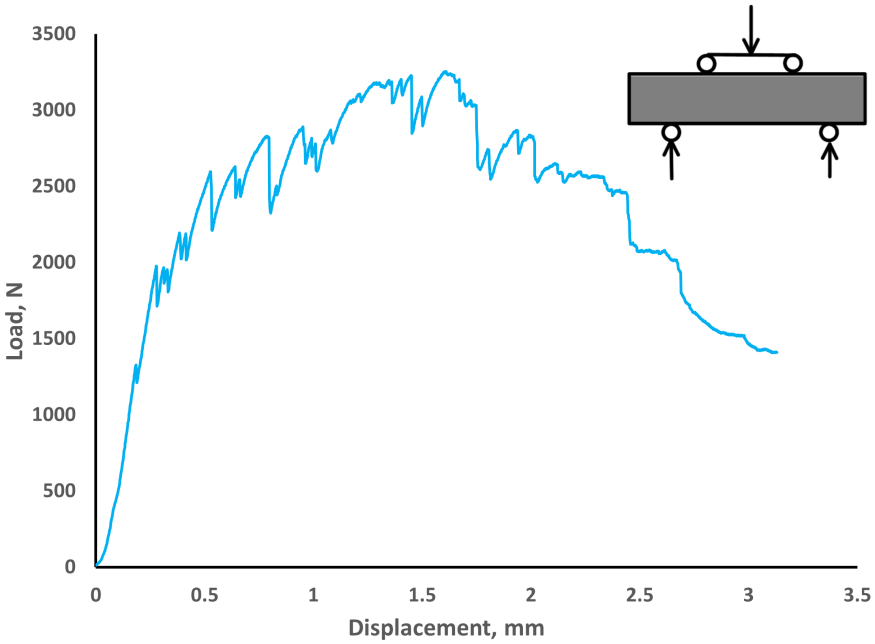


Figure 4.51: The four point bending test for reference beam loaded in the direction parallel to its greater depth

Further, the reference beam and c- notch beam are subjected to four point bending load as shown in Fig. 4.53 and Fig. 4.54. The maximum load capacity of reference beam is 1,100 N, whereas when the the same beam is loaded like deep beam, its capacity was observed to be much higher around 3,200 N. The reason for this behavior is that when the beam is loaded like deep beam, it has more depth as compared to when loaded flat.

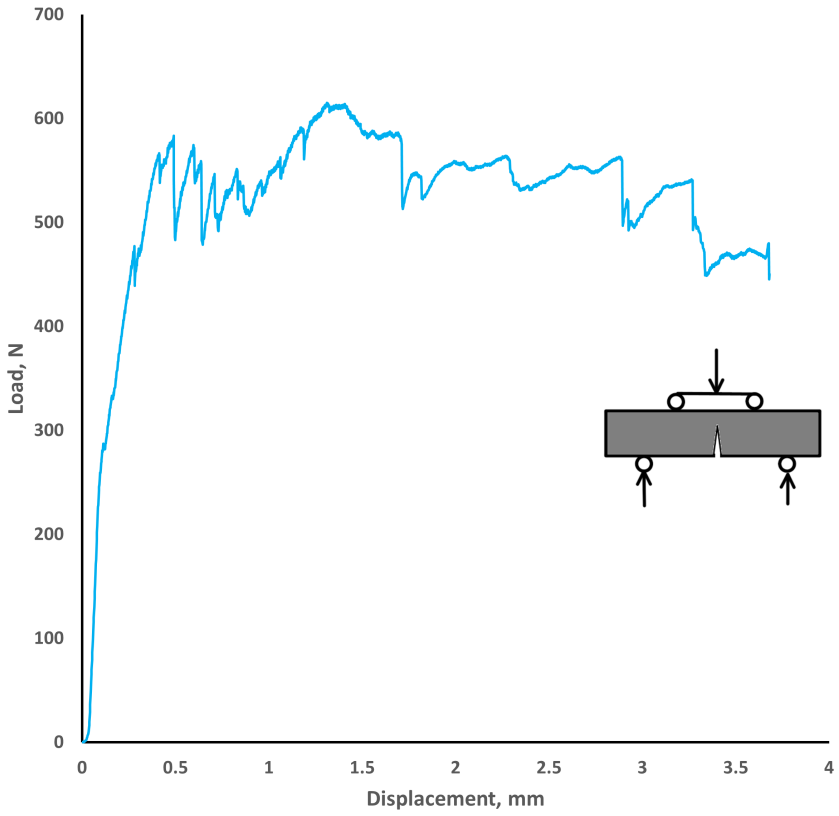


Figure 4.52: The four point bending test for v- notched beam loaded in the direction parallel to its greater depth

4.7 Tensile response of fiber-reinforced composites

4.7.1 Splitting/ wedge test

The fiber reinforced composite cube with two notches was evaluated using splitting test (Fig 4.55.a) and the corresponding load displacement curve is reported in Fig 4.55.b. The first crack is observed at 0.48 mm displacement and corresponding load of 13,000 N. It is also observed that the fibers help the cube to resist the failure after the peak loading.

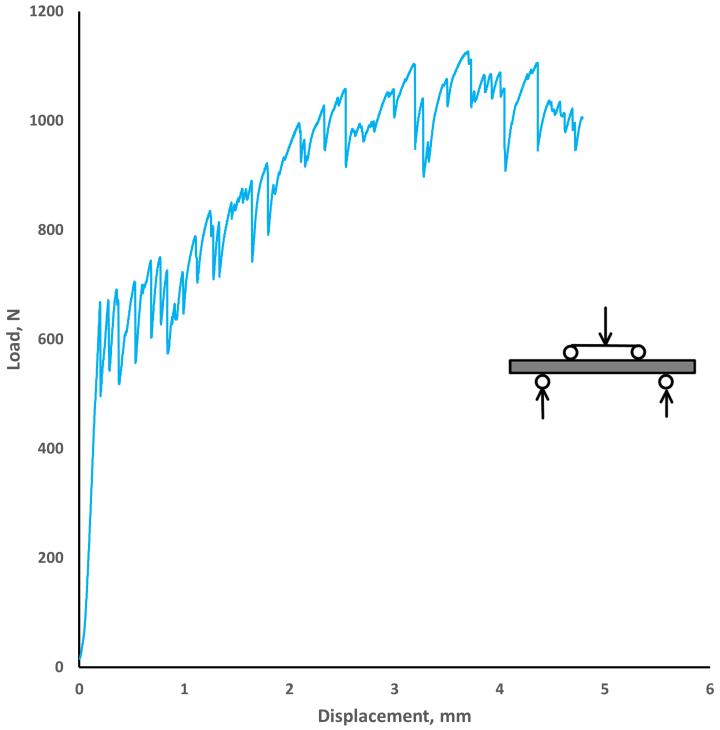


Figure 4.53: The four point bending test for reference beam loaded in the direction parallel to its smaller depth

4.7.2 Direct tension response

The two beam samples, reference beam and a beam with v notch were tested for tension as the concrete cracking strength is the function of tensile strength subjected to pure tension. The Fig 4.56 and Fig 4.57 demonstrates the load displacement curve for reference beam and v notched beam, respectively.

4.7.3 Characterization of notched samples

In order to characterise the auxetic geometry and to study the effect of geometrical extrusions, v-notched beam was tested under tensile load. The Fig 4.57 reports the load-displacement curve for notched beam under tensile loading.

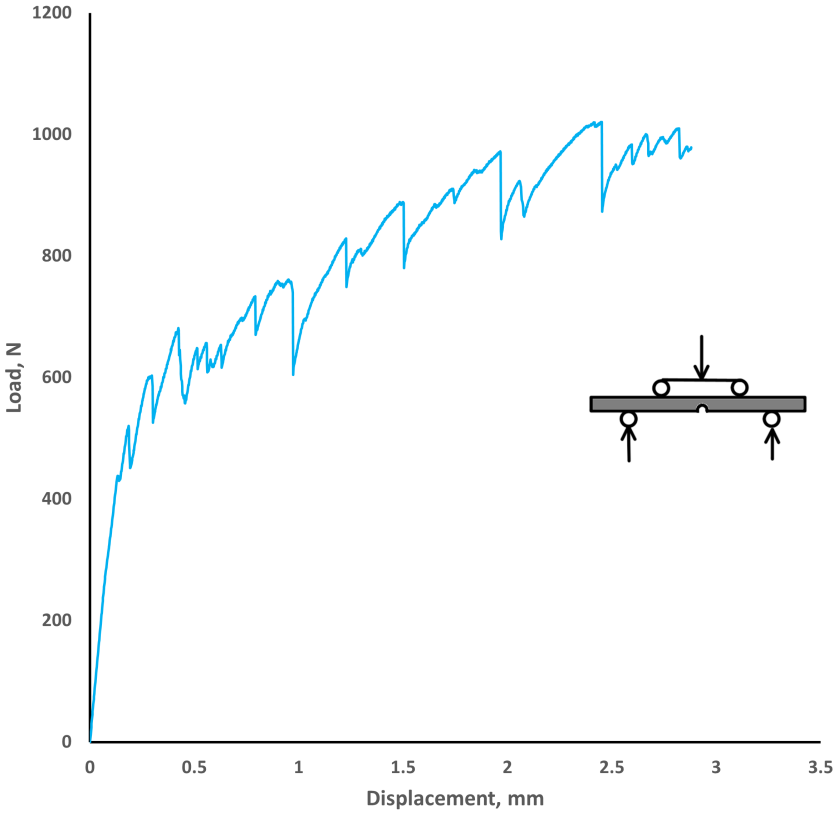


Figure 4.54: The four point bending test for c-notched beam loaded in the direction parallel to its smaller depth

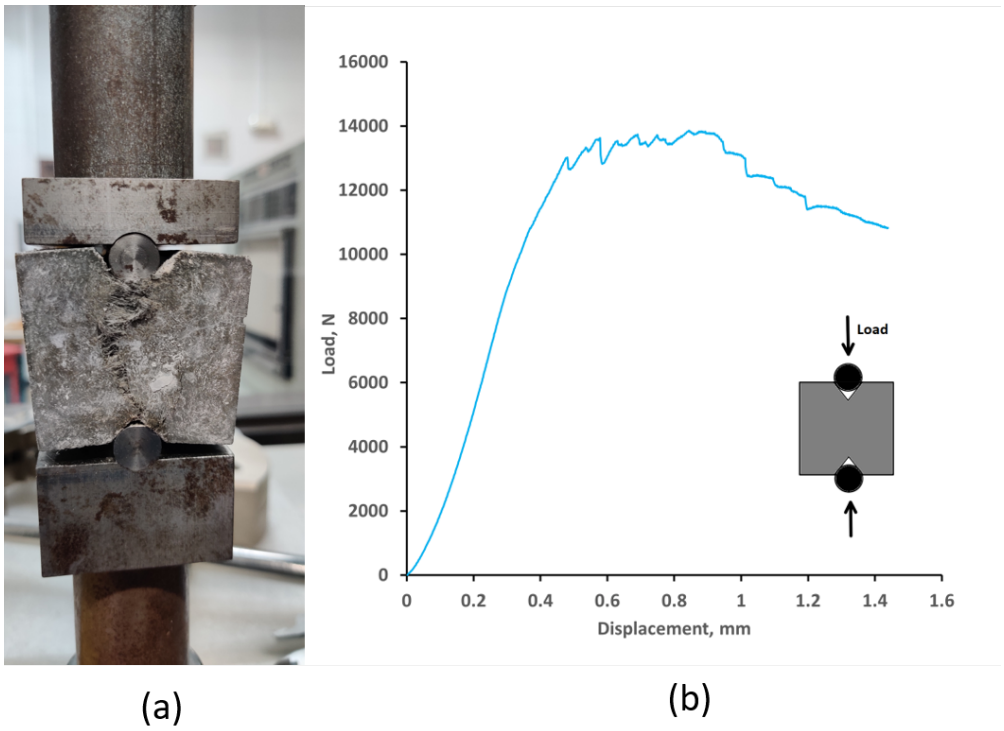


Figure 4.55: The cube with two notches is tested for compression: (a) experimental set up, (b) The load-displacement curve for cube with two notches

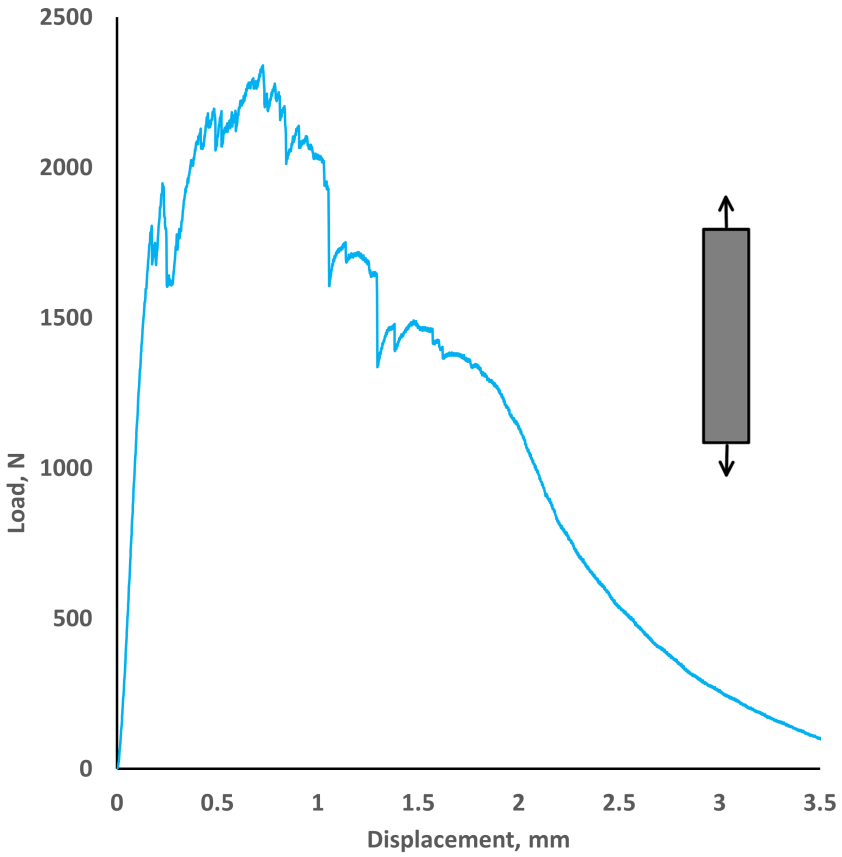


Figure 4.56: The load-displacement curve for reference beam subjected to tensile load

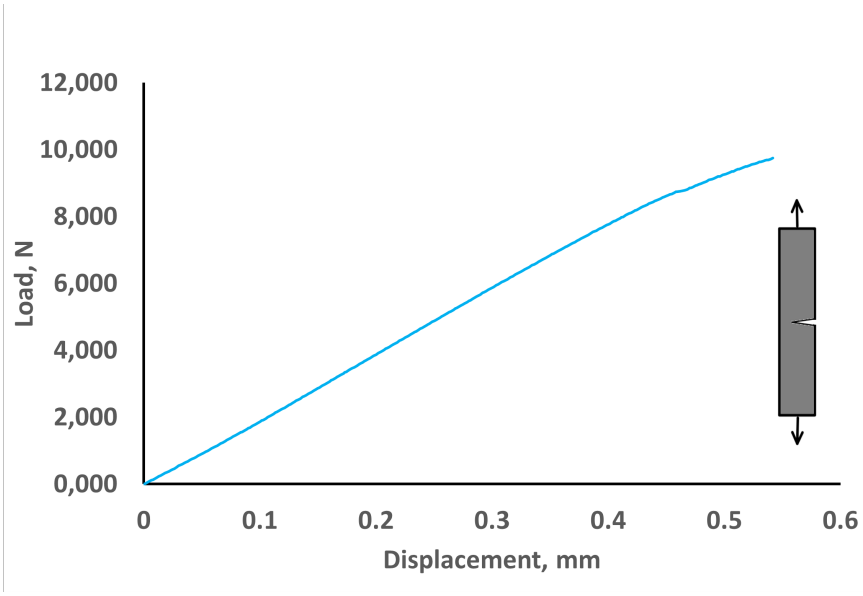


Figure 4.57: The load-displacement curve for v-notched beam subjected to tensile load

Chapter 5

Design philosophy and practical applications of auxetic concrete

There has been significant research effort on digital manufacturing of complex structures, but one of the major limitation for 3D printing is related to incorporating of reinforcement into the structures; and this limitation remains a major hindrance in the implementation of 3D printing. The reported research can eliminate a need for reinforcement bars by introducing fiber reinforcement into auxetic metamaterial exhibiting negative apparent Poisson's ratio using Origami and Kirigami (OAK) inspired structural design. This design, coupled with fiber reinforcement, can provide the tunable thermal expansion response and reduce or even eliminate the need for rebar reinforcement.

Thermal response is an important factor to be controlled for the long-term response and stability of the structures. The coefficient of thermal expansion (CTE) of the structural materials and members is one of the key parameters considered in the design. Selecting the material with lowest CTE is one of the solution to achieve the thermal stability, reduce the associated deformations and so improve the efficiency of the structures. Metamaterials and meta structures (structural shapes) with zero apparent Poisson's ratio and an ability to accommodate thermal stresses very low CTE were proposed for application in biomedical engineering, aerospace and smart textiles but, it is not always possible to use such materials due to costs, weight or the incompatibility with conventional structural systems. Here, the

geometry of the entire structure can be tuned in a such a way that the structure exhibits zero thermal deformation and associated connection issues. For example; when a honeycomb structure is under temperature gradients, the metamaterials inserts can be tuned to compensate the overall honeycomb cellular structure deformation. The smart response involving bending and plastic deformations of elements can be tuned to effectively cancel the overall expansion or contraction so that, with appropriate specification of the materials and geometry, a zero, (or negative, as per a design target) effective thermal expansion is achieved [74].

The geometry of the structural element at macro (full-scale) and intermediate scale affects the stiffness response and other properties of the structure. Hence, developing effective geometrical design using Origami and Kirigami (OAK) based structures becomes important for future applications. It is envisioned that the OAK system is a technology that can be used to make a lightweight but stiff structures also suitable for rapid deployment. With zero thermal response, folded-core and honeycomb-core sandwich panels are examples of the former applications when the proposed approach is used at an intermediate scale element and macro-scale design. Here, folded core panels are lightweight composite structures that can be fabricated by folding and assembling of thin sheets [75]. These OAK inspired elements can be tuned to exhibit a negative apparent Poisson's ratio are also called auxetic metamaterials when the proposed approach is used at a micro-scale. Auxetic metamaterials and structural elements have received considerable attention due to their unusual properties and potential applications in different fields such as defense (body armor), materials engineering, fashion designing (such as shoes and clothing) and medical (knee and elbow pads). The reported research defines the structural components of the auxetic metamaterial which is self-folding, self-adaptable, and with potential zero thermal response which can be 3D printed based on

developed nano-engineered concrete ink.

5.1 Auxetic metamaterials and structures

Metamaterials are the wide class of tailored artificial materials with obscure properties that are usually not found in naturally occurring deposits. This class of materials has received immense attention due to their unusual properties and potential applications in different fields. Recently, the most demanding subclass of mechanical metamaterials named 'auxetic' materials [8] is been proposed due to unique counter-intuitive deformation response. Here, conventional materials contract in the transverse direction when subjected to uniaxial tensile load, whereas auxetic material demonstrates expansion in the transverse direction on the application of uniaxial tensile load (as defined in Section 2.7 and Fig 2.4).

The magnitude of this transverse deformation is governed by a material property defined by Poisson in 1827 [76] as a Poisson's ratio (PR). The PR is formulated as the ratio of transverse strain (ϵ_x) to longitudinal strain (ϵ_y) along the direction of the applied load. Negative Poisson's ratio have not been observed in nature [16], but it has enormous potential to improve the mechanical properties such as enhanced shear, indentation resistance, damping and fracture toughness. The macroscopic mechanical properties of the system are expected to be governed primarily by the geometrical structure of the system rather than by its material composition [77]. For isotropic materials (a material class that does not have preferred orientation), the Poisson's ratio ranges from -1 to 0.5 whereas for anisotropic materials, this range does not apply. Analysis of the tensorial elastic constants of anisotropic single crystal cadmium suggests that Poisson's ratio may attain negative values in some directions [16]. Anisotropic, macroscopic two-dimensional flexible models of certain honeycomb structures (assemblies) can exhibit negative PR in some directions [78]. These known examples depend

on the presence of a high degree of anisotropy; the effect only occurs in some directions and may be dominated by coupling between tensile force and shear deformation [16].

Auxetic materials or assemblies with negative apparent PR can be achieved from the cumulative behavior of repeated functional units when arranged in a specific order. The internal structure of this element can be designed using a geometrical configuration which will exhibit an auxetic effect. This geometrical configuration is achieved using various approaches such as kirigami, origami, chirality and star systems. Various geometrical structures and models that can result in auxetic behavior have been discovered, studied, tested and validated [79]. For a better understanding of how the auxetic effect is achieved using its topological optimization, it is essential to understand the geometrical classification of auxetic materials. Normally, the auxetic materials are primarily classified based on the concept on which their internal structure is derived: such as origami-inspired auxetic material (Oriauxetic), kirigami inspired auxetic material (Kiriauxetic), chiral auxetic material (Chirauxetic) and star-shaped auxetic material (Starauxetic) Figure 5.1.

5.1.1 Classification of auxetic metamaterials

Origami ('oru' means folding and 'kami' means paper) is a Japanese word associated with the art of folding paper [80]. For decades, origami inspired structures have been eye catching and motivating the design and functionality of engineered objects. The implementation of origami is straight forward, it assembles two-dimensional components that are easy to manufacture such as sheets and plates into three-dimensional structures. More recently, researchers became curious about the utilization of active materials that convert various sorts of energy into mechanical work to supply the specified folding behavior in origami structures.

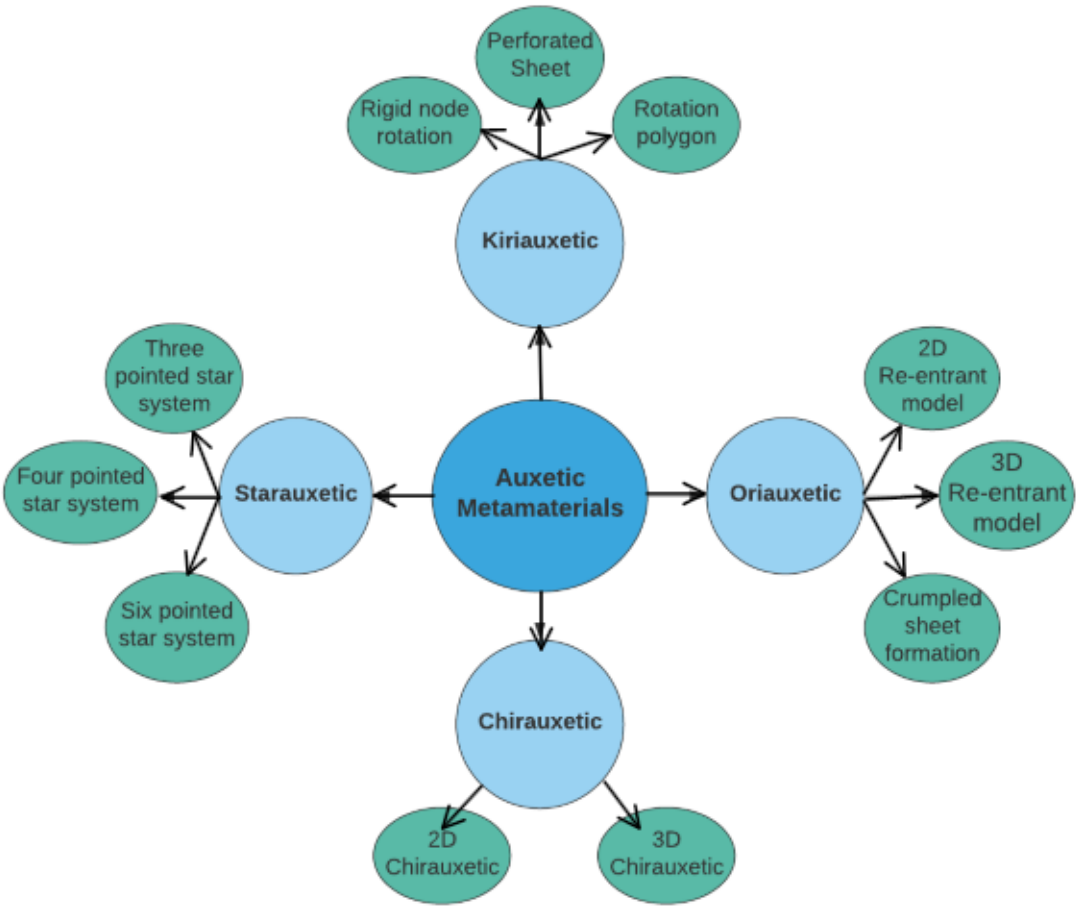
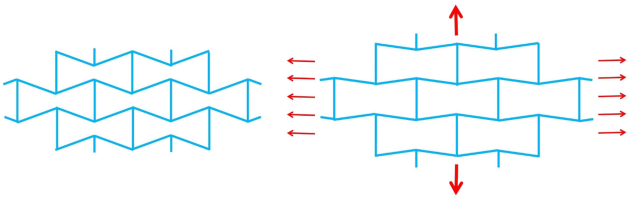


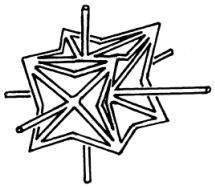
Figure 5.1: Classification of auxetic metamaterials

Such structures are termed active origami structures and are capable of folding and unfolding without the application of external mechanical loads but rather by the stimulus provided by thermal, chemical, or electromagnetic impulse [80]. Such active origami structures made up with repetitive unit cells can demonstrate negative PR. Based on the behavior and response of the structure, the origami oriented auxetic metamaterials are further classified as 2D re-entrant (Figure 5.2a), 3D re-entrant (Figure 5.2b) and crumpled sheet formation (Figure 5.2c). A conventional honeycomb geometry exhibits a negative apparent Poisson's ratio; but when honeycomb structure based on origami is given re-entrant folds, the resulting geometry demonstrates the auxetic behavior with negative apparent Poisson's ratio.

There are auxetic metamaterials whose cellular geometry is based on Japanese art called



(a) 2D re-entrant structure



(b) 3D re-entrant structure



(c) Crumpled sheet

Figure 5.2: The examples of origami-inspired structures

kirigami. Kirigami ('kiru' means cut and 'kami' means paper) is a variation of origami that engages strategically configured arrays of cuts to attain desirable topology of the structure on folding. The kirigami approach exhibits high extensibility resulting in stress delocalization over numerous presets of deformation points [81]. This enhanced potential of kirigami inspires researchers to develop the auxetic metamaterials using kirigami approach. Furthermore, kirigami inspired auxetic metamaterials have potential for shape changing applications such as morphing structures [82].

Based on the geometrical configuration and behavior of the cuts, kirigami-based metamaterials are further classified into three major classes namely perforated sheet nodes (PSN) (Figure 5.3 [83]), rigid node rotation and rotating polygonal auxetic metamaterials. Perforated sheet models are considered as an extension to rigid node rotation auxetic materials, where the PR of the system can be tuned and drastically altered by varying the length of

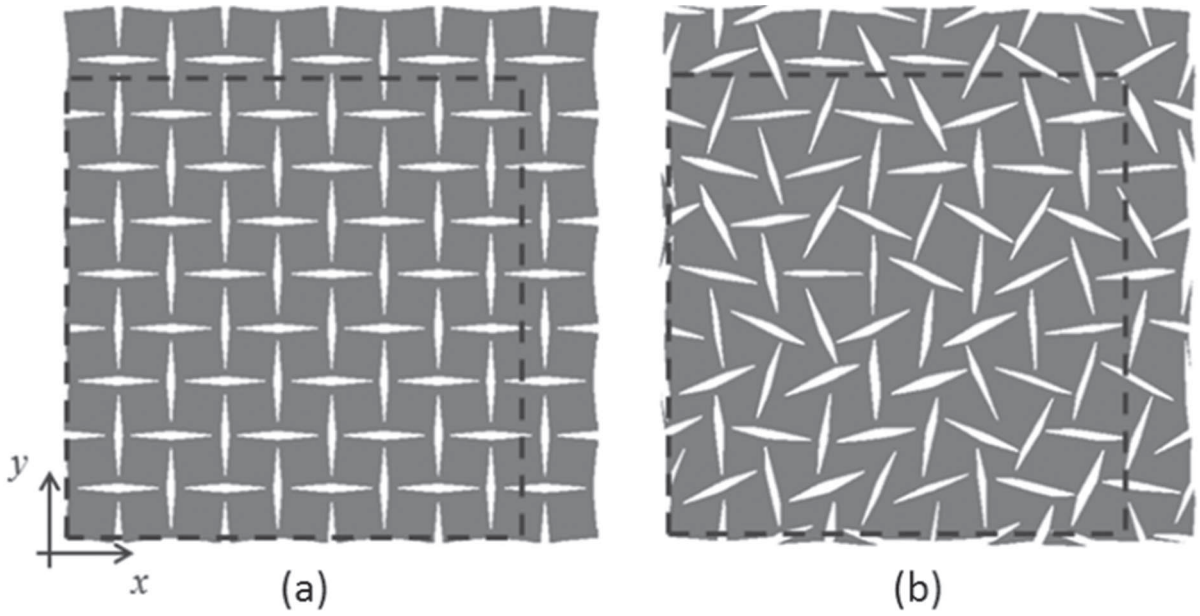


Figure 5.3: The PSN materials a) alternative horizontal and vertical slits forming squares; b) random perforations forming hexagon [78]

the cuts. The isotropy of the system is controlled by the degree of rotational symmetry of cut-patterns, where three- and six-fold symmetry results in an isotropic response while two and four fold symmetry results in anisotropic response [84]. Here, the auxetic behavior can be easily tuned by varying the length of the cuts and it is retained under large levels of applied deformation beyond the limit of small strains [84]. Figure 5.3 explains that irrespective of the arrangements and randomness of the cuts, the perforated sheets demonstrate the auxetic behavior, concluding that high degree of symmetry is not required for the perforated kirigami oriented material to exhibit the auxetic response [83]. This feature enables considerable design freedom for creating auxetic configurations which can be applicable to concrete structures including construction on Moon and other planets.

Auxetic materials and assemblies reveal numerous outstanding properties which are not observed in conventional materials and can be effectively incorporated into cement based composite structures, such as increase in shear resistance [9], increased indentation resistance [10, 11], energy absorption [8], fracture resistance [12], variable permeability [13, 14, 15],

ability to undergo a synclastic curvature [16], increased toughness and sound dampening properties [17].

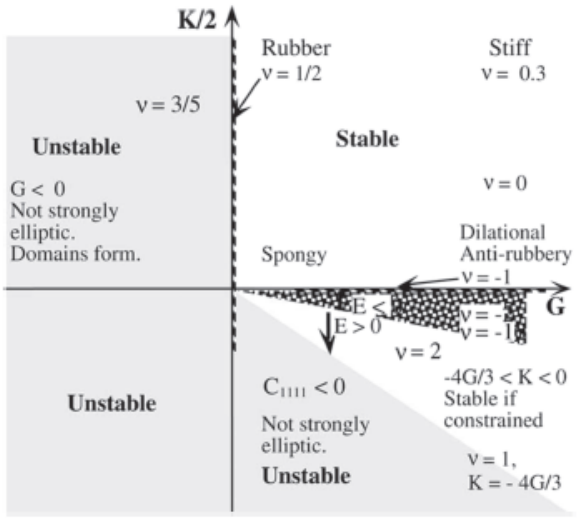


Figure 5.4: Map of bulk modulus and shear modulus with regions of negative PR and negative stiffness [4]

The elastic behavior of the material can be expressed using four constants, namely the Young's modulus (E), the shear modulus (G), the bulk modulus (K) and the Poisson's ratio (ν). For isotropic material, the four constants are interdependent and the Poisson's ratio ranges from -1 to 0.5. The relationship between these constants is given by the following equations; G=E/(2*(1+ν) and K=E/(3*(1-2ν)). From these equations, it is observed that shear modulus increases with decrease in Poisson's ratio and, as result, significant increase in shear resistance is achieved. If the Young's modulus is maintained constant by changing the microstructure of the material, with the change in Poisson's ratio, the values of K and G can be altered. The range of E corresponding to instability and stability under different conditions is plotted in the Figure 5.4. When the value of Poisson's ratio approaches -1, a very high shear modulus (nearly infinity) can be obtained. Simply, the material becomes difficult to shear but easy to deform volumetrically.

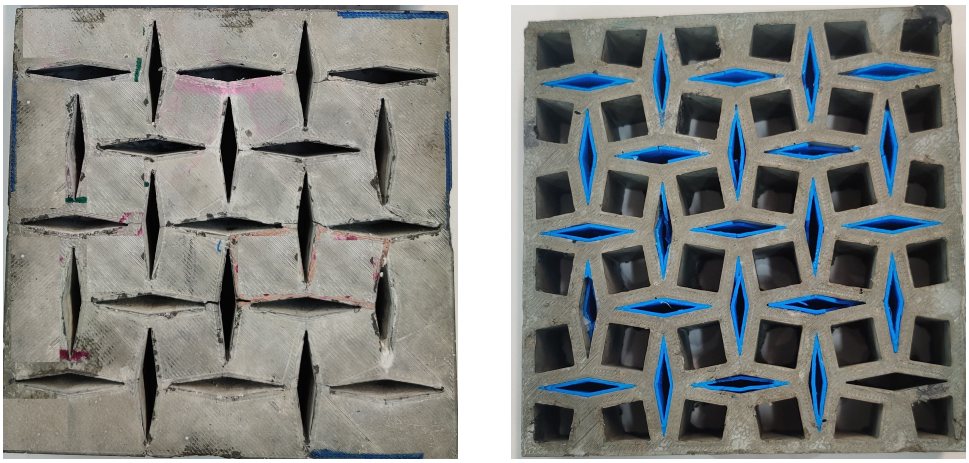
When subjected to impact load, the ordinary material deforms in the direction perpen-

dicular to the applied load. In contrast, the auxetic material, when subjected to an impact load, flows in the vicinity of the impact point and creates area of denser material, resulting in an increase in indentation resistance [48]. Based on the theory of elasticity, the indentation resistance of isotropic material is closely related to material hardness, which is directly proportional to E/(1-ν^2) at uniform pressure distribution. Hence, as the Poisson's ratio approaches to -1, the indentation resistance tends to infinity [13, 85].

The auxetic materials can exhibit a greater indentation resistance as compared to honeycomb cells under the specific conditions [86]. Due to negative PR, the auxetic materials demonstrate improved fracture toughness and crack resistance such that material expands, and crack closes up when being pulled apart. More energy is required to propagate the crack in the auxetic laminate [87] as compared to conventional material increasing its crack resistance up to twice that of non-auxetic material [88]. For conventional material with positive PR, the surfaces of the bent prismatic beam possesses a saddle shape deformation, i.e., anticlastic curvature. In contrast, material with a negative PR assumes an ellipsoidal shape or synclastic curvature [89].

5.1.2 Mechanical response of auxetic composites based on developed inks

In this research, two geometries were tested for auxetic behavior. The geometrical design of the auxetic concrete was based on a literature review and specifically the kirigami approach. The auxetic concrete molds were 3D printed and were casted using fiber-reinforced composite produced using the same mix design as reported for the experiment with fiber-reinforced cubes and beams. The Fig 5.5 demonstrates two auxetic geometries tested in this research. The initial geometrical design (Fig 5.5a) is based on kirigami that is further modified by



(a) (b)

Figure 5.5: The auxetic geometries tested in this research (a) initial geometrical design tested, (b) optimized geometrical configuration of auxetic concrete

introducing hollow square between the diamond shape cuts (Fig 5.5b). This approach can not only reduce the material cost but should also provide the flexibility to deform and, finally, exhibit the auxetic behaviour.

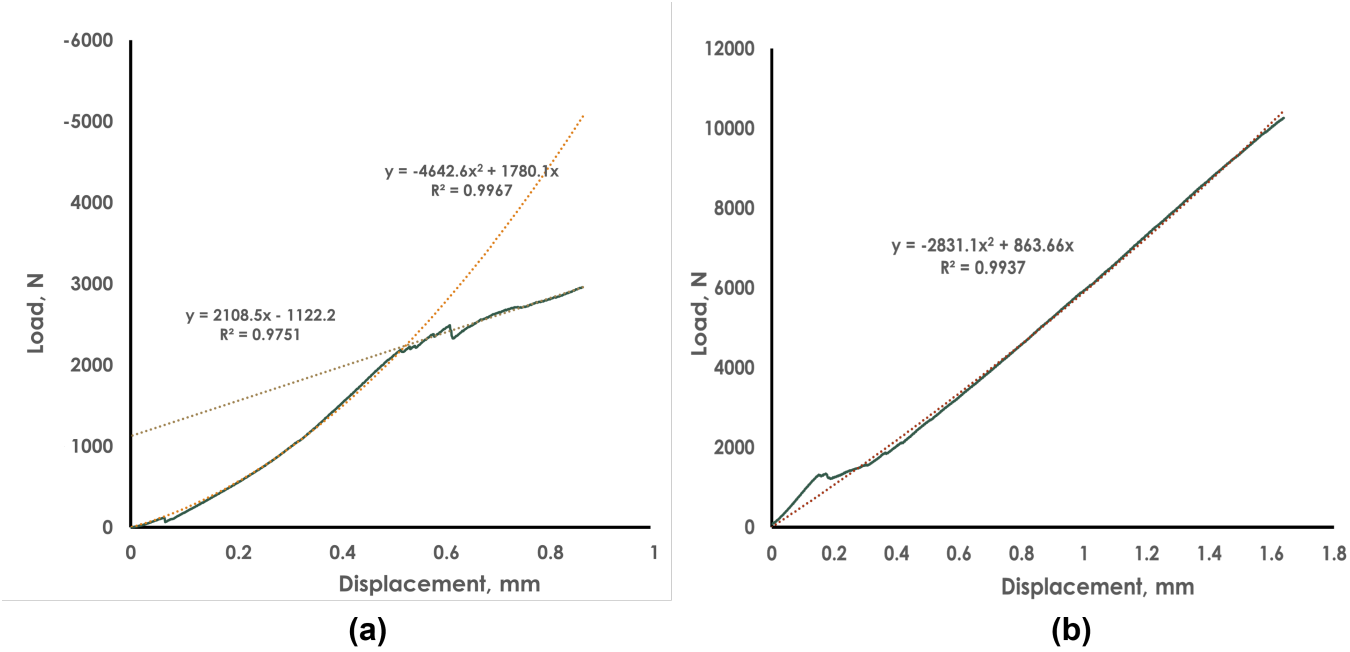


Figure 5.6: The load- displacement curve for auxetic concrete (a) initial geometry, (b) optimized geometry

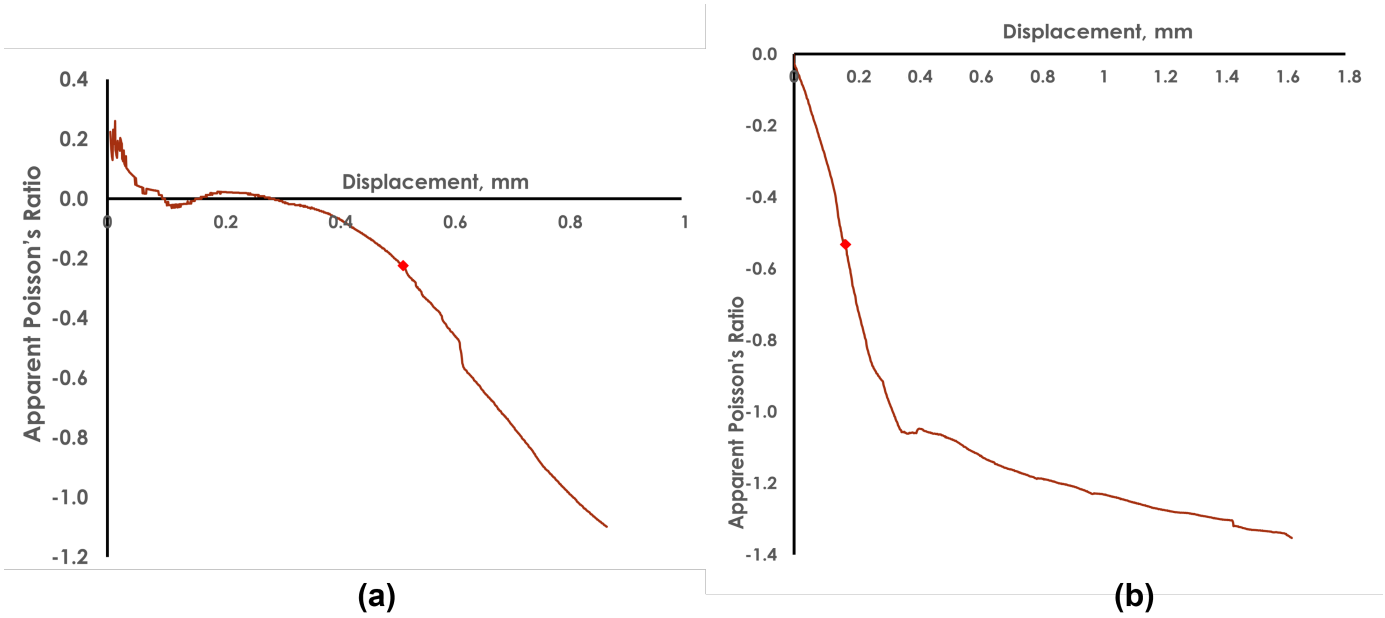


Figure 5.7: The apparent Poisson's ratio for auxetic concrete (a) initial geometry, (b) optimized geometry

Chapter 6

Conclusions and future work

The main objective of this research was to develop a range of smart material for construction applications using additive and digital manufacturing technologies. The smart materials as specified earlier in this research, based on the state-changer and shape-changer response were indeed developed. The developed MRCI inks can be used to 3D print the auxetic concrete elements which were designed and tested in this research. The experimental investigation for characterization of MRCI inks, and design and testing of auxetic concrete led to the following conclusions:

1. The addition of fly ash to superplasticized portland cement ink intended for 3D printing applications increases the plastic viscosity and reduces yield stress to zero, making the system to follow the Newtonian fluid response. This property makes the system workable and suitable for pumping operations; however, near-zero yield property was found to be not desirable for 3D printing;

2. The use of nano-particles in reference systems based on portland cement and portland cement-fly ash inks produces an effect of a significant increase in yield stress and also result in a stiffening phenomenon at near-zero shearing rates as described by the Sticky Particle Model. Therefore, the addition of nano-silica or nano-alumina to the ink systems can be a very effective performance-enhancing solution for the development of a next generation of inks for 3DPC. While nano-silica-based inks demonstrated very

promising results, the inks with nano-alumina fibers may need further tuning due to excessive fluidization realized under the test conditions;

3. Magnetite powder, when added to reference compositions at a very small dosage of 1% or less results in an increase in yield stress. The ink systems with combination of magnetite powder and nano-materials have demonstrated a significant increase in yield and stiffening. A portland cement system with magnetite powder and nano-silica has demonstrated the highest yield stress of 478.8 Pa (Table 4.1);

4. The application of magnetic field has resulted in an overall increase in yield stress for all the investigated systems, especially for systems with fly ash and magnetite powder. These compositions have demonstrated the highest percentage increase (of approximately 300%) for yield stress due to the presence of ferromagnetic inclusions in fly ash and magnetite powder;

5. The research results demonstrate that even a relatively small magnetic field of 0.1 T is capable of altering the rheological response of MRCI compositions based on a combination of portland cement, fly ash, nano-particles, and magnetite powder;

6. The Sticky Particles Model, based on the "inverted" Papanastasiou equation describes the ideal ink material suitable for the design of smart MRCI intended for 3D and 4D printing applications, which incorporates the stiffening parameter

$$\tau$$

$_s$; This parameter describes the stiffening stress, which is an important factor when describing nano-engineered cementitious inks. The system with magnetic fly ash (R_1OM)

demonstrates the highest stiffening stress amongst all the systems tested in this research;

7. The portland cement systems (including systems with fly ash) with nano-particles have demonstrated considerable increase in yield and stiffening, but on application of magnetic field, further stiffening enhancement was not observed. This is because nano-particles create a barrier between the magnetic poles, facilitating sliding instead of locking and chain formation. Here, stiffening enhancement can be realized by the addition of dopants based on ferrous oxide or other types of magnetic nano-particles;

8. The nano-particles, especially nano-silica help to accelerate the process of hydration, especially, after short time exposure to the magnetic field;

9. Due to ultrafine ferromagnetic materials used in this research such as, magnetite powder and also cobalt powder accelerate the process of portland cement hydration, which is accelerated further after exposure to the magnetic field;

10. The fly ash beneficiation process has proved to be effective in extracting high ferrous content products for MRCI. The MRCI compositions with these fly ash beneficiated products without any nano-particles have demonstrated comparatively higher stress values on the application of the magnetic field. Furthermore, it can be concluded that fly ash beneficiated products are sustainable and cost-effective than other ferrous-rich powders (magnetite and cobalt powder) used in this research;

11. This research is successful in demonstrating the auxetic behavior in concrete structures design based on kirigami approach. The geometrical design of auxetic concrete is optimized to get better auxetic behaviour and apparent Poisson's ratio. However, further research will be needed to design other geometrical shapes for auxetic concrete

demonstrating negative apparent Poisson's ratio;

12. Auxetic response with apparent zero to negative Poisson's ratio was demonstrated for fiber reinforced composites based on the developed inks with nano-particles.

The on-demand manipulation of the MRCI structure's rheological response in the fresh state, which impacts the hydration and microstructure formation and results in tunable properties and mechanical response in the hardened state, can be considered the fourth dimension of material design, which may be considered the next stage of additive manufacturing technology, leading to 4D printing. Furthermore, the response of 3D printed auxetic concrete structures to various loading conditions will give 4^{th} dimension to the concrete auxetic structures. The two smart materials- MRCI and auxetic concrete studied in the research have the potential to develop next-generation sustainable smart infrastructure that would be the future of the construction industry.

Bibliography

[1] Md Hossain, Altynay Zhumabekova, Suvash Chandra Paul, Jong Ryeol Kim, et al. A review of 3d printing in construction and its impact on the labor market. *Sustainability*, 12(20):8492, 2020.

[2] Scott Muzenski, Ismael Flores-Vivian, and Konstantin Sobolev. Ultra-high strength cement-based composites designed with aluminum oxide nano-fibers. *Construction and Building Materials*, 220:177–186, September 2019.

[3] Sriramya Duddukuri Nair and Raissa Douglas Ferron. Set-on-demand concrete. *Cement and Concrete Research*, 57:13–27, March 2014.

[4] Yun-Che Wang and RS Lakes. Composites with inclusions of negative bulk modulus: extreme damping and negative poisson's ratio. *Journal of composite materials*, 39(18):1645–1657, 2005.

[5] GuoWei Ma, Li Wang, and Yang Ju. State-of-the-art of 3D printing technology of cementitious material—An emerging technique for construction. *Science China Technological Sciences*, 61(4):475–495, April 2018.

[6] Freek Bos, Rob Wolfs, Zeeshan Ahmed, and Theo Salet. Additive manufacturing of concrete in construction: potentials and challenges of 3d concrete printing. *Virtual and Physical Prototyping*, 11(3):209–225, 2016.

[7] Robert Bogue. Smart materials: a review of capabilities and applications. *Assembly Automation*, 34(1):16–22, January 2014.

[8] KE Evans and MA Nkansah. 1. j. hutchinson, and sc rogers. *Nature*, 353:124, 1991.

[9] JB Choi and RS Lakes. Non-linear properties of metallic cellular materials with a negative poisson's ratio. *Journal of Materials Science*, 27(19):5375–5381, 1992.

[10] Ivan I Argatov, Raúl Guinovart-Díaz, and Federico J Sabina. On local indentation and impact compliance of isotropic auxetic materials from the continuum mechanics viewpoint. *International Journal of Engineering Science*, 54:42–57, 2012.

[11] VL Coenen and KL Alderson. Mechanisms of failure in the static indentation resistance of auxetic carbon fibre laminates. *physica status solidi (b)*, 248(1):66–72, 2011.

[12] JB Choi and RS Lakes. Fracture toughness of re-entrant foam materials with a negative poisson's ratio: experiment and analysis. *International Journal of fracture*, 80(1):73–83, 1996.

[13] Xin Ren, Raj Das, Phuong Tran, Tuan Duc Ngo, and Yi Min Xie. Auxetic metamaterials and structures: a review. *Smart materials and structures*, 27(2):023001, 2018.

[14] Andrew Alderson, J Rasburn, and KE Evans. Mass transport properties of auxetic (negative poisson's ratio) foams. *physica status solidi (b)*, 244(3):817–827, 2007.

[15] Mohammad Sanami, Naveen Ravirala, Kim Alderson, and Andrew Alderson. Auxetic materials for sports applications. *Procedia Engineering*, 72(Supplement C):453–458, 2014.

[16] Roderic Lakes. Foam structures with a negative poisson's ratio. *Science*, 235:1038–1041, 1987.

[17] Matteo Bianchi and Fabrizio Scarpa. Vibration transmissibility and damping behaviour

for auxetic and conventional foams under linear and nonlinear regimes. *Smart materials and structures*, 22(8):084010, 2013.

[18] Freek P. Bos, Zeeshan Y. Ahmed, Rob J. M. Wolfs, and Theo A. M. Salet. 3D Printing Concrete with Reinforcement. In D.A. Hordijk and M. Luković, editors, *High Tech Concrete: Where Technology and Engineering Meet*, pages 2484–2493. Springer International Publishing, Cham, 2018.

[19] Izabela Hager, Anna Golonka, and Roman Putanowicz. 3D Printing of Buildings and Building Components as the Future of Sustainable Construction? *Procedia Engineering*, 151:292–299, 2016.

[20] Yi Wei Daniel Tay, Biranchi Panda, Suvash Chandra Paul, Nisar Ahamed Noor Mohamed, Ming Jen Tan, and Kah Fai Leong. 3D printing trends in building and construction industry: a review. *Virtual and Physical Prototyping*, 12(3):261–276, July 2017.

[21] I.O. Omuh P.F. Tunji-Olayeni A.O. Afolabi, R.A. Ojelabi. 3d house printing: A sustainable housing solution for nigeria's housing needs. *Conference Series: Physics*, 1299, 2019.

[22] Steven J Schuldt, Jeneé A Jagoda, Andrew J Hoisington, and Justin D Delorit. A systematic review and analysis of the viability of 3d-printed construction in remote environments. *Automation in Construction*, 125:103642, 2021.

[23] Vladimir Lojanica, Vesna-Mila Colic-Damjanovic, and Novica Jankovic. Housing of the future: Housing design of the fourth industrial revolution. In *2018 5th International Symposium on Environment-Friendly Energies and Applications (EFEA)*, pages 1–4. IEEE, 2018.

[24] AL Mohd Tobi, SA Omar, Z Yehia, S Al-Ojaili, A Hashim, and O Orhan. Cost viability of 3d printed house in uk. In *IOP Conference Series: Materials Science and Engineering*, volume 319, page 012061. IOP Publishing, 2018.

[25] Tracie Prater, Monsi Roman, Tony Kim, and Rob Mueller. Nasa centennial challenge: 3d-printed habitat. In *AIAA Space 2017*, 2017.

[26] Daniel Delgado Camacho, Patricia Clayton, William O'Brien, Raissa Ferron, Maria Juenger, Salvatore Salamone, and Carolyn Seepersad. Applications of additive manufacturing in the construction industry–a prospective review. In *ISARC. Proceedings of the International Symposium on Automation and Robotics in Construction*, volume 34. IAARC Publications, 2017.

[27] Eric L Kreiger, Megan A Kreiger, and Michael P Case. Development of the construction processes for reinforced additively constructed concrete. *Additive Manufacturing*, 28:39–49, 2019.

[28] David Smith. Printed buildings: an international race for the ultimate in automation. *Construction Research and Innovation*, 3(2):26–31, 2012.

[29] Jüri Liiv, Tonis Teppand, Ergo Rikmann, and Toomas Tenno. Novel ecosustainable peat and oil shale ash-based 3d-printable composite material. *Sustainable Materials and Technologies*, 17:e00067, 2018.

[30] Geert De Schutter, Karel Lesage, Viktor Mechtcherine, Venkatesh Naidu Nerella, Guillaume Habert, and Isolda Agusti-Juan. Vision of 3d printing with concrete—technical, economic and environmental potentials. *Cement and Concrete Research*, 112:25–36, 2018.

[31] Skylar Tibbits. 4D Printing: Multi-Material Shape Change. *Architectural Design*, 84(1):116–121, January 2014.

[32] Skylar Tibbits. The emergence of "4D printing".

[33] Farhang Momeni, Seyed M.Mehdi Hassani.N, Xun Liu, and Jun Ni. A review of 4D printing. *Materials & Design*, 122:42–79, May 2017.

[34] Xiao Kuang, Devin J. Roach, Jiangtao Wu, Craig M. Hamel, Zhen Ding, Tiejun Wang, Martin L. Dunn, and Hang Jerry Qi. Advances in 4D Printing: Materials and Applications. *Advanced Functional Materials*, 29(2):1805290, January 2019.

[35] Comlan Sossou. A holistic approach to design for 4D Printing. page 202.

[36] Business wire. 4d printing market-forecasts from 2017 to 2022. *Research and Markets*, 4331728(2):75, 2019.

[37] Olafur Haraldsson Wallevik and Jon Elvar Wallevik. Rheology as a tool in concrete science: The use of rheographs and workability boxes. *Cement and Concrete Research*, 41(12):1279–1288, December 2011.

[38] Mohamadreza Moini, Jan Olek, Bryan Magee, Pablo Zavattieri, and Jeffrey Youngblood. Additive Manufacturing and Characterization of Architectured Cement-Based Materials via X-ray Micro-computed Tomography. In Timothy Wangler and Robert J. Flatt, editors, *First RILEM International Conference on Concrete and Digital Fabrication – Digital Concrete 2018*, volume 19, pages 176–189. Springer International Publishing, Cham, 2019. Series Title: RILEM Bookseries.

[39] M. Kosson, L. Brown, and F. Sanchez. Early-Age Performance of 3D Printed Carbon

Nanofiber and Carbon Microfiber Cement Composites. *Transportation Research Record: Journal of the Transportation Research Board*, 2674(2), February 2020.

[40] Ioan Bica, Ying Dan Liu, and Hyoung Jin Choi. Physical characteristics of magnetorheological suspensions and their applications. *Journal of Industrial and Engineering Chemistry*, 19(2):394–406, March 2013.

[41] M. Ashtiani, S.H. Hashemabadi, and A. Ghaffari. A review on the magnetorheological fluid preparation and stabilization. *Journal of Magnetism and Magnetic Materials*, 374:716–730, January 2015.

[42] Sriramya Duddukuri Nair and Raissa Douglas Ferron. Real time control of fresh cement paste stiffening: Smart cement-based materials via a magnetorheological approach. *Rheologica Acta*, 55(7):571–579, July 2016.

[43] Weng W. Chooi and S. Olutunde Oyadiji. Design, modelling and testing of magnetorheological (MR) dampers using analytical flow solutions. *Computers & Structures*, 86(3-5):473–482, February 2008.

[44] C. Guerrero-Sanchez, T. Lara-Ceniceros, E. Jimenez-Regalado, M. Raşa, and U. S. Schubert. Magnetorheological Fluids Based on Ionic Liquids. *Advanced Materials*, 19(13):1740–1747, July 2007.

[45] Konstantin Sobolev. Mechano-chemical modification of cement with high volumes of blast furnace slag. *Cement and concrete composites*, 27(7-8):848–853, 2005.

[46] Laurent Sibille, Paul Carpenter, Ronald Schlagheck, and Raymond A French. Lunar regolith simulant materials: recommendations for standardization, production, and usage. *Marshall Space Flight Center*, 2005.

[47] A Sgambatia, M Berga, F Rossia, A Daurskikhb, B Imhofc, R Davenportc, P Weiss, M Peer, T Gobert, and A Makaya. Urban: conceiving a lunar base using 3d printing technologies. In *Proceedings of the 69th International Astronautical Congress, Bremen, Germany*, pages 1–5, 2018.

[48] Lei Jiang, Dustin Pearson, and Tim Dunbar. Modeling of impact properties of auxetic materials phase 2. Technical report, Martec Limited Halifax, Nova Scotia Canada, 2014.

[49] Seyed Mohammad Sajadi, Cristiano F. Woellner, Prathyush Ramesh, Shannon L. Eichmann, Qiushi Sun, Peter J. Boul, Carl J. Thaemlitz, Muhammad M. Rahman, Ray H. Baughman, Douglas S. Galvão, Chandra Sekhar Tiwary, and Pulickel M. Ajayan. 3D Printed Tubulanes as Lightweight Hypervelocity Impact Resistant Structures. *Small*, 15(52):1904747, December 2019.

[50] Konstantin Sobolev and Miguel Ferrada Gutiérrez. How Nanotechnology Can Change the Concrete World. In *Progress in Nanotechnology*, pages 113–116. John Wiley & Sons, Inc., Hoboken, NJ, USA, August 2014.

[51] Qinghua Li, Xiang Gao, and Shilang Xu. Multiple effects of nano-SiO2 and hybrid fibers on properties of high toughness fiber reinforced cementitious composites with high-volume fly ash. *Cement and Concrete Composites*, 72:201–212, September 2016.

[52] Scott Muzenski, Ismael Flores-Vivian, and Konstantin Sobolev. Ultra-high strength cement-based composites designed with aluminum oxide nano-fibers. *Construction and Building Materials*, 220:177–186, 2019.

[53] Ismael Flores-Vivian, Rani G K Pradoto, Mohamadreza Moini, and Konstantin Sobolev. THE USE OF NANOPARTICLES TO IMPROVE THE PERFORMANCE OF CONCRETE. page 7, 2013.

[54] M. Collepardi, S. Collepardi, U. Skarp, and R. Troli. Optimization of Silica Fume, Fly Ash, and Amorphous Nano-Silica in Superplasticized High-Performance Concretes. In *Proceedings of 8th CANMET, SP-221*, Las Vegas, USA, 2004.

[55] Pedro Serna, Francesco Lo Monte, Eduardo J Mezquida-Alcaraz, Viktor Mechtcherine, Michaela Reichardt, Alva Peled, Oren Regev, Ruben P Borg, Alexej Tretjakov, Dennis Lizunov, Konstantin Sobolev, Stamatina Sideri, Kim Nelson, and Enrico Maria Gastaldo Brac. UPGRADING THE CONCEPT OF UHPFRC FOR HIGH DURABILITY IN THE CRACKED STATE: THE CONCEPT OF ULTRA HIGH DURABILITY CONCRETE (UHDC) IN THE APPROACH OF THE H2020 PROJECT RESHEALIENCE. page 8.

[56] Gyu Don Moon, Sungwoo Oh, and Young Cheol Choi. Effects of the physicochemical properties of fly ash on the compressive strength of high-volume fly ash mortar. *Construction and Building Materials*, 124:1072–1080, 2016.

[57] L Krishnaraj and PT Ravichandran. Investigation on grinding impact of fly ash particles and its characterization analysis in cement mortar composites. *Ain Shams Engineering Journal*, 10(2):267–274, 2019.

[58] Dengwu Jiao, Karel Lesage, Mert Yucel Yardimci, Khadija El Cheikh, Caijun Shi, and Geert De Schutter. Quantitative assessment of the influence of external magnetic field on clustering of nano-Fe3O4 particles in cementitious paste. *Cement and Concrete Research*, 142:106345, April 2021.

[59] J David Carlson and Mark R Jolly. MR fluid, foam and elastomer devices. page 15, 2000.

[60] Ying Dan Liu, Cheng Hai Hong, and Hyoung Jin Choi. Polymeric colloidal magnetic composite microspheres and their magneto-responsive characteristics. *Macromolecular Research*, 20(12):1211–1218, December 2012.

[61] W H Li, G Chen, and S H Yeo. Viscoelastic properties of MR fluids. *Smart Materials and Structures*, 8(4):460–468, August 1999.

[62] E. C. Bingham. An investigation of the laws of plastic flow. *Bulletin of the Bureau of Standards*, 13(2):309, August 1916.

[63] A G Olabi and A Grunwald. Design and Application of Magneto-Rheological Fluid "MRF". page 19.

[64] C Acary-Robert, E D Fernández-Nieto, G Narbona-Reina, and P Vigneaux. Viscoplastic Free-Surface Flows: The Herschel-Bulkley Case. page 15.

[65] Juan de Vicente, Daniel J. Klingenberg, and Roque Hidalgo-Alvarez. Magnetorheological fluids: a review. *Soft Matter*, 7(8):3701, 2011.

[66] Jong Hyeok Park, Moo Hyun Kwon, and O. Ok Park. Rheological properties and stability of magnetorheological fluids using viscoelastic medium and nanoadditives. *Korean Journal of Chemical Engineering*, 18(5):580–585, September 2001.

[67] Geert De Schutter and Karel Lesage. Active control of properties of concrete: a (p)review. *Materials and Structures*, 51(5):123, October 2018.

[68] Chiara F Ferraris, Nicos S Martys, Max Peltz, William L George, Edward J Garboczi, and Blaza Toman. Certification of SRM 2497:: standard reference concrete for rheological measurements. Technical Report NIST SP 260-194, National Institute of Standards and Technology, Gaithersburg, MD, April 2019.

[69] ASTM International. Standard practice for mechanical mixing of hydraulic cement pastes and mortars of plastic consistency. *ASTM lnternational*, pages 1–3, 2006.

[70] Dengwu Jiao, Khadija El Cheikh, Caijun Shi, Karel Lesage, and Geert De Schutter. Structural build-up of cementitious paste with nano-Fe3O4 under time-varying magnetic fields. *Cement and Concrete Research*, 124:105857, October 2019.

[71] P F G Banfill, editor. *Rheology of Fresh Cement and Concrete*. Taylor & Francis, Abingdon, UK, 1991.

[72] Huaning Zhu, Nicos S. Martys, Chiara Ferraris, and Daniel De Kee. A numerical study of the flow of Bingham-like fluids in two-dimensional vane and cylinder rheometers using a smoothed particle hydrodynamics (SPH) based method. *Journal of Non-Newtonian Fluid Mechanics*, 165(7-8):362–375, April 2010.

[73] Aparna S Deshmukh, Reed T Heintzkill, Rosalba A Huerta, and Konstantin Sobolev. Rheological response of magnetorheological cementitious inks tuned for active control in digital construction. *Materials Journal*, 118(6):263–274, 2021.

[74] George Jefferson, Ronald J Kerans, and Triplicane A Parthasarathy. Bi-material composite structure with reduced thermal expansion, March 27 2012. US Patent 8,142,874.

[75] Tomohiro Tachi, Evgueni T Filipov, and Glaucio H Paulino. Deployable folded-core sandwich panels guided by a generating surface. In *Proceedings of IASS Annual Symposia*, volume 2015, pages 1–7. International Association for Shell and Spatial Structures (IASS), 2015.

[76] Siméon Denis Poisson. Note sur les vibrations des corps sonores. *Ann. Chim. Phys*, 36:86–93, 1827.

[77] Luke Mizzi, EM Mahdi, Kirill Titov, Ruben Gatt, Daphne Attard, Kenneth E Evans, Joseph N Grima, and Jin-Chong Tan. Mechanical metamaterials with star-shaped pores exhibiting negative and zero poisson's ratio. *Materials & Design*, 146:28–37, 2018.

[78] IJ Gibson and Michael Farries Ashby. The mechanics of three-dimensional cellular materials. *Proceedings of the Royal Society of London. A. Mathematical and Physical Sciences*, 382(1782):43–59, 1982.

[79] Brendan Burns Healy, Aparna Deshmukh, Elliott Fairchild, Caroline J Merighi, and Konstantin Sobolev. Wallpaper groups and auxetic metamaterials. *arXiv preprint arXiv:2102.12972*, 2021.

[80] Edwin A Peraza Hernandez, Darren J Hartl, and Dimitris C Lagoudas. Introduction to active origami structures. In *Active Origami*, pages 1–53. Springer, 2019.

[81] Terry C Shyu, Pablo F Damasceno, Paul M Dodd, Aaron Lamoureux, Lizhi Xu, Matthew Shlian, Max Shtein, Sharon C Glotzer, and Nicholas A Kotov. A kirigami approach to engineering elasticity in nanocomposites through patterned defects. *Nature materials*, 14(8):785–789, 2015.

[82] Robin M Neville, Fabrizio Scarpa, and Alberto Pirrera. Shape morphing kirigami mechanical metamaterials. *Scientific reports*, 6:31067, 2016.

[83] Joseph N Grima and Ruben Gatt. Perforated sheets exhibiting negative poisson's ratios. *Advanced Engineering Materials*, 12(6):460–464, 2010.

[84] Sicong Shan, Sung H Kang, Zhenhao Zhao, Lichen Fang, and Katia Bertoldi. Design of planar isotropic negative poisson's ratio structures. *Extreme Mechanics Letters*, 4:96–102, 2015.

[85] Kenneth E Evans and Andrew Alderson. Auxetic materials: functional materials and structures from lateral thinking! *Advanced materials*, 12(9):617–628, 2000.

[86] Justin Dirrenberger, Samuel Forest, and Dominique Jeulin. Effective elastic properties of auxetic microstructures: anisotropy and structural applications. *International Journal of Mechanics and Materials in Design*, 9(1):21–33, 2013.

[87] Teik-Cheng Lim and U Rajendra Acharya. Longitudinal modulus of semi-auxetic unidirectional fiber composites. *Journal of reinforced plastics and composites*, 29(10):1441–1445, 2010.

[88] Andrews Boakye, Yuping Chang, King Raji Rafiu, and Pibo Ma. Design and manufacture of knitted tubular fabric with auxetic effect. *The Journal of The Textile Institute*, 109(5):596–602, 2018.

[89] Kadir Bilisik, Nesrin Sahbaz Karaduman, and Nedim Erman Bilisik. Fiber architectures for composite applications. In *Fibrous and textile materials for composite applications*, pages 75–134. Springer, 2016.

Curriculum Vitae

APARNA DESHMUKH

❖ Personal Statement

More than 2 years of experience as a structural engineer and 4 years of experience in concrete and cement-based materials for the application of 3D printing of concrete, focused in the rheological and magnetorheological characterization of cement composites. Seeking for challenging position that demands structural as well as materials background focused on testing, designing, and developing a new generation of cement composites for construction.

❖ Education

University of Wisconsin- Milwaukee, WI
PhD in Civil-Materials-Structural Engineering, 2017-2021 December
JSPM's Rajarshi Shahu College of Engineering - Pune, India
ME in Structural Engineering, 2015
Government College of Engineering Karad, India
BS in Civil Engineering, 2012

❖ Honors/Awards

- ***UWM Graduate Student Chancellor Award***, six semesters, 2018-2021
  - 'Best and the brightest' student with GPA of 3.5 or above
- Second place in ***Three Minute Thesis (3MT) competition 2020***.
- Title: Nano-engineered composites for 3D printing of concrete auxetic structures.
  https://www.youtube.com/watch?v=XaMhFH8p6Oc
- TU Dresden and DAAD scholarship to attend ***Dresden International summer school 2019 in TU Dresden***, Germany on "Mineral-bonded composites for enhanced structural impact safety."
- First place in ***ME Structural Engineering in RSCOE,*** 2015

❖ Research Experience

University of Wisconsin- Milwaukee, **Research Assistant,** **Fall 2017-Present**
Civil and Environmental Engineering Department
(PhD Thesis on *'Characterisation of magnetorheological cement compositions for 3D printing of concrete(3DPC) application' (Fall 2018-Present))*

- Performed tests such as particle size distribution, XRD, SEM for material characterisation for 3DPC.
- Performed rheological tests on various cement compositions using Dynamic Shear rheometer.
- Developed protocol for magnetorheological tests for certain cement paste compositions.
- Performed fly ash milling as a part of fly ash beneficiation project and use of iron rich fly ash in cementitious ink used for 3DPC.
- Characterisation of Lunar Regolith for 3DPC application.
- Investigated compatibility of Lunar Regolith in concrete to replace cement and aggregates.
- Design and analysis of auxetic geometries using finite element analysis.
- Developed protocol for compression and tensile testing of auxetic concrete.
- Trained undergraduate students.

Additional Research Projects

'*Smart Concrete' (Spring 2020-Present)*

- Developed cement mortar using graphene for producing electrically conductive material.
- performed tests to study dispersion of graphene.

'*Underwater concreting' (Fall 2017-Spring 2018)*

- Literature review and customer discovery for underwater concreting.

Master Thesis on *'Assessment of Capacity Enhancement of Retrofitted Bridge' (Fall 2014-2015))*

- Design and analysis of bridge deck using Finite element analysis software (ANSYS).
- Comparative study of different materials used for retrofitting of bridges.

❖ Industrial Experience

Jendusa Design and Engineers, Hartland, WI, **Structural Intern** **Fall 2018**

- Inspection and strength estimation of old residential and commercial structures.
- Retrofitting design for existing failed structures.
- Design calculations and prepared drawings for structural elements.

S W Mone & Associates- Pune, India, **Structural Design Engineer** **Jan 2016 to June 2017**

- Designed and detailing of structures
- Made and checked complex engineering computations quickly and accurately.
- Reviewed calculations and analytical data to maintain accuracy of the technical reports.
- Planned and coordinated work requiring modification of standard engineering techniques, procedures, and criteria.
- Visited project sites during construction to monitor progress and consult with contractors and on-site engineers.

Suhas Joshi Structural Designing Consultancy- Pune, India
Structural Design Engineer **Jan 2013 to June 2013**

- Visited project sites during construction to monitor progress and consult with contractors and on-site engineers.
- Structural Design of residential buildings.

❖ Teaching Experience

University of Wisconsin- Milwaukee, **Teaching Assistant** **Fall 2020-Present**
Civil and Environmental Engineering Department

- Delivering in person and online lab sessions for Engineering statistics.
- Teaching statistics software such as Excel, Minitab, and MATLAB.
- Assessing homework, lab assignments, quizzes, and exams.
- Proctoring interim and final exams.

University of Wisconsin- Milwaukee, **Instructor** **Spring 2019-Fall 2019**
Civil and Environmental Engineering Department

- Planned, prepared, and delivered lessons for Engineering Statistics course.
- Co-ordinated with teaching assistants for better co-ordination of lecture and lab sessions.
- Updated curriculum, homework, assignments, and lab manual.
- Assigned and mentored group project.
- Conducted interim and final exams.
- Prepared progress reports for each student and provided feedback to individual students.
- Prepared assessment report and other documentation required for ABET.
- Advised and co-operated with other teachers in the preparation and development of courses of study, teaching materials, and assessments.

Private Tutor, India **July 2015-April 2016**

- Provided tutoring services for structural engineering subjects like strength of Material, Theory of Structures, Design of Concrete Structures and Design of Steel Structures.

Rajarshi Shahu College of Engineering (Polytechnic), **Instructor** **December 2013-July 2015**

- Served as first faculty of newly established Civil engineering department.
- Planned, prepared, and delivered lessons for civil engineering courses such as Engineering mechanics, Strength of Material, Theory of Structures, Design of Steel Structures.
- Designed and prepared curriculum for lab sessions, teaching material and assessments.
- Conducted lab sessions for Engineering Mechanics and Strength of Material.
- Set up new laboratories, preparing academic calendar and class schedules.
- Assigned and mentored group project and organising industrial visits.
- Prepared progress reports for each student and provided feedback to individual students.
- Prepared assessment report and other documentation required for NBA accreditation.
- Advised and co-operated with other teachers in the preparation of courses of study, teaching materials, and assessments.

❖ Publications

- Aparna S. Deshmukh, Reed T. Heintzkill, Rosalba A. Huerta, Konstantin Sobolev (2021), “Rheological response of Magnetorheological cementitious ink (MRCI) tuned for active control in digital construction”, ACI materials Journal. DOI:10.14359/51733128
- Brendan Burns Healy, Aparna Deshmukh, Elliott Fairchild, Caroline J. Merighi, Konstantin Sobolev, “Wallpaper Groups and Auxetic Metamaterials”, Preprint on ResearchGate. https://www.researchgate.net/publication/349620710_Wallpaper_Groups_and_Auxetic_Metamaterials
- Deshmukh. A. S (M.E Student), Prof. G. R. Patil (Asst. Professor) (2015), “Assessment of Capacity Enhancement of Retrofitted Bridge Deck”, *Conference for M.E. Students (CIVIL PGCON)*.

❖ Professional Organization and Membership

- American Concrete Institute (ACI)
- Precast/ Prestressed Concrete Institute (PCI)
- American society for Testing Materials (ASTM)
- Society of Women Engineers (SWE)
- Student association of India at UWM, Founder, President (2018-2019) and Advisor (2019-2020)
- Member of Society of Women Engineers at UWM
- Counselor at UWM EnQuest Summer Camp 2019, which is for high school girls to introduce various fields of engineering.